UNIVERSITÉ DU LUXEMBOURG

PhD-FSTM-2024-005
The Faculty of Science, Technology and Medicine

DISSERTATION

Defence held on 10/01/2024 in Luxembourg

to obtain the degree of

DOCTEUR DE L'UNIVERSITÉ DU LUXEMBOURG

EN SCIENCES DE L'INGÉNIEUR

by

Tobias JÄGER
Born on 25 April 1993 in Munich (Germany)

MICRO SURFACE FUNCTIONALIZATION TO IMPROVE MEMBRANE DISTILLATION

Dissertation defence committee

Dr Stephan LEYER, dissertation supervisor
Professor, Université du Luxembourg

Dr Nikolaos PRASIANAKIS, second dissertation supervisor
Head of Transport Mechanisms Group, Paul Scherrer Institut

Dr Frank SCHOLZEN, Chairman
Professor, Université du Luxembourg

Dr Sergiy ANTONYUK
Professor, TU Kaiserslautern

Dr Stephan WESTERMAN, Vice Chairman
Head of Unit Functional Polymers, Luxembourg Institute of Science and Technology

ABSTRACT

As water scarcity becomes an increasing problem around the world, water desalination is becoming more important as it can provide an alternative source of water in regions with access to seawater. Among other technologies, membrane distillation is a promising approach because it can be powered by low–grade heat and operates below the boiling point. In this thesis, I studied membranes typically used for membrane distillation in an unprecedented detail, using a multi phase and multi component Lattice Boltzmann method. We investigated the liquid entry pressure and the interface shape of pressurized liquids in contact with various rough structures. We have shown that the D3Q27 Shan–Chan like multiphase model is capable of accurately predicting liquid entry pressures for realistic membrane geometries.

In our investigation, we found that surface functionalization, either through hydrophilic–hydrophobic zoning or a pillar structure, can increase the liquid–gas interface area of a liquid film in contact with such surfaces and increases the magnitude of the evaporation flux by 5% to 6%. For an untreated membrane surface the liquid–gas interface was limited by the porosity of the membrane.

Moreover we observed an agglomeration of water droplets in membrane regions of high porosity when water vapor condenses inside the membrane structure.

We also conducted a theoretical analysis of the constant mean curvature problem in cases of rotational symmetry. This analysis allowed us to determine an analytical expression for the liquid entry pressure of a hydrophobic pillar–pore structure, as well as the shape of the liquid–gas interface and the location of its minimum.

Furthering our research, we analyzed the stability and energy barrier of droplets in the Cassie–Baxter state on periodically pillared surfaces. Based on this, we further develop a transition criterion and derive an improved version which allows predicting for which pillar geometries, equilibrium contact angles and droplet volumes the Cassie–Baxter state switches from a meta stable to an unstable state. This enabled a comparison with existing experiments and 3D multi phase Lattice Boltzmann simulations for different pillar geometries and equilibrium contact angles, where a good agreement has been found.

ACKNOWLEDGMENTS

First and foremost I am extremely grateful to my supervisor Prof. Stephan Leyer and my co–supervisor Dr. Nikolaos Prasniakis for their invaluable advice, continuous support, and patience during my PhD study. Their plentiful experience and knowledge have encouraged me in all the time of my academic research. I would also like to thank Prof. Frank Scholzen for being part of my thesis supervision committee. I appreciate his support and valuable advice.

Furthermore I am very thankful for the many fruitful discussions and support from Dr. Athanasios Mokos, Jemp Keup, Dr. Filip Janasz, Tahmineh Adili and the rest of the team. A special thanks goes to Dr. Marie–Alix Dalle for the many insightful discussions on evaporation models and the results presented in chapter 6.

The calculations in this work were carried out using the HPC facilities at the University of Luxembourg and the Swiss Supercomputing Center CSCS. I also thank the University of Luxembourg and Swiss-Nuclear for their support.

I would also like to thank my friends who have made my time at the university of Luxembourg a special and unforgettable part of my life that I will always treasure.

Finally, I would like to express my deep appreciation to my parents, my brother and my partner Anne Karst, whose understanding and support have been indispensable. I would also like to thank Anne Karst for proofreading this dissertation.

CONTENTS

ACRONYMS

MD	Membrane Distillation
CMC	Constant mean curvature
PDE	Partial differential equation
Δp_{crit}	Liquid Entry Pressure (LEP)
γ	Surface tension
q	$\Delta p / \gamma$
r_p	Pillar radius
r_c	Pore radius
α_p	Contact angles between the liquid and the pillar wall
α_c	Contact angles between the liquid and the pore wall
α_0	Equilibrium contact angle between liquid and solid
P	Pillar distance (periodicity in x– and y–direction)
A_c	Area of the periodically repeated cell ($A_c = P \times P$)
A	Top area of the pillar
l	Perimeter of the pillar
$\hat{\mathbf{n}}$	Unit normal vector of the liquid–gas interface
LB	Lattice Boltzmann
NRMSD	Normalised root mean square deviation
f_i	Discreet density distribution function
p	Pressure
ρ	Density
ρ_l	Liquid density
ρ_g	Gas density
$\mathbf{F}$	Force
Δx	Lattice spacing
Δt	Time step
m	Fluid particle mass
G_{ads}	LB parameter to tune the equilibrium contact angle
G	LB parameter to control the fluid–fluid interaction strength
τ	Relaxation time for the collision term
ν	Kinematic viscosity
c_s	Speed of sound
g	Gravitation acceleration
$\mathbf{v}$	Velocity

$\mathbf{c_i}$	Discrete lattice velocity
j	Mass flux
T	Temperature
σ	Dimensionless coefficient from the Hertz–Knudsen equation
L	Characteristic length
λ	Mean free path
Kn	Knudsen number
Bo	Bond number
Ca	Capillary number
D	Diffusivity
R_s	Specific gas constant
p_s	Saturation vapor pressure

1 INTRODUCTION

According to the United Nations, "water scarcity is a growing problem on every continent, with poorer communities most badly affected" [27]. In general one distinguishes between physical and economic water scarcity. Physical water scarcity, also known as absolute water scarcity, occurs when the demand for water in a particular region exceeds the limited water resources available there [33]. Based on a UN report released in 2007, roughly 1.2 billion individuals, accounting for nearly 20% of the people in the world, inhabit areas hit by physical water scarcity [28].

Water scarcity is also observed in regions and countries with sufficient water resources. This is for example caused by broken infrastructure, pollution, conflicts and inadequate water resource management. In the future, human actions and the climate crisis will further undermine people's access to clean water and sanitary facilities [48].

Mekonnen and Hoekstra [26] found that "two–thirds of the global population (4 billion people) live under conditions of severe water scarcity at least 1 month of the year. Half a billion people in the world face severe water scarcity all year round" (2016). It is projected that by 2025, nearly half of the people in the world could be inhabiting regions experiencing water scarcity, and acute water scarcity could disperse around 700 million humans by 2030. Additionally, by 2040, approximately one in four children worldwide will be residing in regions exposed to severe water stress [48].

The negative effects of water scarcity are far–reaching, as the lack of safe drinking water and basic hygiene practices increases the susceptibility to diseases such as cholera. In general, a limited supply of clean water also increases its cost [48].

Water desalination is essential for solving water scarcity in regions where seawater is available. Thermal distillation and reverse osmosis are the most commonly used technologies for seawater desalination. Thermal separation methods can be categorized into multi–effect distillation, low–pressure steam processes, and multi–stage flash evaporators [11]. However, these techniques demand substantial power and a reliable electricity supply [29]. In contrast, membrane distillation (MD) is a thermal separation process powered by low grade heat that functions at temperatures lower than the boiling point at ambient pressure and offers a promising solution to global water scarcity [3]. MD employs evaporation to extract clean, distilled water from salt, brackish or other contaminated water sources. In contrast to the previously mentioned technologies, MD offers the benefits of minimal capital and

operational expenses, since it may be powered by non–concentrated solar heat [9] or residual heat sources [3]. Nevertheless, the overall effectiveness and the magnitude of the distilled fresh water flux of MD modules are currently insufficient for competitive performance [2, 38].

Various MD designs have been developed, with air gap membrane distillation (AGMD) being a particularly promising approach for seawater distillation [3]. In AGMD, the heated input solution makes direct contact with a hydrophobic membrane. However, unlike direct contact membrane distillation, an air gap exists and separates the membrane from the condenser. Water vapor is transported through the porous structure of the membrane and the air gap before condensing on a cooled solid interface (see figure 1.1). The hydrophobic nature of the membrane material prohibits an intrusion of saltwater into the porous structure, ensuring that only water vapor without salt or other impurities can cross the membrane [43]. The air gap offers the advantage of thermal insulation and therefore reduces the heat loss. However, a disadvantage is the additional mass transport pathway due to the air gap, which affects the membrane throughput [3].

State–of–the–art AGMD modeling [4, 13, 17–19, 43] typically consists of modeling the heat transfer from the hot water channel to the cold water channel and the mass transfer from the hot water channel to the condensation film (see figure 1.1). This usually involves the numerical solution of partial differential equations describing the conservation of mass, momentum and energy using methods from traditional CFD. This approach typically includes the use of the dusty gas model to represent the membrane and the diffusion of water vapor through it. In the dusty gas model, membrane properties like porosity, tortuosity, and the viscosity of the gas mixture are essential input parameters for calculating the total vapor flow through the membrane. However, this model is a very coarse approximation of the membrane, the vapor transport, and the liquid–gas interface where evaporation takes place, and doesn't take into account the detailed pore geometry of the membrane. Normally, these types of models assume a flat liquid–gas interface and neglect the interaction of liquid and hydrophobic membrane material.

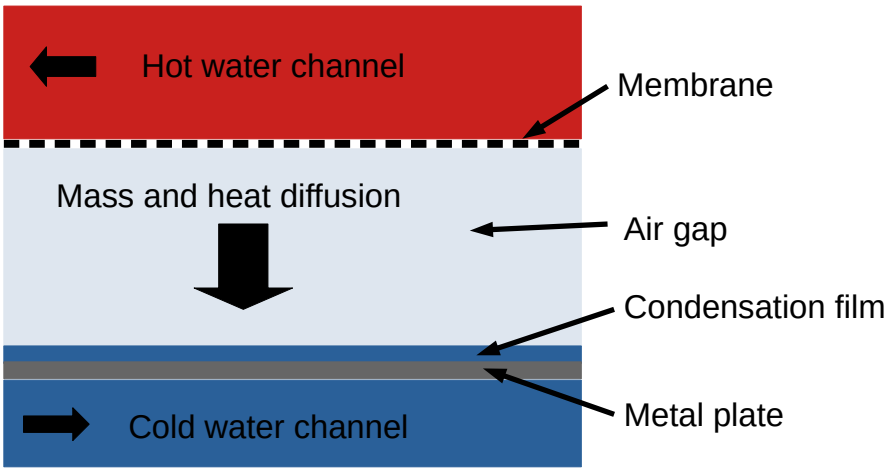

Figure 1.1: Schema of an air gap membrane distillation module [16].

The driving force for water vapor transport in AGMD is the water vapor concentration gradient in the porous membrane and the layer of air. A higher temperature at the evaporation interface results in a higher saturation vapor pressure compared to the condensation interface. Typically, the saturation vapor pressure in the air gap and the membrane is assumed when modeling a complete AGMD module. Based on the temperature, the Antoine equation can be used to calculate the saturation vapor pressure at the condensation and evaporation interface. The difference of the saturation vapor pressures can be used to calculate the total vapor flux. Full saturation in the air gap is an assumption that may not be true. Since the partial vapor pressure effects the magnitude of the evaporation flux it is important to gain a better understanding which vapor pressures can be expected and how this influences the magnitude of the fresh water flux obtained with the AGMD module.

Since the saturation level above the evaporation and condensation interface has a strong influence on the magnitude of the evaporation and condensation fluxes [31], a detailed modeling of the separation processes which resolves the vapor concentration in the membrane and the air gap is important. The key mechanisms involved are evaporation, diffusion, and condensation of water vapor. To enhance efficiency and to maximize the distilled water flux of MD modules, a deeper comprehension of the fundamental mechanisms at the pore level is crucial.

Evaporation of water leads to an increased salt concentration at the evaporation interface, which can result in salt and pollutant precipitation and membrane pore blockage. Specific membrane structures, such as micropillars, arranged in a periodic pattern, and high hydrophobicity can mitigate scaling issues and prolong the membrane's lifespan [49]. A detailed understanding of the impact of surface roughness, e.g.

achieved by micropillars, on the hydrophobicity, the liquid distribution and the liquid–gas interface is therefore desirable.

The evaporation and diffusive transport happens within the membrane's microporous layout. Because evaluating microscopic–level flow using experimental techniques is intricate, there exists an incomplete understanding concerning the interplay among gas, liquid and the hydrophobic membrane material on the pore scale. Therefore to enhance the performance of MD modules, an improved comprehension of the underlying mechanisms on the pore scale, is mandatory. As a result, in–depth numerical modeling of the phenomena within MD becomes imperative.

Evaporation, being a non–equilibrium phenomenon, is a complicated occurrence featuring a discontinuity in the temperature field at the interface between the liquid and gas phases. Various theories, like statistical rate theory and the Hertz–Knudsen equation, have been formulated for the estimation of the evaporation flux [31, 32] using a static liquid–gas interface as a foundation.

The magnitude of the evaporation flux is influenced by various factors, including the vapor pressure across the liquid–gas interface, the extent of the liquid–gas interface's surface area, and the concentration of salt in the water. A larger liquid–gas interface results in higher evaporation fluxes. Therefore, it is important to determine the shape of the liquid–gas interface as a foundation for the aforementioned evaporation models.

The main research questions addressed in this thesis to improve the membranes used for MD are:

- We validate a Shan–Chen type mulitphase LB model and its capability to simulate flow in a complex and realistic 3D porous membrane structure.
- We try to answer which liquid distribution can be expected inside the porous structure of the membrane if water condensates.
- Understanding and controlling the interface shape of pressurized liquids in contact with rough materials plays an important role in many microfluidic applications.
  - We will investigate the shape of the liquid–gas interface of water in contact with a realistic membrane geometry typically used for MD and try to answer the question if a flat liquid–gas interface is a reasonable assumption for such membranes.
  - Experiments by Xiao et al. [49] have shown that micropillars arranged in a periodic pattern and hydrophobic coatings, can mitigate scaling problems and prolong membrane lifetime. This is likely attributed to a state where the water remains in the elevated state and air is trapped between the

pillars. Using LB simulations and a theoretical approach we try to answer the question for which pillar geometry and droplet volumes a droplet switches from the elevated Cassie–Baxter state to the fully wetted Wenzel state. This is important because such surfaces are typically developed and tested by placing droplets on them and analyzing their contact angle and wetting behavior.

  - Oil transportation, water/oil separation, and thermal management of micro/power electronic systems, call for porous structures with the ability to retain low–surface–tension liquids against an imposed pressure difference. One micrometer geometry fabricated for such applications is a pillar–pore structure [1]. Therefore we try to derive an expression for the liquid–gas interface shape and the liquid entry pressure of such a geometry.

- Which partial vapor pressures can be expected inside the membrane and the air gap? Is the saturation vapor pressure a good assumption?

- Can we increase the evaporation (distilled water) flux of the AGMD module by specific surface treatments?

To answer the aforementioned research questions several studies have been conducted. This is a cumulative thesis, which is structured as follows: In chapter 2, I give an overview of the modeling and simulation of fluids in the context of MD. The focus lies on the Lattice Boltzmann method, which is suitable for the slip and transitional flow regime present in membrane pores, moreover the different transport models for a multi–component gas mixture are studied. Chapter 3 contains results published in the MDPI membranes journal with a focus on multiphase simulations within a realistic membrane geometry. This allows to determine the liquid–gas interface and the droplet distribution inside the porous membrane material. Chapter 4 contains the results of a second publication in the MDPI coatings journal, where we analyzed the liquid entry pressure (LEP) and the constant mean curvature of a hydrophobic pillar–pore structure. This is relevant to a wide range of applications, such as microfluidics and biochemical analysis. For many applications it is relevant to retain liquids behind or within rough structures, such as the pillar–pore structure, therefore a detailed understanding of the interface shape and the magnitude of the LEP is desirable. Chapter 5 presents the work published in the ACS Omega journal, in which we analyze the stability of droplets in the CB state on periodically pillared surfaces and compare existing theoretical predictions with LB multiphase simulations. A better understanding of the stability of droplets on micro pillars is important for MD, since such artificial surface roughness can prolong the lifetime

of a membrane used in MD. In chapter 6 we investigate the question of what level of saturation can be expected in the air gap of AGMD modules. Chapter 7 investigates two different surface functionalizations for membranes. After determining the liquid–gas interface for a liquid film in contact with the functionalized membrane surface, we evaluate the effect of the liquid distribution on the magnitude of the evaporation flux. The last chapter contains a conclusion on the comprised work of this thesis.

2

MODELLING OF FLUIDS IN THE CONTEXT OF MEMBRANE DISTILLATION

The fundamentals to describe fluids rely on a continuous framework or methods grounded on particle dynamics. In the continuum framework, continuous quantities such as velocity and density vary smoothly in space and time, while the particle dynamics approach considers the interaction between the individual particles (molecules). For large geometries compared to the mean free path length of a fluid particle, the continuum approach provides a good description of the fluid dynamics. The Knudsen number ($\mathrm{Kn} = \lambda / L$) serves as an important dimensionless quantity for characterizing the flow regime. Here λ denotes the mean free path length of a fluid particle and L represents the characteristic length associated with the flow [24]. Based on the Knudsen number, four flow regimes can be defined: continuum ($\mathrm{Kn} < 0.01$), slip ($0.01 < \mathrm{Kn} < 0.1$), transitional ($0.1 < \mathrm{Kn} < 10$) and free molecular ($\mathrm{Kn} > 10$) flow. In the context of MD, L corresponds to the diameter of the pores in the membrane, ranging from 200 nm to 450 nm, resulting in Knudsen numbers of about $Kn \approx 0.3 - 0.8$ for membranes typically used in MD [10].

In general, a distinction is made between a Lagrangian and an Eulerian description of the flow field. In the Eulerian framework, the fluid flow is observed through control volumes that are fixed in space, whereas in the Lagrangian description, the individual fluid parcels and their motion in the fluid field are observed and tracked.

In the continuum regime, the Euler and Navier–Stokes (NS) equations, partial differential equations (PDEs) describing conservation of mass, momentum and energy, provide an adequate description of the flow. Several approaches have been developed to numerically solve these nonlinear partial differential equations (PDEs). Common approaches are Finite Volume Method (FVM), Finite Element Method (FEM), Finite Difference Method (FDM), Spectral Method and Smoothed Particle Hydrodynamics (SPH) [34]. FVM and FEM solve the weak (integral) form of the PDEs. For both methods, space is divided into discrete cells. For the FVM the state variables (mass, momentum and energy density) in each cell are updated by fluxes between neighboring cells. FEM is a higher order method and uses a linear combination of basis function (typically polynomials) up to a certain order on each cell, to describe the state variables. The scalar coefficients involved in the linear combination are updated at each time step, based on numerical integration schemes such as the Runge–Kutta method. FVM conserves quantities such as mass, whereas FEM

does not. FEM has the advantage that for certain problems, increasing the order of the basis functions leads to better accuracy than simply increasing the number of cells. FDM also uses discrete cells, but approximates the derivative in the PDEs directly by finite differences. The Spectral method uses global ansatz functions such as a Fourier series [34]. The PDEs are transformed into the Fourier space. For the transform the efficient Fast Fourier Fransform (FFT) is utilized.

For free molecular flow, the motion of individual atoms is described. A common method is molecular dynamics simulation, where the atoms are treated as classical particles and Newton's equations of motion are solved for each atom.

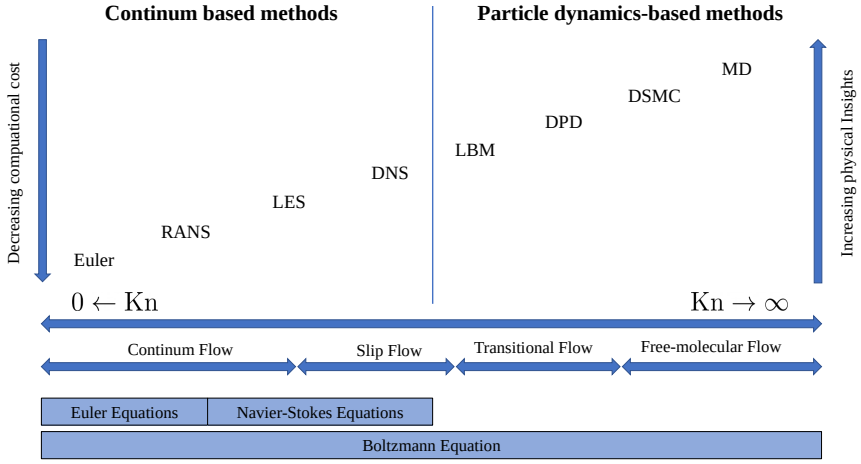

Figure 2.1: A hierarchy of modelling and simulation approaches [24].

A promising method to model slip and transitional flow is the Lattice Boltzmann (LB) method which is a particle dynamic–based method on the mesoscopic scale. Among the mesoscopic methods, one makes distinctions between lattice and particle based methods [40]. The LB method is suitable for the investigation of the flow within microporous membrane material, since the integration of complex boundary conditions is naturally supported by the LB schema due to its lattice based nature [50]. The LB method is also capable of modeling flow in the continuum flow regime since it recovers the Navier–Stokes in the hydrodynamic limit. Particle based mesoscopic methods are for example the Direct Simulation Monte Carlo (DSMC) method and the Dissipative Particle Dynamics (DPD) method [40]. Moving from left to right in figure 2.1, the resolution and the physical insights increase, but so does the computational cost.

2.1 VAPOUR TRANSPORT IN THE AIR GAP

2.1.1 *Fick's laws of diffusion*

Diffusion plays an important role in many scientific and engineering processes, including air gap membrane desalination where the separation process is driven by diffusion. The principle of diffusion, which describes the rate at which particles diffuse from regions with a high concentration to regions with a lower concentration, and can be modeled in a first approximation by Fick's law. The diffusive mass flux $\mathbf{j}$ is calculated based on the (mass) concentration gradient [6]. In the context of air gap membrane desalination, diffusion in general and Fick's law in particular are important for understanding the transfer of water vapor across a hydrophobic membrane and the air gap. The combination of evaporation and diffusion is utilized in membrane distillation to separate saltwater from fresh water. Fick's law helps to understand the fundamental factors influencing the diffusive transport of water vapor across the air gap and the membrane. These factors include the concentration gradient, the diffusion coefficient, and the thickness of the membrane and the air gap. Fick's law is expressed by the following equation [6, 14]:

$$\mathbf{j} = -D(\mathbf{x}) \nabla \rho(\mathbf{x}) \tag{2.1}$$

The dynamic process of diffusion is captured be the continuity equation:

$$\frac{\partial \rho}{\partial t} + \operatorname{div} \mathbf{j} = 0 \tag{2.2}$$

Where ρ is the mass concentration of one species in the bulk gas and $\mathbf{j}$ is the mass flux of the species [14]. In the context of air gap membrane distillation, the passively transported species is the water vapor and the bulk gas is dry air. It is important to note that in case of high vapor mass fractions which are possible at elevated temperatures, Fick's law, which is a passive scalar model, may not be applicable. In such scenarios, the vapor actively interacts with the overall gas flow, resulting in the breakdown of the simplified passive scalar modeling assumptions [39]. A more general description of diffusive transport is provided by the Stefan—Maxwell model [6, 14, 39].

Considering steady–state and a one dimensional problem, the mass diffusion equation simplifies to:

$$0 = \frac{\partial}{\partial x} \left(D(x) \frac{\partial \rho(x)}{\partial x} \right) \tag{2.3}$$

Where D is the diffusivity of vapor in dry air. D depends on the temperature, and therefore generally on x.

$$j(x) = -D(x)\frac{\partial \rho(x)}{\partial x} \tag{2.4}$$

If D is constant, the solution of equation 2.3 is linear and of the form:

$$\rho(x) = \frac{D}{j}x + \rho_0 \tag{2.5}$$

Where j is constant for the steady–state case.

$$j = -\frac{D}{d}(\rho_d - \rho_0) \tag{2.6}$$

If $D(x)$ depends on x, j must still be constant with respect to x for the steady state case (see equation 2.3). Integrating equation 2.4 one gets the following solution:

$$j\int_0^d \frac{1}{D(x)}\mathrm{d}x = -(\rho_d - \rho_0) \tag{2.7}$$

One can define:

$$v_D = \left[\int_0^d \frac{1}{D(x)}\mathrm{d}x\right]^{-1} \tag{2.8}$$

The "velocity" v_D is a measure of how fast vapor is transported from the evaporation to the condensation interface.

Since the AGMD module consists of different layers (such as membrane, air gap, hot and cold channels, ...) with different heat and mass diffusivities in series, an important special case is the 1D diffusion with different diffusion constants in series:

$$j = -D_{01}\frac{\rho_1 - \rho_0}{d_{01}} = -v_{D,01}(\rho_1 - \rho_0) \tag{2.9}$$

$$j = -D_{12}\frac{\rho_2 - \rho_1}{d_{12}} = -v_{D,12}(\rho_2 - \rho_1) \tag{2.10}$$

$$\rho_1 = \frac{v_{D,12}/v_{D,01}\rho_2 + \rho_0}{v_{D,12}/v_{D,01} + 1} \tag{2.11}$$

$$j = -\frac{v_{D,01}v_{D,12}}{v_{D,01} + v_{D,12}}(\rho_0 - \rho_2) = -v_{D,eff}(\rho_0 - \rho_2) \tag{2.12}$$

$$v_{D,eff} = \frac{v_{D,01} v_{D,12}}{v_{D,01} + v_{D,12}} = \frac{1}{\frac{1}{v_{D,01}} + \frac{1}{v_{D,12}}} \tag{2.13}$$

This can easily be extended to N different diffusion coefficients in series. For the continuum case $N \to \infty$, $\Delta x_i \to 0$ holds:

$$v_{D,eff}^{-1} = \sum_{i=1}^{N} \left(\frac{D(x_i)}{\Delta x_i} \right)^{-1} = \int_0^d \frac{1}{D(x)} \mathrm{d}x \tag{2.14}$$

2.1.2 *Maxwell-Stefan diffusion*

Maxwell–Stefan diffusion is a theoretical model which describes the transport of multiple components (species) in a fluid mixture. In contrast to Fick's law, which describes the diffusive transport of components in a bulk, it takes into account the interaction between individual components and provides a more accurate description of diffusion. Each component of the mixture is treated equally. Maxwell–Stefan diffusion is a very good approximation for gases at low density [6]. It considers the diffusivities D_{ij} between two species i and j and needs in total an input of $n/2(n-1)$ binary diffusivities for n species [6]. Mathematically, Maxwell–Stefan diffusion is characterized by a set of coupled partial differential equations, known as the Maxwell–Stefan equations, which govern the transport of each component in the mixture [6]. These equations take into account various factors such as the binary diffusivities, the molar flux $\mathbf{N_i}$, the velocity $\mathbf{v_i}$, the mole fraction X_i, and the molar concentration c_i of species i. The molar density of the solution is given by $c = \sum_i c_i$. By providing a more comprehensive description of diffusion than Fick's law, Maxwell–Stefan diffusion offers insights into the transport behavior and interactions among different species in a mixture. The Maxwell-Stefan equations are given by [6]:

$$\nabla x_i = -\sum_{\substack{j=1 \\ j \neq i}}^{n} \frac{X_i X_j}{D_{ij}} (\mathbf{v}_j - \mathbf{v}_i) = -\sum_{\substack{j=1 \\ j \neq i}}^{n} \frac{1}{c D_{ij}} \left(X_j \mathbf{N}_j - X_i \mathbf{N}_i \right) \tag{2.15}$$

Following the Clausius–Clapeyron or Antoine equation, the saturation vapor pressure, which represents the maximum amount of water vapor a gas mixture can hold, increases exponentially as the temperature rises. In other words, as the temperature goes up, the amount of water vapor which can be retained by the dry air also increases significantly. Specifically, for a temperature of about 80°C, at which MD modules are typically operated, the mass fraction of water vapor per carrier gas (dry air) can reach values up to 0.55 [39]. This shows that at a temperature of 80°C, the air has the capability to

hold a significant quantity of water vapor compared to its own mass. This indicates the need to use the Maxwell–Stefan equations, instead of relying solely on a passive scalar approach and Fick's law, when modeling diffusion in the specific scenario of AGMD modeling [39].

2.2 EVAPORATION AND CONDENSATION MODELS

The simplest approach to model evaporation is to treat the evaporation interface of the liquid as a boundary condition fixed in time and space. Several models have been developed to describe an evaporation surface. Assuming thermal equilibrium at the evaporation interface, the Hertz–Knudsen (HK) equation can be derived using classical kinetic theory. The HK equation gives an expression for the evaporation flux based on the partial vapor pressure above the evaporation interface [32].

Experiments showed discontinuities in the temperature field at the water evaporation interfaces [32]. Thermal equilibrium at the evaporation interface is therefore a simplification. The Hertz–Knudsen equation has two fitting parameters and they can vary by three orders of magnitude from setup to setup.

In contrast to the HK equation, the statistical rate theory (SRT) is free of fitting parameters and in good accordance with experiments [32]. Heat and mass transfer at the interface are coupled via SRT, which makes an implementation more difficult. The SRT includes a complex nonlinear equation that accounts for the temperature jumps at the interface and is valid also far from equilibrium.

An even more complete description of evaporation can be achieved by integrating the evaporation model directly into a numerical multiphase model, as it was done by Qin et al. [36]. They used a LB multiphase model with a non–ideal equation of state coupled to a Runge–Kutta method to model the heat/temperature transport. Qin et al. [36] were able to model the evaporation in a porous structure and achieved good agreement with experimental results. The benefit of this approach is that the evaporation interface is handled dynamically and allows to model non static liquid gas interfaces but comes with the drawback of a much higher computational cost since more complex multi–relaxation time LB models are involved.

Detailed studies of the evaporation of stationary droplets have shown that in the absence of heating, a model capturing diffusion alone is able to accurately predict the droplet evaporation. However, if the liquid is heated, a more sophisticated model that includes both diffusion and convection has to be used [7, 51], accounting for the mean bulk flow of the surrounding gas. This flow is known as Stefan flow, and is essential for an accurate description of evaporation [7]. Since the surrounding gas is dragged along with the evaporating liquid, a passive scalar diffusion model is not sufficient to capture the

characteristics of the flow. The evaporation of liquid at the liquid–gas interface also causes a vapor concentration gradient in the gas mixture, so a model including convection and diffusion is essential.

2.2.1 *Hertz–Knudsen and Hertz–Knudsen–Schrage equation*

A basic model for estimating the condensation and evaporation fluxes is the Hertz–Knudsen equation. By making an approximation that treats the vapor like an ideal gas which is in equilibrium with the liquid and the liquid–vapor interface, it is possible to establish the Hertz–Knudsen relation [32] stated in equation 2.16.

$$j_{HK} = \sqrt{\frac{m}{2\pi k_B}} \left[\frac{\sigma_e P_s(T_I^L)}{\sqrt{T_I^L}} - \frac{\sigma_c p^V}{\sqrt{T_I^V}} \right] \tag{2.16}$$

m is the mass of the evaporating molecule, k_B is the Boltzmann constant, $P_s(T_I^L)$ the vapor pressure at saturation, p^V is the vapor pressure above the evaporation interface, T_I^L the temperature of the liquid at the liquid–gas interface and T_I^V the temperature of the vapor at the liquid–gas interface. j is a mass flux ($\mathrm{kg\,m^{-2}\,s^{-1}}$). The evaporation and condensation coefficients σ_e and σ_c are dimensionless parameters that depend on the experimental setup. In experiments conducted for water, the σ parameters showed a range spanning from 10^{-3} to 1 [32].

Schrage argued that for a net flux of evaporation, the velocity distribution of the molecules departing from the liquid–gas interface differs from the molecules colliding with the interface. Therefore he proposed that the evaporating and condensing molecules exhibit a Maxwellian velocity distribution which is shifted by a mean velocity. As a result, he proposed a modification to the HK relation, commonly known as the Hertz–Knudsen–Schrage (HKS) equation [32].

$$j_{HKS} = \frac{2}{2-\sigma_c} \sqrt{\frac{m}{2\pi k_B}} \left[\frac{\sigma_e P_s(T_I^L)}{\sqrt{T_I^L}} - \frac{\sigma_c p^V}{\sqrt{T_I^V}} \right] \tag{2.17}$$

It should be noted that the HK and the HKS equation do not yield a complete description of evaporation processes and may lead to incorrect predictions. Temperature discontinuity at the interface are measured in experiments which contradicts the basic assumption of thermal equilibrium [32]. Moreover, the evaporation coefficient (σ_e) and the condensation coefficients (σ_c) can vary depending on the experimental setup, e.g. the velocity of the hot water flow, and the contamination of the water [37]. Many publications assume that $\sigma_e = \sigma_c$ and $T_I^L = T_I^V$, but this may not be the case [32].

2.3 LIOUVILLE AND BOLTZMANN EQUATION

The underlying theory for the LB method is the Boltzmann equation (BE), describing the kinetics of the one–body distribution function f [44].

$$\frac{\partial f}{\partial t} + \mathbf{p}/m \cdot \nabla f + \mathbf{F} \cdot \nabla_{\mathbf{p}} f = C_{12} \tag{2.18}$$

This equation originates from the Liouville equation for the N–body distribution function (f_N). By integration over parts of the variables of f_N one ends up with the s–body distribution function f_s.

$$f_s(\mathbf{r}_1 \dots \mathbf{r}_s, \mathbf{p}_1 \dots \mathbf{p}_s, t) = \int f_N(\mathbf{r}_1 \dots \mathbf{r}_N, \mathbf{p}_1 \dots \mathbf{p}_N, t)\, d\mathbf{r}_{s+1} \dots d\mathbf{r}_N d\mathbf{p}_{s+1} \dots d\mathbf{p}_N \tag{2.19}$$

Integration of the Liouville equation over the variables r_2 ... r_N and p_2 ... p_N one gets the kinetic equation for the one–body distribution function $f = f_1$ which has the units $\mathrm{kg} \times \mathrm{m}^{-3} \times (\mathrm{m/s})^{-3}$. $f(\mathbf{r}, \mathbf{p}, t)$ expresses the mass density of a particles at position $\mathbf{r}$ at time t with with momentum $\mathbf{p}$. Therefore $f(\mathbf{r}, \mathbf{p}, t)\mathrm{d}\mathbf{r}\mathrm{d}\mathbf{v}$ is the mean mass in a phase–space volume $\mathrm{d}\mathbf{r}\mathrm{d}\mathbf{v}$ at position $\mathbf{r}$ with momentum $\mathbf{p}$ at time t.

$\mathbf{F}$ is an external force and C_{12} describes the collisions between particles and is a statistical term. C_{12} contains an integral of $f_2 = f_2(\mathbf{r}_1, \mathbf{p}_1, \mathbf{r}_2, \mathbf{p}_2, t)$ that describes the probability to observe particle one at position $\mathbf{r}_1$ with impulse $\mathbf{p}_1$ and particle two at position $\mathbf{r}_2$ with impulse $\mathbf{p}_2$ at time t. To solve f, one has to know f_2, which requires to solve f_3 and so on until finally reaching the Liouville equation. This is known as the BBGKY hierarchy [44] which links f_n to f_{n+1}. If f_{n+1} can be modelled one can finally solve for f_n. For $n = 1$ and an appropriate approximation of f_2 this leads to the Boltzmann equation.

A key assumption to obtain the Boltzmann equation is the molecular chaos hypothesis. It assumes for all the particles in a fluid "molecular chaos" which means that the velocity of colliding particles are uncorrelated and independent of the position. This finally leads to the simplification $f_2 = f(\mathbf{r_1}, \mathbf{p_1}) f(\mathbf{r_2}, \mathbf{p_2})$. Combining this with the BBGKY hierarchy one can derive the Boltzmann equation for dilute gases given in equation 2.20, which is not shown here.

In the Boltzmann equation in 2.20 the left side reflects the reversible Newtonian single–particle dynamics and the right side represents the interactions (collisions) between the particles (C_{12}).

$$\frac{\partial f}{\partial t} + \mathbf{v} \cdot \nabla f + \mathbf{F} \cdot \nabla_{\mathbf{p}} f = \int (f(\mathbf{r}_1', \mathbf{p}_1', t) f(\mathbf{r}_2', \mathbf{p}_2', t) - f(\mathbf{r}_1, \mathbf{p}_2, t) f(\mathbf{r}_2, \mathbf{p}_2, t)) h \Lambda(h, \Omega) \mathrm{d}\Omega \mathrm{d}\mathbf{p}_2 \tag{2.20}$$

C_{12} involves a complex integral which includes the differential cross section Λ of the two body collision, the solid angle Ω and $h = |\mathbf{p}_1 - \mathbf{p}_2| = |\mathbf{p}_1' - \mathbf{p}_2'|$. Primed values are the values after the collision and non primed before the collision [44].

At local equilibrium the collision term on the right side has to vanish which leads to the detailed balance condition:

$$f(\mathbf{r}_1', \mathbf{p}_1', t) f(\mathbf{r}_2', \mathbf{p}_2', t) = f(\mathbf{r}_1, \mathbf{p}_2, t) f(\mathbf{r}_2, \mathbf{p}_2, t) \tag{2.21}$$

Taking the logarithms yields:

$$\ln(f(\mathbf{r}_1', \mathbf{p}_1', t)) + \ln(f(\mathbf{r}_2', \mathbf{p}_2', t)) = \ln(f(\mathbf{r}_1, \mathbf{p}_2, t)) + \ln(f(\mathbf{r}_2, \mathbf{p}_2, t)) \tag{2.22}$$

The quantity $\ln(f)$ is therefore a additive collision invariance [44]. During the collisions the mass, momentum and energy are conserved. Therefore $\ln(f)$ can be written as: $\ln(f) = A \cdot m + \mathbf{B} \cdot m\mathbf{v} + C \cdot \frac{m}{2}\mathbf{v}^2$ From this equation the Maxwell–Boltzmann equilibrium distribution can be obtained by imposing the conservation of mass, momentum and energy [44]:

$$\int f \mathrm{d}\mathbf{v} = \rho \tag{2.23}$$

$$\int f \mathbf{v} \mathrm{d}\mathbf{v} = \rho \mathbf{u} \tag{2.24}$$

$$\int f \mathbf{v}^2 / 2 \mathrm{d}\mathbf{v} = \rho e \tag{2.25}$$

The Maxwell–Boltzmann distribution is stated below. Note that ρ is the mass density of the fluid.

$$f^{eq}(\mathbf{v}) = \rho (2\pi v_t^2)^{-D/2} \exp\left(-\frac{(\mathbf{v} - \mathbf{u})^2}{2v_T^2}\right) \tag{2.26}$$

Where $v_T = \sqrt{k_B T / m}$ is the thermal velocity, T the temperature, $\mathbf{u}$ the mean velocity, $\boldsymbol{\xi} = \mathbf{v} - \mathbf{u}$ the relative velocity and m the mass of a particle. For a global equilibrium $\mathbf{u}$ and v_T (T) needs to be constant in space and time. In general the hydrodynamical fields (like the macroscopic velocity $\mathbf{u}$) can change in time and space on a macroscopic scale, nevertheless the Maxwell–Boltzmann (MB) equilibrium distribution 2.23 is locally fulfilled, which refers to local equilibrium. Local means that for a sufficient small volume and a sufficient small

time frame $\mathbf{u}$ can be assumed to be constant. Maxwellian equilibria fulfill translational and rotational invariance [44].

The collision operator from the Boltzmann equation in 2.20 involves a complex integral, therefore both the theoretical and the numerical treatment of the Boltzmann equation are very complex. Moreover the collision operator for the Boltzmann equation is only valid for dilute gases.

In general the collision operator C_{12}, from equation 2.18, has to conserve mass, momentum and for the monoatomic case also energy. Which is expressed through [20]:

$$\int C_{12} \mathrm{d}^3 v = 0 \tag{2.27}$$

$$\int \mathbf{v} C_{12} \mathrm{d}^3 v = 0 \tag{2.28}$$

$$\int |\mathbf{v}|^2 C_{12} \mathrm{d}^3 v = 0 \tag{2.29}$$

Besides the conservation laws, the collision operator has to guarantee that the one–body distribution function f converges locally to its equilibrium [20]. The simplest operator to approximate C_{12} which fulfils these conditions is the BGK collision operator [20].

$$C_{12} \approx -\frac{f - f^{eq}}{\tau} \tag{2.30}$$

Locally f is relaxed exponentially towards f^{eq} [20].

$$f(\mathbf{v}, t) = f^{eq}(\mathbf{v}) + (f(\mathbf{v}, 0) - f^{eq}(\mathbf{v}))e^{-t/\tau} \tag{2.31}$$

It should be noted that the BGK collision operator predicts a Prandtl number of $\mathrm{Pr} = 1$ whereas experiments predict a value of $\mathrm{Pr} \approx 2/3$ [20]. From the definition of the BGK collision operator and the conservation of mass, momentum and energy follows directly that the equilibrium distribution has to fulfill certain conditions:

$$\int f^{eq} \mathrm{d}\mathbf{v} = \int f \mathrm{d}\mathbf{v} = \rho \tag{2.32}$$

$$\int f^{eq} \mathbf{v} \mathrm{d}\mathbf{v} = \int f \mathbf{v} \mathrm{d}\mathbf{v} = \rho \mathbf{u} \tag{2.33}$$

$$\int f^{eq} \mathbf{v}^2/2 \mathrm{d}\mathbf{v} = \int f \mathbf{v}^2/2 \mathrm{d}\mathbf{v} = \rho e \tag{2.34}$$

Integrating the Boltzmann equation (2.20) over velocity space, one finds the continuity equations which describes the mass conservation on the macroscopic scale. If the BE is multiplied by v_a before integration over velocity space, the Cauchy momentum equation is recovered, which describes the conservation of momentum on a macroscopic scale. And the stress tensor is identified by:

$$\sigma_{ab} = -\int \xi_a \xi_b f d\mathbf{v} \tag{2.35}$$

When multiplying by $v_a v_a$ before integrating over velocity space the total energy equation is recovered, which describes the conservation of energy on a macroscopic scale. And the heat flux $\mathbf{q}$ is identified by:

$$q_b = -\int \xi_a \xi_a \xi_b f d\mathbf{v} \tag{2.36}$$

Applying the Chapman-Enskog analysis

$$f = f^{eq} + f^{neq} = f^{eq} + \mathrm{Kn}^1 \cdot f^{(1)} + \mathrm{Kn}^2 \cdot f^{(2)} + ... \tag{2.37}$$

f is expanded around the local equilibrium f^{eq} in terms of the Knudsen number. For $\mathrm{Kn} \to 0$ the Euler equations are recovered which implies that viscous dissipation and heat diffusivity are linked to the non–equilibrium [20]. The Navier-Stokes-Fourier model, including viscous stress and heat conduction, can be obtained through a first-order approximation of f, which is not shown here.

2.3.0.1 *H–Theorem*

With the H–Theorem by Boltzmann one can define the entropy [44].

$$H(t) = -\int f(\mathbf{v}, t) \ln(f(\mathbf{v}, t)) \mathrm{d}^3 v \tag{2.38}$$

$H(t)$ is a quantity which increases monotonously if the one body distribution function f follows the BE. This is also the case if the collision term is approximated by the BGK collision operator.

2.4 LATTICE BOLTZMANN METHOD

To get a discrete form of the BE one needs to discretise the phase space. This includes a discretisation of the space and the momentum (velocity). Leading to the Lattice Boltzmann (LB) equation given in equation 2.39.

$$f_i(\mathbf{r} + \mathbf{c_i}\Delta t, t + \Delta t) = f_i(\mathbf{r}, t) + \Omega_{ij}(f_j^{eq}(\mathbf{r}, t) - f_j(\mathbf{r}, t)) \tag{2.39}$$

The external force **F** is set to zero for the moment and the complex collision integral was replaced by a relaxation to a local equilibrium $f_j^{eq}(\mathbf{r}, t)$. $f_i(\mathbf{r}, t)$ expresses the density of particles at position **r** at time t and with velocity c_i. The index i stands for a set of discrete velocities ($i = 0, ..., b$). A common choice for the velocity discretisation in two dimensions is the 9–speed lattice (D2Q9) and in 3 dimensions the 19– or 27–speed lattice (see figure 2.2). Moreover the space (**r**) is divided into discreet lattice cells.

The LB method is performed in two steps. First the collision step is calculated which updates the f_is on every lattice node according to the right side in equation 2.39. After that the streaming step is executed which updates the f_is on the whole lattice according to the left side of equation 2.39 which effectively streams the f_is to their corresponding neighboring lattice node.

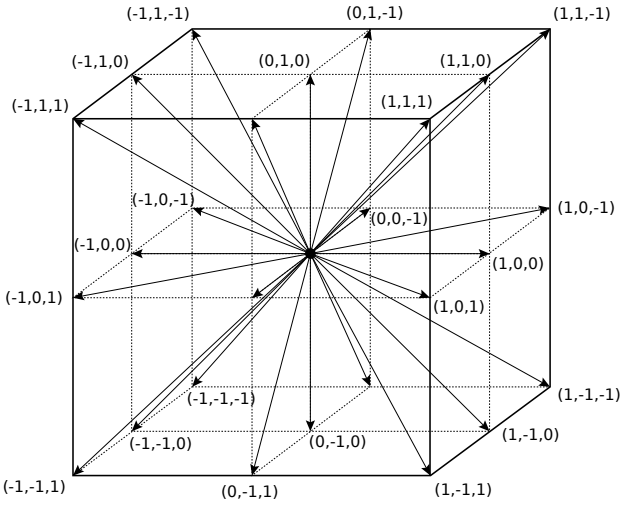

Figure 2.2: D3Q27 lattice discretization, 27 Discrete velocity $\mathbf{c}_i$ with $i = 0, ..., 26$ in a 3 dimensional space [16].

A further simplification is to approximate Ω_{ij} with δ_{ij}/τ. Here τ is the relaxation time. This is the above mentioned BGK approximation. Often the local equilibrium distribution f^{eq} is approximated by a second order expansion (in the local Mach-number) of the Maxwell–Boltzmann distribution and needs to fulfill certain conditions to ensure the conservation of mass and momentum, as well as the isotropy of space (angular momentum conservation). This standard isothermal model is not invariant to Galilean transformations, lacks rotational isotropy moreover the speed of sound is fixed to $c_s^2 = 1/3$ [44, 45].

$$f_i^{eq}(\mathbf{r}, t) = w_i \rho \left(1 + \frac{u_a c_{ia}}{c_s^2} + \frac{u_a u_b Q_{iab}}{2c_s^4}\right) \tag{2.40}$$

Where $Q_{iab} = c_{ia}c_{ib} - c_s^2 \delta_{ab}$ represents the quadrupole projector along the i-the direction [45]. Analog to the continuous case the macro-

scopic quantities like density (ρ) and velocity ($\mathbf{u}$) are calculated by a sum over the full discreet velocity space.

$$\rho = \sum_i^b f_i = \sum_i^b f_i^{eq} \tag{2.41}$$

$$\rho \mathbf{u} = \sum_i^b f_i \mathbf{c}_i = \sum_i^b f_i^{eq} \mathbf{c}_i \tag{2.42}$$

As for the continuous case, the BGK collision operator puts some constraints on the f_i^{eq}s to ensure the conservation of mass and momentum. Furthermore, the rotational isotropy of the lattice must be guaranteed up to the fifth order, which requires that all moments of the weights w_i up to the fifth order are isotropic [20]. This is necessary to recover the Navier–Stokes equation. Therefore, the weights w_i from the equilibrium distribution must satisfy the following conditions [20]:

$$\sum_i w_i = 1 \tag{2.43}$$

$$\sum_i w_i c_{ia} = 0 \tag{2.44}$$

$$\sum_i w_i c_{ib} c_{ia} = \delta_{ab} c_s^2 \tag{2.45}$$

$$\sum_i w_i c_{ib} c_{ia} c_{ic} = 0 \tag{2.46}$$

$$\sum_i w_i c_{ib} c_{ia} c_{ic} c_{id} = c_s^4 (\delta_{ab}\delta_{cd} + \delta_{ad}\delta_{bd} + \delta_{ad}\delta_{bc}) \tag{2.47}$$

$$\sum_i w_i c_{ib} c_{ia} c_{ic} c_{id} c_{ie} = 0 \tag{2.48}$$

Moreover the weights w_i have to be positive. Therefore for D3Q27 one obtains for the weights w_i:

$$\begin{aligned} w_i = [&8/27, 2/27, 2/27, 2/27, \\ &2/27, 1/54, 1/54, 1/54, 1/54 \\ &2/27, 1/54, 1/54, 1/54, 1/54, \\ &1/216, 1/216, 1/216, 1/216, \\ &2/27, 1/54, 1/54, 1/54, 1/54, \\ &1/216, 1/216, 1/216, 1/216] \end{aligned} \tag{2.49}$$

The momentum–flux tensor ($\mathbf{P}$) is given by:

$$\mathbf{P} = \sum_{i}^{b} f_i \mathbf{c}_i \mathbf{c}_i \tag{2.50}$$

The trace of the momentum–flux tensor P_{aa} corresponds to the fluid energy. The off-diagonal elements of $\mathbf{P}$ represent the fluid shear. The Mach–number is given by $\mathrm{Ma} = |\mathbf{u}|/c_s$, where c_s is the speed of sound which depends on the specific choice of the discrete lattice speeds $\mathbf{c}_i$ (compare equation 2.45) [45]. Chapman and Cowling [8] showed that in the limit of long–wavelengths, when compared to the lattice scale equation 2.39 simplifies to the Navier–Stokes equation, closed by an ideal equation of state

$$p(\rho) = \rho c_s^2 \tag{2.51}$$

And the kinematic viscosity

$$\nu = c_s^2(\tau - \Delta t/2) \tag{2.52}$$

Even if the LB method origins from the BE which is only valid for dilute weakly interacting gases, it can be also applied to strongly interacting particles as for example in liquids. This is possible since in the LB framework the elementary degrees of freedoms (individual particles) are cast into a system with a reduced collective degree of freedom [45]. Every lattice point describes a set of particles and the collision operator in the lattice BGK approximation is a fairly general approximation of the collision term in the BE. The lattice BGK approximation assumes only an attraction to local equilibrium and that for a small perturbation the process can be described by a relaxation process with relaxation time τ, which depends on the viscosity and is valid for a wide range of fluids [45].

According to equation 2.40 it is clear that the standard LB method is only able to capture week compressions, since f_{eq} in equation 2.40 is a second order expansion and therefore density and pressure changes up to $O(\mathrm{Ma}^2)$ are supported. Higher pressure gradients can be modelled by including an additional external force term ($\mathbf{F}_{ext} = -\nabla p$). An ideal equation of state does not mean that incompressible flow is not supported within the LB schema. For an incompressible flow only $\mathrm{div}(\mathbf{u}) = 0$ has to be fulfilled.

The lattice Boltzmann method is able to describe flow and transport processes on micro/nano–meter scales due to its particle dynamic based nature. But not only on such small scales the LB method has been applied successfully [22], it also provides a viable alternative for the Navier–Stokes solvers from traditional CFD for weakly compressible flows (low Mach number) at a macroscopic scale. Therefore the LB

method allows to simulate flow from the continuum to the transitional flow regime. The advantage over the Navier–Stokes equation is its computational efficiency and it's simple, straight forward implementation, which allows a good parallelization. Only the local collision term is non–linear, whereas the transport term for the Navier–Stokes equation is non–local and non–linear [45]. Moreover complex boundary conditions can be modelled easily [45]. Disadvantage of the standard LB method is its limitation to an isothermal flow. There exist several approaches to extent the LB method to get a consistent description of the internal energy and non–isothermal flows. Moreover the LB method is limited to uniform quadratic grids.

2.4.1 *Lattice Boltzmann Unit System*

The LB method is commonly simulated using a similarity approach rather than SI units. Thus, according to the LB unit convention, one chooses for the time step $\Delta t = 1\,\mathrm{ts}$, for the lattice spacing $\Delta x = 1\,\mathrm{lu}$ and for the fluid particle mass $m = 1\,\mathrm{mu}$. Here "ts" stands for time step, "lu" for lattice unit and "mu" for mass unit.

From the conditions 2.43 to 2.48 follows for most of the velocity discretisation, for example D2Q9, D3Q19 and D3Q27, that $c_s = c/\sqrt{3}$. Where $c = \Delta x/\Delta t$ is the lattice speed [44]. In the LB unit system for a single component problem holds $c = 1\,\mathrm{lu/ts}$ and thus $c_s = 1/\sqrt{3}\,\mathrm{lu/ts}$. The equation of state simplifies to $p = \rho/3$ and fixes $k_B T/m = 1/3$ in the LB unit system.

For a multi component gas the equation of state of an ideal gas for each individual species j holds:

$$c_{sj}^2 = p_j/\rho_j = k_B T/m_j \tag{2.53}$$

For the isothermal case follows immediately $c_{sj} \propto 1/\sqrt{m_j}$ where m_j is the particle mass, p_j the partial pressure and ρ_j the mass concentration of each species j. The condition for the speed of sound gives $c_{sj} = c_j/\sqrt{3}$ for each species j. For component 1 we can set in the LB unit system $m_1 = 1\,\mathrm{mu}$ and therefore $k_B T = 1/3$ and $c_1 = 1\,\mathrm{lu/ts}$, similar to the single component case. For component 2 follows $m_2 \neq 1$ since the real particle mass ratio (m_2/m_1) has to be maintained. Therefore $c_2 = 1/\sqrt{m_2}\,\mathrm{lu/ts}$ and as a consequence during one time step (Δt) component 2 does not stream to the next lattice node but ends up between two lattice points which makes interpolation necessary.

2.4.1.1 *Unit Conversion*

In the following section quantities with a superscript "$*$" are in LB units and quantities without are in SI units.

$$L^* = L/\Delta x \tag{2.54}$$

and

$$t^* = t/\Delta t \tag{2.55}$$

$$\frac{u^*}{u} = \frac{\Delta t}{\Delta x} \tag{2.56}$$

$$\mathrm{Re} = \frac{uL}{\nu} = \frac{u^* L^*}{\nu^*} \tag{2.57}$$

The ratio of inertial to viscous forces defines the Reynolds number given in equation 2.57 [21]. Rearranging equation 2.57 one can show that the following equation holds:

$$\frac{\nu^*}{\nu}\Delta x = \frac{u^*}{u} = \frac{\Delta t}{\Delta x} \tag{2.58}$$

Finally one can calculate Δt:

$$\Delta t = \frac{\nu^*}{\nu}\Delta x^2 \tag{2.59}$$

For a given ν^*, one needs the actual Reynolds (Re) number of the problem, to calculate for example the inlet velocity u^* in LB units. u is the corresponding inlet velocity in SI units and L the inlet diameter in SI units of the problem.

In the case of a diffusive and convective transport with diffusion coefficient D and convective velocity u, the Péclet number (Pe) can be used to calculate the diffusion coefficient in LB units (D^*). Pe is the ratio of the advective transport rate to the diffusive transport rate [21].

$$\mathrm{Pe} = \frac{uL}{D} = \frac{u^* L^*}{D^*} \tag{2.60}$$

Finally one gets:

$$D^* = \frac{u^* L^*}{\mathrm{Pe}} = D\frac{\Delta t}{\Delta x^2} \tag{2.61}$$

The Schimdt number (Sc) is defined as the ratio of the momentum diffusivity to the mass diffusivity.

$$\mathrm{Sc} = \frac{\nu}{D} = \frac{\mu}{\rho D} = \frac{\nu^*}{D^*} \tag{2.62}$$

$$D^* = D\frac{\nu^*}{\nu} \tag{2.63}$$

For the multiphase case the Bond number (Bo), Laplace number (La) and the Capillary number (Ca) are of importance. The Bond number represents the ratio of gravitational to capillary forces [21]. For a low Bond number (Bo $\ll 1$) gravitational effects can be neglected. Moreover the Bond number can also be used to calculate the gravitational constant in lattice units.

$$\mathrm{Bo} = \frac{F_{volume}}{F_{surface}} \tag{2.64}$$

If there is a gravitational force, it holds:

$$\mathrm{Bo} = \frac{\Delta\rho g L^2}{\gamma} = \frac{\Delta\rho^* g^* L^{*2}}{\gamma^*} \tag{2.65}$$

From this follows:

$$g^* = g\frac{\Delta\rho\gamma^*\Delta x^2}{\Delta\rho^*\gamma} \tag{2.66}$$

The capillary number represents the comparative effect of viscous drag forces versus surface tension forces acting at an interface between a liquid and a gas [21]. This factor is particularly important in dynamic events such as the collision of two droplets.

$$\mathrm{Ca} = \frac{\nu_l\rho_l u}{\gamma} = \frac{\nu_l^*\rho_l^* u^*}{\gamma^*} \tag{2.67}$$

$$\Delta t = \Delta x\frac{\gamma^*\nu_l\rho_l}{\gamma\nu_l^*\rho_l^*} \tag{2.68}$$

The Laplace number can be used to characterize the processes of fluid spraying (atomization) in a two–phase flow. It relates inertial and surface tension forces to viscous forces [21].

$$\mathrm{La} = \frac{\gamma\rho_l L}{(\eta_l)^2} \tag{2.69}$$

It can be used to convert the surface tension from LB units to SI units.

$$\mathrm{La} = \frac{\gamma\rho_l L}{(\eta_l)^2} = \frac{\gamma^*\rho_l^* L^*}{(\eta_l^*)^2} \tag{2.70}$$

$$\gamma = \frac{\gamma^*\rho_l^*(\eta_l)^2}{\Delta x\rho_l(\eta_l^*)^2} \tag{2.71}$$

Pressure units can be converted as follows:

$$p = p^*\frac{\gamma}{\gamma^*\Delta x} \tag{2.72}$$

2.4.2 *Guided equilibrium*

In this study, the guided equilibrium (GE) equation introduced in previous works [35, 39] was employed. The GE function can be derived through the minimization of the entropy function while upholding four conditions, which ensure the preservation of mass, momentum and energy, combined with an extra condition related to the pressure tensor, which was necessary to retrieve the Navier–Stokes equations [35]. The outcomes can be formulated in the subsequent manner:

$$f_i^{eq}(\rho, \mathbf{u}, T) = \rho \prod_{\alpha=x,y,z} \frac{1 - 2c_{i\alpha}^2}{2^{c_{i\alpha}^2}} \left(c_{i\alpha}^2 - 1 + c_{i\alpha}u_\alpha + u_\alpha^2 + T\right) \tag{2.73}$$

The LB method with the guided equilibrium equation distribution restores the Galilean invariance and therefore provides a more accurate solution [35] compared to the standard second order expansion of the Maxwell-Boltzmann distribution.

2.4.3 *External force*

In order to include a force $\mathbf{F}_{tot}$ into the LB method, several schemes have been developed. All of the schemes incorporate the force either by modifying the velocity which is used to compute the equilibrium distribution, or by an additional term in the collision operator, or both. We have chosen to use the original Shan–Chen forcing scheme, which recovers the correct macroscopic behavior and has a simple and straightforward implementation, since it only requires the velocity to be modified [20, 41, 42].

$$\mathbf{u} = \frac{1}{\rho} \sum_{i=0}^{26} f_i \mathbf{c}_i + \frac{\tau \mathbf{F}_{tot}}{\rho} \tag{2.74}$$

2.4.4 *Multiphase*

LB multiphase models can typically be categorized into five main types: the color–gradient method, the free–energy method, the phase–field method, entropic LB method and the pseudopotential method [23].

Gunstensen et al. [12] introduced the color–gradient LB technique, which utilizes two separate distribution functions with different "colors" to represent two distinct fluid phases. In addition to the normal collision operator, this method incorporates an extra collision operator that creates the surface tension at the liquid–gas interface [23].

The free–energy LB method, introduced by Swift et al. [46, 47], incorporates a non–ideal thermodynamic pressure tensor to describe the separation of the phases. However, it lacks Galilean invariance

and does not recover the Navier–Stokes equation equation correctly. This can be resolved by adding correction terms to the equilibrium distribution function, similar correction terms are needed in the color–gradient LB models [23].

The phase–field LB method belongs to the category of multiphase LB models, which utilize the phase–field theory to describe the time evolution of the interface by using an order parameter determined by e.g. the Cahn–Hilliard equation [23].

The entropic LB method applies an entropic stabilization mechanism to control the dynamics at the liquid–gas interface and leads to a thermodynamic consistent description of the multi phase flow [25].

The pseudopotential multiphase LB method, developed by Shan and Chen [41, 42], is the simplest approach among multiphase LB methods. This method simulates fluid–fluid interactions using an interparticle pseudo potential, enabling automatic separation of fluid phases or components without the need for interface tracking or capturing techniques. Although the interparticle potential results in a non–ideal pressure tensor, it differs from the one used in the free-energy LB method [23]. The main draw back of this model are spurious non physical currents that appear near to the interface. The pseudopotential LB method has gained consiberable popularity in the multiphase LB community because of its straightforward concept, easy implementation and computational efficiency, and it has been successfully applied to various problems [23]. Furthermore, the pseudopotential method can be easily extended by a fluid–solid interaction, which allows to tune the hydrophobicity of the solid by adjusting a model parameter. This, together with the ability to handle complex boundary conditions, makes the model particularly useful for multiphase flows in the context of MD. Therefore the Chan–Chen pseudo potential multiphase model was chosen. Implementation details can be fond in chapter 3.

2.4.5 *Multicomponent*

In chapter 2, it was discussed that modeling diffusion at high temperatures necessitates solving the Stefan–Maxwell equations to account for mass diffusion correctly, the passive scalar approach mathematically described by Fick's law is not applicable anymore. This is due to the significant saturation mass ratio of water vapor to dry carrier gas, which can reach up to 0.55 (kg water vapor/kg dry air) at 80°C [39]. Therefore, a multicomponent LB model introduced in [5, 39] was applied and two separate LB equations are integrated over time for each individual gas component. This provides a more complete description of the hydrodynamics for water vapor and carrier gas (dry air), including the phenomena of diffusion and convection. This multicomponent model enables the independent determination of dry air velocity and

water vapor velocity. This is the biggest difference when compared to passive scalar models, which impose the velocity of the carrier gas on the vapor [39]. In contrast to the BGK single relaxation time approach, the multicomponent model from Arcidiacono et al. [5] features two relaxation times per species, one attributed to the viscosity and the other one attributed to the binary diffusion coefficient (D_{jk}). The dynamic of each species j is modeled by the following discreet LB equations [5, 39]:

$$\partial_t f_{ij} + \tilde{c}_{ij\alpha}\partial_\alpha f_{ij} = -\frac{1}{\tau_{j1}}(f_{ij} - f^*_{ij}) - \frac{1}{\tau_{j2}}(f^*_{ij} - f^{eq}_{ij}),\ \alpha = x, y, z \quad (2.75)$$

For the equilibrium distribution of each species, the GE distribution introduced earlier is used again [5, 39]:

$$f^{eq}_{ij} = f^{eq}_{ij}(\rho, \mathbf{u}, T) = \rho \prod_{\alpha=x,y,z} \frac{1 - 2c^2_{ij\alpha}}{2^{c^2_{ij\alpha}}} \left(c^2_{ij\alpha} - 1 + \tilde{c}_{ij\alpha}u_\alpha + u^2_\alpha + T\right) \quad (2.76)$$

For the lattice velocity of species j holds $\mathbf{c}_{ij} = \mathbf{c}_i/\sqrt{m_j}$ and for each spacial direction $\alpha = x, y, z$ holds $c_{ij\alpha} = c_{i\alpha}/\sqrt{m_j}$. Here $\mathbf{c}_i$ represents the lattice velocity form the spacial discretisation of the domain. ρ and $\mathbf{u}$ are bulk velocity and bulk density respectively [39]. m_j is the molecular mass of species j. ρ_j and u_j represent the density and velocity of species j respectively. Moreover $f^*_{ij} = f^{eq}_{ij}(\rho, \mathbf{u_j}, T)$ [39].

$$\rho_j = \sum_i f_{ij}, \qquad \rho_j \mathbf{u}_j = \sum_i \mathbf{c}_{ij} f_{ij} \quad (2.77)$$

$$\rho = \sum_j \rho_j, \qquad \rho\mathbf{u} = \sum_j \rho_j \mathbf{u}_j \quad (2.78)$$

τ_{j1} and τ_{j2} are calculated as follows:

$$\tau_{j1} = \frac{\mu_j}{p \sum_{k \neq j} X_k \phi_{jk}} \quad (2.79)$$

$$\phi_{jk} = \frac{1}{\sqrt{8}} \left(1 + \frac{m_j}{m_k}\right)^{-1/2} \left[1 + \left(\frac{\mu_j}{\mu_k}\right)^{1/2} \left(\frac{m_k}{m_j}\right)^{1/4}\right]^2 \quad (2.80)$$

$$\tau_{j2} = \frac{\rho_j}{p_j} D_{jm} \quad (2.81)$$

$$D_{jm} = \frac{1 - \rho_j/\rho}{p \sum_{k \neq j} X_k / D_{jk}} \tag{2.82}$$

It should be noted that equation 2.81 is only an approximation and the definition of τ_{j1} and τ_{j2} is only valid if the momentum differences is the slow variable. If the pressure is the slow variable it holds [5]:

$$\tau_{j2} = \frac{\mu_j}{p \sum_{k \neq j} X_k \phi_{jk}} \tag{2.83}$$

$$\tau_{j1} = \frac{\rho_j}{p_j} D_{jm} \tag{2.84}$$

In any case $\tau_{j1} \leq \tau_{j2}$ has to be fulfilled.
For the multicomponent case the equation of state becomes [5]:

$$p = \beta RT \tag{2.85}$$

Here $\beta = \sum_j \beta_j$ is the total molar concentration of the mixture in mol per volume. p is the pressure of the ideal gas mixture, X_j and Y_j represent the molar and the mass fraction of species j [5].

The streaming step for the multi component case involves interpolation if one particle mass is unequal to zero. The reason for this is that during Δt the f_{ij}s will stream to a point in space which lies between two lattice nodes of the domain, since $c_{ij\alpha} \neq c_{i\alpha}$ if $m_j \neq 1$. Following the work from [39] the following second order interpolation is use for the streaming step:

$$\begin{aligned} f_{ij}(\mathbf{r} + \mathbf{c_i}\Delta t, t + \Delta t) = \hat{f}_{ij}(\mathbf{r}, t) + \frac{1}{2}\left(\hat{f}_{ij}(\mathbf{r} + \mathbf{c_i}, t) - \hat{f}_{ij}(\mathbf{r} - \mathbf{c_i}, t)\right)\phi \\ + \left(\hat{f}_{ij}(\mathbf{r} + \mathbf{c_i}, t) + \hat{f}_i(\mathbf{r} - \mathbf{c_i}, t) - 2\hat{f}_{ij}(\mathbf{r}, t)\right)\phi^2 \end{aligned} \tag{2.86}$$

Here $\phi = 1 - \frac{1}{\sqrt{m_i}}$ and $\hat{f}_{ij}$ denotes the discreet distribution function after collision or bounce back but before streaming. To achieve the correct boundary behavior a special streaming step was applied for voxels which are not fluid voxels, e.g. solid voxels.

Streaming from a soild voxel into the fluid:

$$f_{ij}(\mathbf{r} + \mathbf{c_i}\Delta t, t + \Delta t) = \hat{f}_{ij}^{solid}(\mathbf{r}, t) + \left(\hat{f}_{ij}(\mathbf{r} + \mathbf{c_i}, t) - \hat{f}_{ij}^{solid}(\mathbf{r}, t)\right)\phi \tag{2.87}$$

Streaming from the fluid into a solid voxel:

$$f_{ij}^{solid}(\mathbf{r} + \mathbf{c_i}\Delta t, t + \Delta t) = \hat{f}_{ij}(\mathbf{r}, t) + \left(\hat{f}_{ij}(\mathbf{r}, t) - \hat{f}_{ij}(\mathbf{r} - \mathbf{c_i}, t)\right)\phi \tag{2.88}$$

In the model validation benchmarks in chapter 7, we observed that both of the above equations are crucial to achieve the correct behavior at the boundary, especially to guarantee the conservation of mass and momentum.

2.4.6 *Boundary conditions*

2.4.6.1 *Noslip/Bounce Back Boundary Condition*

The simplest way to implement a noslip boundary condition (BC) is the bounce back boundary condition, which is easily achieved by introducing a new type of lattice node, the solid node. Instead of the collision step calculated for fluid nodes, solid nodes are updated according to the following scheme before the streaming step is executed:

$$f_i = f_{opp(i)} \tag{2.89}$$

The function $opp(i)$ returns the index which is opposite to the index $i \in \{0, 1, 2, ..., 26\}$ in the 3D discreet velocity space (see figure 2.2), effectively leading to a bounce back of the in streaming populations f_is along $c_{opp(i)} = -c_i$ and resulting into a no slip boundary condition.

2.4.6.2 *Periodic Boundary Conditions*

Periodic boundary conditions provide a way to mimic an infinite system by allowing fluid or information to seamlessly wrap around from one boundary face of the domain to the opposite boundary face. The idea behind periodic BC is to create a virtual replica of the domain which is periodically repeated along one or several directions in space. This means for the LB method that if one f_i streams beyond the domain face, it re–enters the domain through the opposite domain face, preserving the continuity of the system. Periodic BC therefore eliminate the need to model the behavior at the boundaries through an additional condition and simplify the simulation setup. Periodic BC are a reasonable choice when modeling a system which is actually embedded in a much larger system. Furthermore periodic BC conserve the total mass inside the domain.

2.4.6.3 *Density/Pressure Boundary Conditions*

Density boundary conditions have been implemented according to Zong, Li, and Wang [53]. Prescribing the density ρ_{in} at the domain boundary also fixes the phase and the pressure at the domain boundary for a multi–phase code. Below an example is given for an implementation of the density boundary condition in x–direction:

$$u = 1 - \frac{1}{\rho_{in}} \left(f_0 + f_2 + f_4 + f_9 + f_{11} + f_{13} + f_{18} + f_{20} + f_{22} + 2\left(f_3 + f_6 + f_7 + f_{12} + f_{15} + f_{16} + f_{21} + f_{24} + f_{25}\right) \right)$$

$v = 0$, $w = 0$.

$$N_y = \frac{f_2 + f_{11} + f_{20} - f_4 - f_{13} - f_{22}}{6} - \frac{\rho_{in}}{9} v$$

$$N_z = \frac{f_9 + f_{11} + f_{13} - f_{18} - f_{20} - f_{22}}{6} - \frac{\rho_{in}}{9} w$$

$$f_1 = f_3 + \frac{2 w_3 \rho_{in}}{c_s^2} u$$

$$f_5 = f_7 + \frac{2 w_7 \rho_{in}}{c_s^2} (u + v) - N_y$$

$$f_8 = f_6 + \frac{2 w_6 \rho_{in}}{c_s^2} (u - v) + N_y$$

$$f_{10} = f_{21} + \frac{2 w_{21} \rho_{in}}{c_s^2} (u + w) - N_z$$

$$f_{19} = f_{12} + \frac{2 w_{12} \rho_{in}}{c_s^2} (u - w) + N_z$$

$$f_{14} = f_{25} + \frac{2 w_{25} \rho_{in}}{c_s^2} (u + v + w) - N_y - N_z$$

$$f_{23} = f_{16} + \frac{2 w_{16} \rho_{in}}{c_s^2} (u + v - w) - N_y + N_z$$

$$f_{17} = f_{24} + \frac{2 w_{24} \rho_{in}}{c_s^2} (u - v + w) + N_y - N_z$$

$$f_{26} = f_{15} + \frac{2 w_{15} \rho_{in}}{c_s^2} (u - v - w) + N_y + N_z$$

2.4.6.4 *Evaporation Boundary Conditions*

Following the work from [39] we use the Hertz–Knudsen–Schrage equation 2.17 to calculate the evapoartion flux j_{evap}. The gas is treated as a two component gas mixture. One component is vapor ($j = v$) and the other component is dry air ($j = d$).

To ensure mass conservation the mass balance equation at the liquid–gas interface has to be fulfilled [39]:

$$\mathbf{j}_{v,in} + \mathbf{j}_{v,out} = j_{evap} \hat{\mathbf{n}} \tag{2.90}$$

$$\mathbf{j}_{v,in} = \sum_{i \in IN \wedge \mathbf{c}_i \cdot \hat{\mathbf{n}} > 0} f_{iv}\, \mathbf{c}_i, \qquad \mathbf{j}_{v,out} = \sum_{i \in IN \wedge \mathbf{c}_i \cdot \hat{\mathbf{n}} > 0} f_{opp(i)v}\, \mathbf{c}_{opp(i)} \tag{2.91}$$

It should be mentioned that the BC in equation 2.90 and 2.91 will lead to an injection of mass and momentum into the domain. Similar

to [39] we define the normal vector of the liquid–gas interface as follows:

$$\mathbf{n} = \sum_{i \in IN} \frac{1}{|\mathbf{c}_i|} \mathbf{c}_i \tag{2.92}$$

$\hat{\mathbf{n}} = \mathbf{n}/|\mathbf{n}|$ is the unit normal vector of the interface at a given interface voxel.

For the evaporation the function $s(\mathbf{x})$ is extended by an additional liquid node type and is defined as:

$$s(\mathbf{x}) = \begin{cases} 0 & \text{if gas node at } \mathbf{x} \\ 1 & \text{if solid node at } \mathbf{x} \\ 2 & \text{if liquid node at } \mathbf{x} \end{cases} \tag{2.93}$$

$s(\mathbf{x})$ is fixed in time and contains the domain information for all lattice nodes. The set IN which contains the indices of all incoming directions on the liquid–gas interface at position $\mathbf{x}_{inter}$ is defined by the following conditions [39]:

$$s(\mathbf{x}_{inter} + \mathbf{c}_i) = 0 \wedge s(\mathbf{x}_{inter}) = 2 \wedge s(\mathbf{x}_{inter} - \mathbf{c}_i) = 2 \tag{2.94}$$

Figure 2.3 shows an example for a liquid–gas interface based on the condition in equation 2.94.

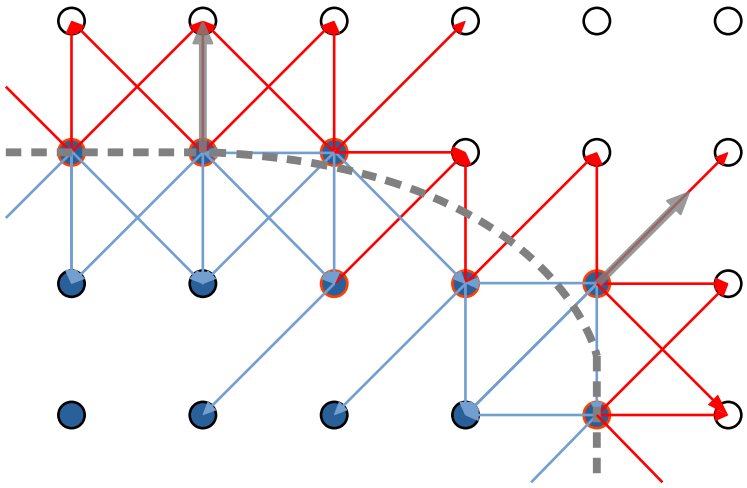

Figure 2.3: Liquid voxels in blue and fluid voxels in white, evaporation boundary voxels are marked with a circular orange border. Arrows in gray mark the unit normal vector, arrows in red show the incoming directions and arrows in light blue show the outgoing directions.

It is important to mention that for certain liquid distribution within the domain some $i \in IN$ can lead to $\mathbf{c}_i \cdot \hat{\mathbf{n}} \leq 0$, which would mean that an f_i is streaming into the interface and not outward as intended for an evaporation. This must be taken into account when constructing the evaporation BC.

A scalar product of $\hat{\mathbf{n}}$ and equation 2.90 yields:

$$\mathbf{j}_{v,in} \cdot \hat{\mathbf{n}} + \mathbf{j}_{v,out} \cdot \hat{\mathbf{n}} = j_{evap} \tag{2.95}$$

With $\mathbf{c}_{opp(i)} = -\mathbf{c}_i$ folows:

$$\sum_{i \in IN \wedge \mathbf{c}_i \cdot \hat{\mathbf{n}} > 0} (f_{iv} - f_{opp(i)v})\, \mathbf{c}_i \cdot \hat{\mathbf{n}} = j_{evap} \tag{2.96}$$

To find the in streaming f_is at the liquid–gas interface that satisfy the mass balance, Safi et al. [39] used an iterative procedure. As an initial value for the iterative process, Safi et al. [39] utilized the equilibrium distribution $f_{iv}^{init} = f_{iv}^{eq}(\rho_{v,init}, \mathbf{u}_{v,init}, T)$. The iteration stops if equation 2.90 is fulfilled with a prescribed accuracy.

This procedure has drawbacks, an iterative process can slow down the code, and the choice of the initial guess has an impact on the convergence speed, and for some geometries it may not converge at all for certain initial guesses. To cure these drawbacks we propose an alternative method to calculate the in streaming f_is based on j_{evap}:

$$f_{iv} = \begin{cases} f_{opp(i)v} + \frac{w_i}{w_{tot}} j_{evap} & \text{if } i \in IN \wedge \mathbf{c}_i \cdot \hat{\mathbf{n}} > 0 \\ f_{opp(i)v} & \text{else} \end{cases} \tag{2.97}$$

$$w_{tot} = \sum_{i \in IN \wedge \mathbf{c}_i \cdot \hat{\mathbf{n}} > 0} w_i\, \mathbf{c}_i \cdot \hat{\mathbf{n}} \tag{2.98}$$

This method is basically an extension of the bounce back boundary condition. When f_i is bouncing into a liquid voxel it gets inverted, just like for the normal bounce–back, but at the same time it gains mass and momentum according to equation 2.97 (see figure 2.4). It should be noted that this method also can be applied for condensation since in this case j_{evap} becomes negative and bouncing into a liquid voxel will reduce the mass and momentum of the species.

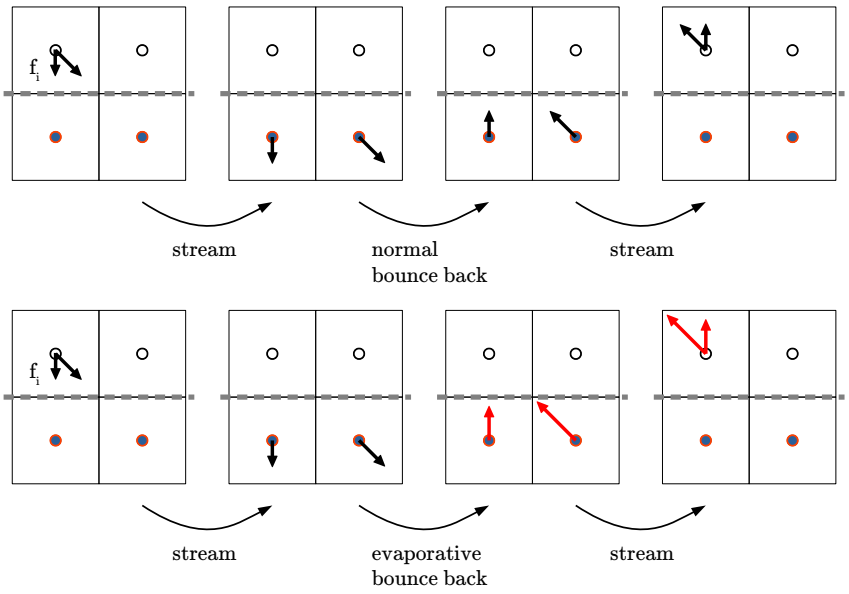

Figure 2.4: Example for a bounce back and an evaporative bounce back BC.

If the sum in equation 2.96 includes more then one summand, the solution for the f_{iv}s are not unique. One possible solution is given in equation 2.97. The w_is allow to redistribute the injected mass and momentum among the fluid voxels adjacent to the liquid voxel. We chose that w_i correspond to the weight from the equilibrium distribution given in equation 2.49. This reduces the mass and momentum injected into diagonal neighbour voxels and increases it for perpendicular neighbour voxels.

The definition of w_{tot} in equation 2.98 is crucial to ensure that the mass balance in equation 2.90 is recovered. When the gas above the liquid interface reaches saturation and j_{evap} becomes zero this method ensures that the liquid interfaces turns into a bounce–back BC ($f_{iv} = f_{opp(i)v}$). This guarantees also for complex boundaries consisting of solid and liquid voxels a stable and consistent schema.

2.4.6.5 *Outflow Boundary Condition for the Multi Component Case*

For a single phase multi component code a simple way to realise an outflow BC with a prescribed boundary density for each species ρ_{jb} is achieved by the following:

$$f_{ij}(x,y,z) = f_{ij}^{eq}(\rho_{jb}, u_x, u_y, u_z, T) \tag{2.99}$$

For an out flow at $x = 0$ holds $u_x(x = 0,y,z) = u_x(x = 1,y,z)$, $u_y(x = 0,y,z) = u_y(x = 1,y,z)$ and $u_z(x = 0,y,z) = u_z(x = 1,y,z)$.

2.4.7 *Implementation details*

The 3D LB simulations carried out in this work utilized an adapted high–performance computing code from Safi et al. [39] developed at the Paul Scherrer Institut in Switzerland. My contribution to the code was the extension of the model from single to multiphase flow, the implementation of periodic BC, density (pressure) BC and an improved version of the evaporation BC.

Because the LB method is explicit and the calculations are executed locally, efficient multithread parallelization within GPUs can be utilized. In particular the code utilizes a combined CUDA–MPI programming structure, allowing it to run concurrently on multiple Nvidia GPUs. For the investigated geometries, multiple GPUs had to be employed simultaneously since the required device (GPU) memory increases in a proportional manner alongside the overall voxel count within the domain. The full domain was subdivided along the x–axis into M separate slices and the LB calculations are carried out in parallel on M different GPUs assigned to different HPC nodes (see figure 2.5).

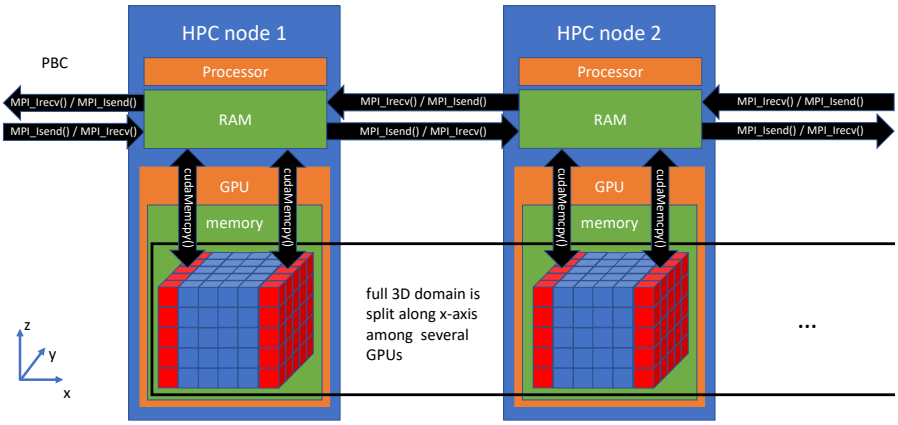

Figure 2.5: Parallel computing architecture on a HPC cluster.

Within the D3Q27 LB method, the time evolution of 27 discreet distribution functions f_i need to be computed for each lattice node at each time step, involving the collision step (right side of equation 2.39) and the streaming to the neighbouring nodes. For each time step, a sequence of functions is executed on the processor of each HPC node, shown in the flowchart diagram in figure 2.6. CUDA kernels are special functions that are executed on a GPU for a subsection of the domain. Every kernel call involves calculations which are executed concurrently for every voxel in the full domain within the M GPUs.

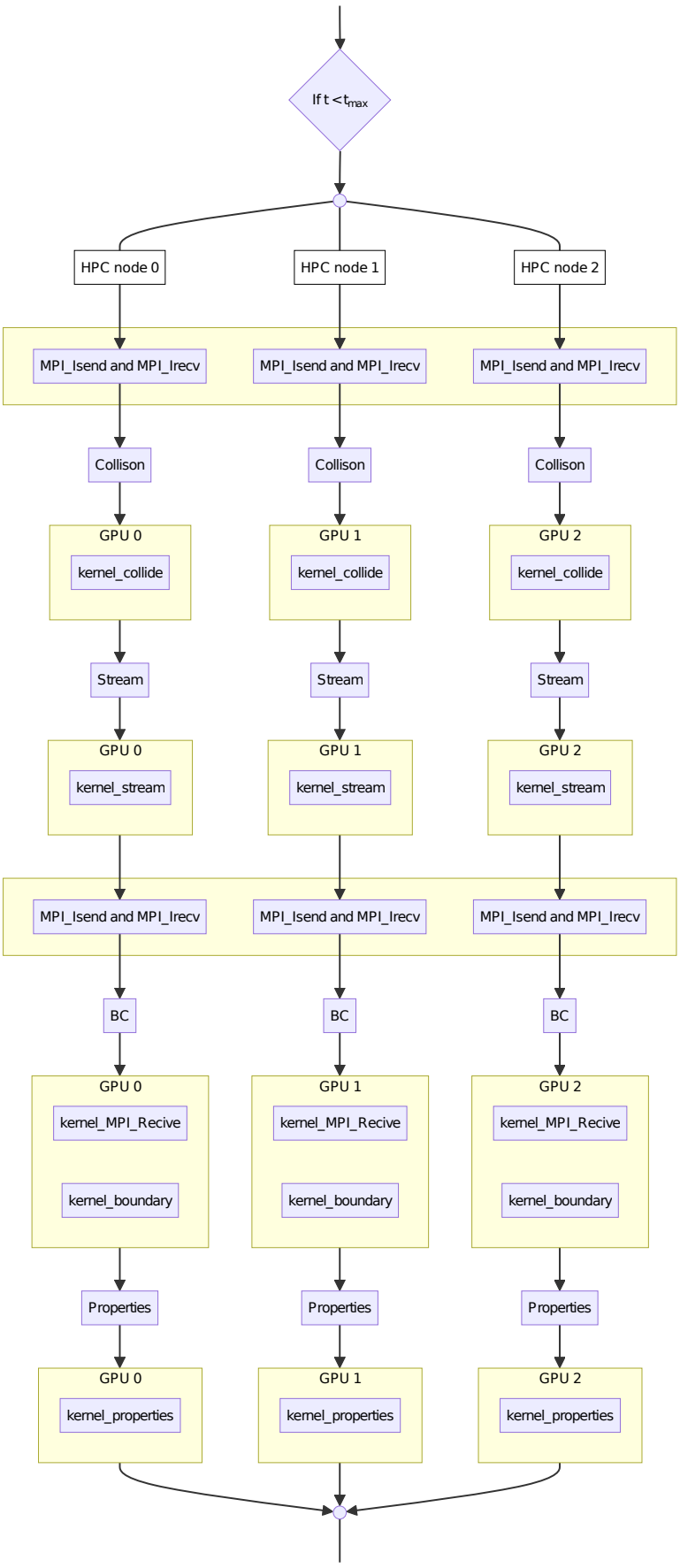

Figure 2.6: CUDA–MPI programming structure of the LB multiphase code.

For the multiphase case, the collision step involves a force calculation that includes the density values of the adjacent lattice points, so density values of another HPC node are required at the subdomain faces (red lattice points in figure 2.5). These density values are transferred via the MPI protocol using the functions MPI_Isend() and MPI_Irecv(). To perform the streaming from one subdomain face to is adjacent subdomain face, the MPI protocol is used again. The MPI_receive kernel completes the streaming after the f_is have been exchanged with the functions MPI_Isend() and MPI_Irecv(). The MPI send and receive procedure always involves copying data from the HPC node RAM to the GPU memory and vice versa. If PBC are enabled, the first HPC node has to exchange data with the last HPC node. Safi et al. [39] found in previous benchmarks that optimal computational efficiency is guaranteed if the GPU device memory use of each GPU was maximized. In case of periodic boundary conditions, is was important to use non blocking data transfer between the HPC nodes via the MPI_Isend() and MPI_Irecv() functions to ensure the best computational performance. The boundary kernel in figure 2.6 includes the implementation of BC at the domain boundary, like e.g. density (pressure) boundary conditions, if PBC are disabled. In the properties kernel the density and velocity on each lattice point are calculated according to equation 2.41 and 2.42 respectively.

3

PORE–LEVEL MULTIPHASE SIMULATIONS OF REALISTIC DISTILLATION MEMBRANES FOR WATER DESALINATION

First author publication in the peer reviewed journal MDPI membranes. URL to the paper: https://www.mdpi.com/2077-0375/12/11/1112. A detailed list of the author contribution can be found at the end of the paper.

In the study presented in this publication, we validate the 3D LB Shan–Chen multiphase model and demonstrate its ability to correctly simulate multiphase flow in realistic porous membranes typically used in MD. In addition to some standard validation benchmarks, we also compare the liquid entry pressure, an important membrane property, calculated with the multiphase model with previous experiments using similar membranes and found good agreement.

With such a powerful 3D multiphase model available, we simulated a pressurized liquid film on top of the porous membrane structure at the pressures typically expected for AGMD and found that a flat liquid–gas interface is a reasonable assumption for an untreated membrane. The liquid–gas interface is therefore limited by the porosity of the membrane material. We also studied the air–water interface in partially saturated membranes and found a correlation between droplet size (and location) and membrane porosity. Therefore water droplets tend to agglomerate in membrane areas of high porosity.

In this work we utilized detailed 3D membrane geometries typically used in MD from Cramer et al. [10]. Each geometry contains up to half a billion voxels at a resolution of 39 nm, obtained through ptychographic X–ray computed tomography.

membranes

MDPI

Article

Pore-Level Multiphase Simulations of Realistic Distillation Membranes for Water Desalination

Tobias Jäger [1,*], Athanasios Mokos [2], Nikolaos I. Prasianakis [2] and Stephan Leyer [1]

[1] Department of Engineering, Faculty of Science, Technology and Medicine , University of Luxembourg, L-1359 Luxembourg, Luxembourg; stephan.leyer@uni.lu
[2] Transport Mechanisms Group, Laboratory for Waste Management, Paul Scherrer Institute, 5232 Villigen PSI, Switzerland; athanasios.mokos@psi.ch (A.M.), nikolaos.prasianakis@psi.ch (N.I.P.)
* Correspondence: tobias.jaeger@uni.lu; Tel.: +352-466-644-9621

Abstract: Membrane distillation (MD) is a thermally driven separation process that is operated below boiling point. Since the performance of MD modules is still comparatively low, current research aims to improve the understanding of the membrane structure and its underlying mechanisms at the pore level. Based on existing realistic 3D membrane geometries (up to 0.5 billion voxels with 39 nm resolution) obtained from ptychographic X-ray computed tomography, the D3Q27 lattice Boltzmann (LB) method was used to investigate the interaction of the liquid and gaseous phase with the porous membrane material. In particular, the Shan and Chen multi-phase model was used to simulate multi-phase flow at the pore level. We investigated the liquid entry pressure of different membrane samples and analysed the influence of different micropillar structures on the Wenzel and Cassie–Baxter state of water droplets on rough hydrophobic surfaces. Moreover, we calculated the liquid entry pressure required for entering the membrane pores and extracted realistic water contact surfaces for different membrane samples. The influence of the micropillars and flow on the water-membrane contact surface was investigated. Finally, we determined the air–water interface within a partially saturated membrane, finding that the droplet size and distribution correlated with the porosity of the membrane.

Keywords: membrane distillation; water treatment; lattice Boltzmann method; multi-phase flow

Citation: Jäger, T.; Mokos, A.; Prasianakis, N.I.; Leyer, S. Pore-Level Multiphase Simulations of Realistic Distillation Membranes for Water Desalination. *Membranes* **2022**, *1*, 0. https://doi.org/

Academic Editor: Chii-Dong Ho

Received: 2 September 2022
Accepted: 22 October 2022
Published:

1. Introduction

Freshwater scarcity is already a severe problem for many countries in the world and will deteriorate in the future due to the climate crisis [1]. However, many arid areas have both access to seawater and high solar irradiance. Therefore seawater desalination is a promising approach for these countries. The most used seawater desalination technologies rely on thermal distillation and reverse osmosis. Common thermal separation processes include multi-effect distillation, a low-pressure steam process, and multi-stage flash evaporators [2]. Nevertheless, these technologies require a lot of energy and a sufficient power supply infrastructure [3].

Membrane distillation (MD) is a thermally driven separation process that is operated below the boiling point of water and is capable of providing significant contributions to the problem of water scarcity in the world [4]. In MD, evaporation is used to extract pure water from saline or brackish water. Compared to the aforementioned technologies, MD has the advantage of small investment and low operating costs as it can be driven by non-concentrated solar energy [5] or waste heat [4]. However, the overall efficiency and output production rate of MD modules are still too small to be competitive [6,7].

The key to improving the design, performance, and efficiency of MD modules is to better understand the underlying mechanisms that govern the separation processes. Several different MD designs have been developed. A very promising design for seawater distillation is the air gap membrane distillation (AGMD) module. In this approach, the hot

feed solution is in direct contact with a hydrophobic membrane, but in contrast to direct contact membrane distillation, an air layer separates the membrane and the condenser (See Figure 1). The water vapour diffuses through the membrane and the air gap to condense on a cold surface. The hydrophobicity of the membrane prevents the saltwater from ingressing within the membrane. Salt contaminants cannot be transported via the vapour phase and only water molecules in vapour form can cross the membrane [8].

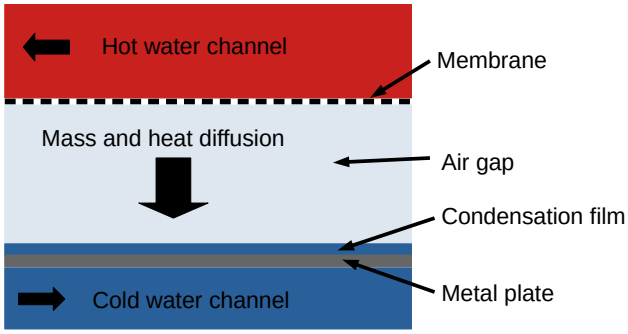

Figure 1. Sketch of an AGMD module.

The main benefit of AGMD is the thermal insulation properties of the air gap, which reduce heat loss. On the downside, the air gap represents an additional mass transport pathway, which has an effect on the membrane throughput [4]. The salt concentration at the evaporation interface is also increased due to water evaporation, which can lead to the precipitation of salt and other pollutants and the blockage of the membrane pores. Specific membrane structures such as micropillars and increased hydrophobicities can reduce scaling and prolong the life cycle of a membrane [9,10].

The phase change and mass transport mechanisms take place within the membrane's microporous structure. An important dimensionless number for characterising the flow regime is the Knudsen number ($\mathrm{Kn} = \frac{\lambda}{L}$), where λ is the mean free path length of the particles and L is the characteristic length scale of the flow [11]. The Knudsen number can be used to define four flow regimes: the continuum ($\mathrm{Kn} < 0.01$), slip flow ($0.01 < \mathrm{Kn} < 0.1$), transitional flow ($0.1 < \mathrm{Kn} < 10$), and free molecular flow ($\mathrm{Kn} > 10$). For MD applications, L represents the pore diameter of the membrane (200 nm–450 nm), and with respect to the vapour phase, this results in a Knudsen number of $\mathrm{Kn} \approx 1$ [12].

Since assessing the flow on the microscopic level through experimental methods is complex, little is known about the interaction of liquid, gas, and hydrophobic membrane material at the pore level. To increase the efficiency of MD modules a better understanding of the underlying mechanisms, such as evaporation at the pore level, would be beneficial. For this reason, detailed numerical modeling of the mechanisms occurring in MD is required.

Evaporation as a non-equilibrium process is a complex phenomenon with temperature jumps observed at the liquid–gas interface where evaporation occurs. Different theories, such as the Hertz–Knudsen equation and statistical rat theory (SRT), were developed to calculate the evaporation flux [13,14].

The size of the evaporation flux depends among other parameters on the vapour pressure above the liquid–gas interface, the surface area of the liquid–gas interface, and the salt content in the water. The larger surface areas of the liquid–vapour interface will lead to higher evaporation fluxes. The basis for the evaporation models mentioned above is a static liquid–gas interface, which needs to be determined before the model is applied.

The fluid dynamics of this case can be expressed either through a continuum-based approach or a particle-based approach. For the continuum approach, macroscopic quantities such as density and velocity are used to describe the flow, whereas the particle approach takes into account the individual particles (atoms, molecules) and their interactions. For domains, orders of magnitude larger than the mean free path of the particle continuum-

based approaches, such as the Navier–Stokes equation and classical computational fluid dynamics (CFD) solvers, provide a viable description of the flow. For 3D micro- and nano-scale complex microstructures, as is the case for the considered membranes, the lattice Boltzmann (LB) framework is a promising approach [15,16].

The LB method describes the flow on a mesoscopic level up to the continuum level and allows for the simulation of the flow in the slip flow regime (Kn < 0.1). The LB method is based on kinetic gas theory and the time evolution of the one-body distribution function, $f(\vec{x}, \vec{v}, t)$ which is a probability density function. $f(\vec{x}, \vec{v}, t)\,\mathrm{d}\vec{x}\,\mathrm{d}\vec{v}$ is the mean number of particles in a phase-space volume $\mathrm{d}\vec{x}\,\mathrm{d}\vec{v}$ at position $\vec{x}$ with velocity $\vec{v}$ at time t. For the LB method, the phase space is discretized, ending up in a domain with discrete cubic cells and discrete velocities.

When membrane distillation modules are modeled numerically, the membrane and the transport of the water vapour through the membrane are typically modeled using the dusty gas model and a flat liquid–membrane interface. For the dusty gas model, only membrane properties, such as porosity and tortuosity, as well as the viscosity of the gas mixture, are required as input for the calculation of the macroscopic flux through the membrane. A microscopic description of the membrane geometry at the pore level is not taken into account within the scope of the dusty gas model [8,17].

To obtain a detailed picture of the liquid–membrane interface, we use high-resolution membrane geometries, which are resolved at the pore level [12], and a multi-phase LB method. In order to validate the model, we simulate typical benchmarks such as the contact angle and Laplace law benchmark. To ensure the correct interaction with the rough membrane material, we validate the influence of micropillar structures on the apparent contact angle in both the Cassie–Baxter and the Wenzel states [18,19] and identify the liquid entry pressure (LEP) needed for the water to move into the pores of the hydrophobic membrane for both a cylindrical and realistic geometry. The LEPs for the realistic membrane samples are compared to the values from the manufacturers. Finally, we use the validated model to determine realistic water–membrane contact surfaces and investigate the droplet distribution within 3D membrane geometries.

2. Materials and Methods

2.1. Membrane Geometry

Experimentally determined [12] membrane geometries were used. A summery of the membrane samples can be seen in Table 1. Cramer et al. [12] used ptychographic X-ray-computed tomography to map the 3D membrane structure of four commercially used membranes at an unprecedented resolution. Pictures of the full membrane geometry are available in [12]. The experiments were conducted at the cSAXS beamline of the Swiss Light Source, PSI, Switzerland. The membrane material was PTFE and the manufacturer values of the porosity were 85% for samples 1, 3, and 4 and 80% for sample 2. The X-ray device used photons with an energy of 6.2 keV achieving a spatial cubic voxel size of $\Delta^{SI}x = 0.03899\,\mu\mathrm{m}$ and a total voxel number of about 0.5 billion voxels per sample. The electron density difference between the membrane material and epoxy (pore space in the membrane) can be used to create a binary (membrane and void) 3D image of the membrane by applying a threshold. For samples 2, 3, and 4, the porosity value based on the ptychographic X-ray-computed tomography matched the manufacturer values [12]. Moreover, Cramer et al. [12] calculated membrane characteristics such as tortuosity and permeability based on single-phase LB simulations with a pressure gradient. Note that samples 1 and 4 originated from different parts of the same membrane.

Table 1. 3D membrane geometries obtained by Cramer et al. [12].

Sample	Membrane	Manufacturer	Pore Diameter [µm]	Sample Dimensions ($x \times y \times z$) [µm^3]	[Voxels]
1	FGLP14250	Merck Millipore	0.2	59.85 ×22.42 × 22.42	1535 × 575 × 575
2	Gore [a]	Gore	0.22	57.70 × 15.60 × 15.60	1480 × 400 × 400
3	FHLP14250	Merck Millipore	0.45	62.42 × 21.44 × 21.44	1601 × 550 × 550
4	FGLP14250	Merck Millipore	0.2	25.34 × 37.04 × 37.04	650 × 950 × 950

2.2. Numerical Method

In this paper, the D3Q27 LB method (see Figure 2) was applied with 27 discrete velocities ($\vec{c}_i$, $i = 0..26$) in a 3D space [20].

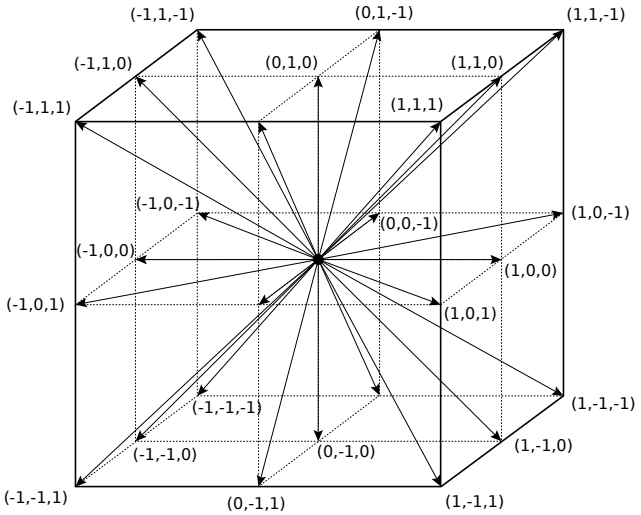

Figure 2. D3Q27 lattice with 27 discrete velocities $\vec{c}_i$.

The evolution of the discrete density distribution function can be written as:

$$f_i(\vec{x} + \vec{c}_i \Delta t, t + \Delta t) - f_i(\vec{x}, t) = -\frac{1}{\tau}\left[f_i(\vec{x}, t) - f_i^{eq}(\rho, \vec{v}, \vec{x}, t)\right] \quad (1)$$

The term on the right is the Bhatnagar–Gross–Krook approximation of the collision operator, reflecting the inter-particle collisions in the fluid [21]. The relaxation time τ is linked to the viscosity of the fluid. In the LB method, the discrete one-body distribution function f_i is relaxed towards a local equilibrium f_i^{eq}. The term on the left represents the propagation of the density distribution function. In this step, the f_is are streamed to their respective neighbouring cells.

The LB method is usually not simulated with SI units but as a similarity problem. For our LB simulation, we used the common LB unit convention: the time step (ts) was set to one, the lattice spacing (Δx) was set to one lattice unit (lu), and the mass of one fluid particle (m) was set to one mass unit (mu). This way, the LB unit convention gave $\Delta t = 1$ ts, $\Delta x = 1$ lu, $m = 1$ mu. Therefore, the speed of sound equalled $c_s = \frac{1}{\sqrt{3}} \frac{\text{lu}}{\text{ts}}$ for the D3Q27 lattice. As is typically done for such multi-phase LB simulations, e.g., [22], for increased stability and faster numerical convergence we chose $\tau = 1$ ts for our simulations. This corresponds to a kinematic viscosity of $1/6\,\text{lu}^2/\text{ts}$ ($\nu = c_s^2(\tau - 0.5)\Delta t$). In SI units, this corresponds to $\Delta t^{SI} = 0.087$ ms and $\Delta^{SI} x = 0.03899$ µm for the membrane geometries mentioned above.

In order to initialize the LB simulation so that it corresponded to the real physical problem, the relevant governing dimensionless numbers must be equal. The problems studied here are governed by the Laplace and Bond dimensionless numbers. The Laplace number is typical for free-surface fluid dynamic flows (multi-phase flow). It relates the

momentum and surface tension forces to viscous forces (La $= \frac{\gamma \rho_l L}{(\eta_l)^2}$) [23] and is used to map the surface tension LB units to the SI units. γ represents the surface tension, ρ_l is the density of the liquid, η_l is the dynamic viscosity of the liquid and L is the characteristic length.

$$\gamma^{SI} = \gamma \frac{\rho_l \, (\eta_l^{SI})^2}{\Delta x^{SI} \, \rho_l^{SI} \, (\eta_l)^2} \tag{2}$$

The Bond number (Bo $= \frac{\Delta \rho g L^2}{\gamma}$) describes the ratio of gravitational to capillary forces [23]. For the membranes assessed, the Bond number is Bo ≈ 0.0001, which means that gravitation is negligible. To convert the time step to SI units, the capillary number can be used $\Delta t^{SI} = \frac{\mu \Delta x^{SI} \gamma}{\gamma^{SI} \mu_{SI}}$. This results in $\Delta t^{SI} = 0.23 \cdot 10^{-9}$ s for the assessed membranes. To convert the pressure from LB units to SI units, the following expression was used: $p^{SI} = p \cdot \frac{\gamma^{SI}}{\gamma \cdot \Delta x^{SI}}$.

The LB method is designed to reproduce the Navier–Stokes equation in the hydrodynamic limit [20]. Macroscopic quantities such as density and velocity can be calculated by summing up the discrete populations f_i and discrete velocities c_i [20].

$$\rho = \sum_{i=0}^{26} f_i \tag{3}$$

$$\vec{v} = \frac{1}{\rho} \sum_{i=0}^{26} f_i \vec{c}_i \tag{4}$$

In this case, the guided equilibrium (GE) model proposed in [20,24] was used. The GE function was found by minimizing the entropy function under four constraints. These constraints ensured the conservation of mass, momentum, and energy, as well as imposed an additional constraint on the pressure tensor. This fourth constraint was a "necessary (but not sufficient) condition in order to recover the Navier-Stokes equations" [20]. The results can be written in the following form:

$$f_i^{eq}(\rho, \vec{v}) = \rho \prod_{\alpha = x,y,z} \frac{1 - 2c_{i\alpha}^2}{2c_\alpha^2} \left(c_{i\alpha}^2 - 1 + c_{i\alpha} v_\alpha + v_\alpha^2 + T \right) \tag{5}$$

The Shan–Chen multi-phase model was chosen [22,25,26]. The interaction between fluid particles was achieved by including the following force:

$$\vec{F} = -G \psi(\vec{x}, t) \sum_{i=0}^{26} w_i \psi(\vec{x} + \vec{c}_i \Delta t, t) \vec{c}_i \tag{6}$$

This leads to the non-ideal equation of state shown in Equation (7). The function $\psi(\rho)$ describes the interaction potential and depends on the density, whereas G describes the interaction strength between the fluid particles and allows the surface tension to be adjusted. According to [26,27], the following form of ψ was chosen: $\psi(\rho) = \psi_0 \exp(-\frac{\rho_0}{\rho})$, $\psi_0 = 4$, $\rho_0 = 200$, and $RT = 1/3$. This results in a phase separation below the critical value $G_{crit} = -92.4$. In this work, two different values were used: (a) $G = -120.0$, which yields a liquid density of $\rho_l = 524.4\,\mathrm{mu\,lu^{-3}}$ and a gas density of $\rho_g = 85.7\,\mathrm{mu\,lu^{-3}}$ in LB units for a flat liquid–gas interface [27], and (b) $G = -180.0$, leading to a liquid density of $\rho_l = 1027.81\,\mathrm{mu\,lu^{-3}}$ and a gas density of $\rho_g = 52.82\,\mathrm{mu\,lu^{-3}}$ in LB units for a flat liquid–gas interface. $G = -120.0$ is a typical value found in the literature and for $G = -180.0$, the above-mentioned membrane geometries result in the desired surface

tension of $\gamma^{SI} = 0.073\,\mathrm{N/m}$ (see Table 2 and Equation (2)). This corresponds to the surface tension of pure water at 16.5 °C.

$$p = \rho RT + \frac{GRT}{2}(\psi(\rho))^2 \tag{7}$$

We note that for the results presented in this paper, which are relevant to the shape of the liquid phase within the porous medium, the capillary forces are dominant rather than the density ratio between the liquid and gas phases. For simulations where the liquid phase's dynamic motion and interaction with the gas phase are of central importance, the model can be adjusted accordingly to capture the relevant physics. For the interaction between the fluid and solid, the following force is introduced, with the function $s(\vec{x})$ giving 1 for solid nodes and 0 for fluid nodes [22,27].

$$\vec{F}_{ads} = -G_{ads}\psi(\vec{x},t)\sum_{i=0}^{26} w_i s(\vec{x}+\vec{c}_i\Delta t,t)\vec{c}_i \tag{8}$$

The parameter G_{ads} correlates linearly with the contact angle for a given G value, as shown in the contact angle benchmark in Section 3.2. G_{ads} allows tuning the contact angle of a liquid droplet on the flat solid phase.

Additionally, a non-slip (bounce-back) boundary condition was employed for the fluid–solid interaction. The membrane samples in Table 1 only represent a small cutout of a membrane sheet typically used in MD. To mimic a much larger membrane sheet, periodic boundary conditions (PBC) were employed at the border of the domain. If not stated otherwise, PBC were used in all directions, x, y, and z, for our LB simulations. We also implemented density (pressure) boundary conditions for the LEP. Similar to [22], we used Zou and He [28] boundary conditions adapted for the D3Q27 lattice [29]. The total force is given by:

$$\vec{F}_{tot} = \vec{F} + \vec{F}_{ads} + \vec{F}_{exe} \tag{9}$$

$\vec{F}_{exe}$ represents an external force such as gravity or a pressure gradient. To incorporate the force in the LB method, Shan and Chen [25,26] modified Equation (4):

$$\vec{v} = \frac{1}{\rho}\sum_{i=0}^{26} f_i\vec{c}_i + \frac{\tau\vec{F}_{tot}}{\rho} \tag{10}$$

If not stated otherwise, the convergence criterion in Equation (11) was $1\cdot10^{-6}$ or better for the simulation.

$$\mathrm{mean}_{x,y,z}\left(\frac{|\rho^i(x,y,z)-\rho^{i-1}(x,y,z)|}{\rho^{i-1}(x,y,z)}\right) \tag{11}$$

Table 2. Summary of membrane and fluid properties.

	LB Units	SI Units	Remark
ρ_l	1028	998.861 $\frac{\mathrm{kg}}{\mathrm{m}^3}$	pure water, 1 bar, 16.5 °C
ρ_g	53	1.204 $\frac{\mathrm{kg}}{\mathrm{m}^3}$	1 bar, 16.5 °C
$\Delta\rho$	975	997.657 $\frac{\mathrm{kg}}{\mathrm{m}^3}$	
ρ_l/ρ_g	19.4	829.619	
μ_l	171.33	$1.094\cdot10^{-3}$ Pa·s	1 bar, 16.5 °C
μ_g	8.83	$1.81\cdot10^{-5}$ Pa·s	1 bar, 16.5 °C
μ_l/μ_g	19	60	
Δx	1	$0.039\cdot10^{-6}$ m	
Δt	1	$0.23\cdot10^{-9}$ s	
c	1	168.5 m/s	
La	24424	24424	1 bar, 16.5 °C
γ	68	0.073 N/m	pure water, 1 bar, 16.5 °C
Bo	$1\cdot10^{-4}$	$1\cdot10^{-4}$	

For the simulations, a high-performance computing code was adapted [30]. The code uses a hybrid CUDA-MPI programming layout, which enables it to be executed on several Nvidia GPUs in parallel. In the D3Q27 LB method, the evolution of a 27-distribution function has to be calculated at each lattice node. This includes three major steps: collision, streaming, and force calculation. Since the method is explicit and all calculations are local, the multithread parallelization within the GPU can be employed efficiently. For the geometries examined, several GPUs in parallel were used, as the required amount of device memory scaled linearly with the total number of voxels in the domain. During the streaming step and the force calculation, data were exchanged between neighbouring lattice nodes and thus between different computing nodes; therefore, the data transfer between different GPUs was realized with OpenMPI.

3. Results and Discussion

3.1. Surface Tension—Young–Laplace Benchmark

A typical benchmark for a multi-phase model is the verification of the Young–Laplace equation ($\Delta p = \gamma \cdot \frac{2}{r}$), which relates the radius r of a bubble to the pressure difference Δp between the liquid and gaseous phases. Figure 3 shows the results of the benchmark, which are in good agreement with the theory. This benchmark also allows for the determination of the surface tension of the gas–liquid interface. For the aforementioned model, we found $\gamma = 14.0409\,\mathrm{mu} \cdot \mathrm{ts}^{-2}$ (in LB units) for $G = -120.0$ and $\gamma = 68.45\,\mathrm{mu} \cdot \mathrm{ts}^{-2}$ (in LB units) for $G = -180.0$.

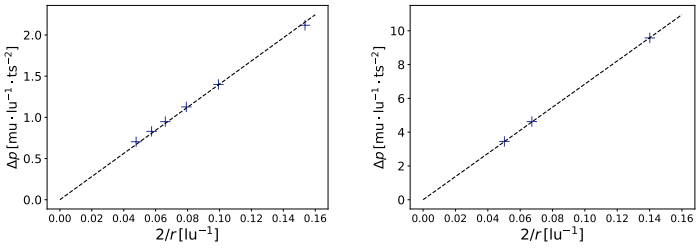

(**a**) (**b**)

Figure 3. Laplace law benchmark ($\Delta p = \gamma \cdot \frac{2}{r}$). In (**a**), $G = -120.0$, $R^2 = 0.9972$, $\gamma = 14.0409\,\mathrm{mu} \cdot \mathrm{ts}^{-2}$, where R^2 is the coefficient of determination. In (**b**), $G = -180.0$, $R^2 = 0.999960$, $\gamma = 68.45\,\mathrm{mu} \cdot \mathrm{ts}^{-2}$. Simulations were performed on a $100 \times 100 \times 100$ domain.

3.2. Wettability—Contact Angle Benchmark

An important property for a multi-phase flow in contact with a solid is the wettability of the surface, which is directly related to the contact angle α of a droplet on a flat surface. The contact angle describes the degree of the hydrophobic/hydrophilic properties of the surface and is dependent not only on the chemical composition of the solid material but also on the solid surface characteristics. The contact angle can be set by adjusting the adsorption coefficient G_{ads}. In the simulations, we initially placed a cubic liquid droplet on a flat surface and let it equilibrate until the simulation reached a static state (see Figure 4).

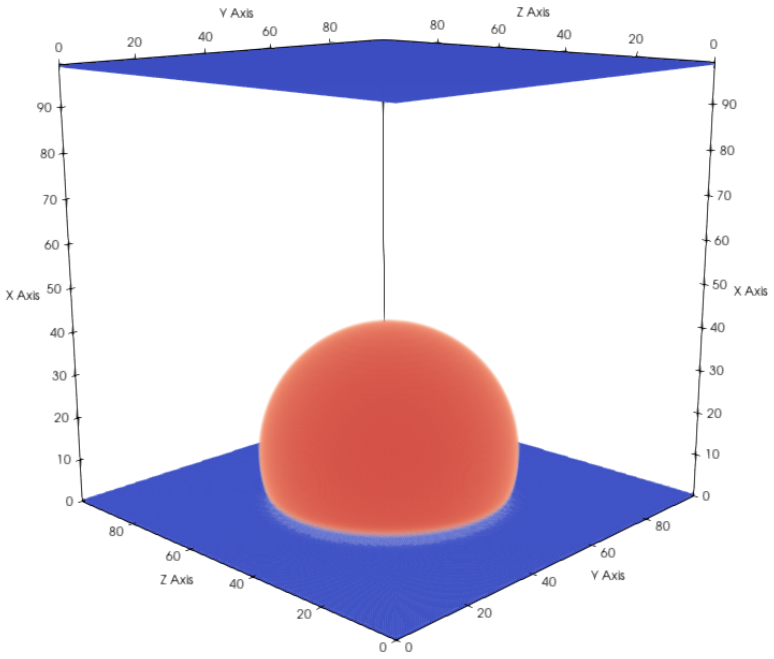

Figure 4. Droplet on a flat hydrophobic surface with a total domain size of $100 \times 100 \times 100$ voxels. Gaseous phase is not shown for better visibility. Contact angle changes depending on the hydrophobicity, which can be controlled with G_{ads} and G. $G_{ads} = -157.16$ and $G = -120.0$ result in a contact angle of 110.6°.

To determine the contact angle from the calculation results, we first extracted the points in the vicinity of the liquid–gas interface using the condition $\frac{\rho(x,y,z)-\rho_c}{\rho_c} < 0.01$ and fitted a sphere to these points. Finally, the expression $\cos\alpha = -\frac{x_c-b}{r}$ was used to calculate the contact angle, with x_c being the center of the sphere, r the radius of the sphere, and b the x position of the surface. The numerically measured linear dependency of α on G_{ads} is in agreement with the results of Peng et al. [22]. We also observed that the contact angle was independent of the droplet size (see Figure 5).

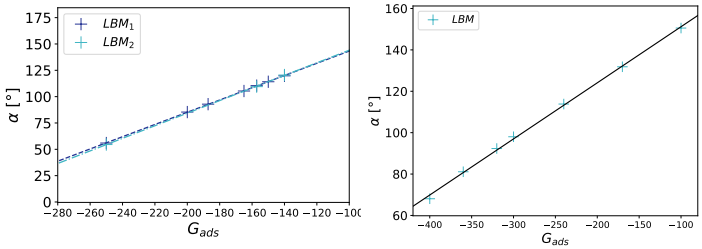

(**a**) (**b**)

Figure 5. Contact angle benchmark on a flat surface. The contact angle α is plotted against the strength of the fluid–solid interaction G_{ads}. In (**a**), $G = -120.0$, LBM_1, and LBM_2 correspond to the different droplet sizes in the LB simulation ($V_2 \approx 15625\,\mathrm{lu}^3$, $V_1 \approx 91125\,\mathrm{lu}^3$). For a linear fit $\alpha = m \cdot G_{ads} + b$, we obtain for the two droplet sizes $R_1^2 = 0.999875$, $m_1 = 0.5808$, $b_1 = 201.36$, $R_2^2 = 0.999882$, $m_2 = 0.5973$, $b_2 = 203.78$, where R_i^2 is the coefficient of determination. In (**b**), $G = -180.0$. Simulations were performed on a $100 \times 100 \times 100$ domain.

3.3. Cassie–Baxter and Wenzel States

It is well known that for a droplet on a surface, the (apparent) contact angle also depends on the surface structure. One can distinguish between Cassie–Baxter (CB) and Wenzel states [19,31]. For the CB state, gas is trapped in the gaps created by the surface roughness, with the result that the liquid droplet remains at a higher level and does not

penetrate the rough surface. For the Wenzel state, no gas is trapped at all and the liquid is in direct contact with the rough solid phase. It is therefore important to identify the state of the membrane in order to determine the correct contact angle. This step also serves as an additional benchmark to ensure the correct behavior on rough surfaces such as the membrane material studied later in this work.

Cassie and Baxter [19] developed an expression (Equation (12)) that relates the contact angle on a flat surface (α) to the apparent contact angle (α_{app}) on a rough surface of the same material for a droplet in the CB state. The parameter f_{SL} determines the fraction of the bottom surface of the liquid droplet in contact with the solid. Based on the micropillar structure, one can calculate $f_{SL} = \frac{A_{top}}{P^2}$, where A_{top} is the flat top surface area of a pillar and P is the pitch between pillars (periodicity).

$$\cos \alpha_{app}^{theor} = f_{SL}(\cos \alpha + 1) - 1 \tag{12}$$

Wenzel [31] developed a model describing a droplet in the Wenzel state. The apparent contact angle is computed through

$$\cos \alpha_{app}^{theor} = R_f \cos \alpha \tag{13}$$

where $R_f = 1 + \frac{A_l}{P^2}$ relates the total surface area of the roughness to its projection on a flat plane and A_l is the lateral surface of the pillar. Contact angles in the CB state are measured with respect to the plane above the roughness, whereas contact angles in the Wenzel state are measured with respect to the plane on the bottom of the roughness.

In this paper, we first analysed the dependence of the droplet state on the pillar structure (pillar distance) and the initial condition and compared the simulation results to the experiments performed by Jung and Bhushan [10] (Figures 6–8). Similar to the 3D LB simulations performed by Xiong and Cheng [32], who also used a Shan–Chen-like model, we compared the apparent contact angle of water droplets on a rough micropillar structure to the theoretical predictions from the CB and Wenzel equations (12) and (13).

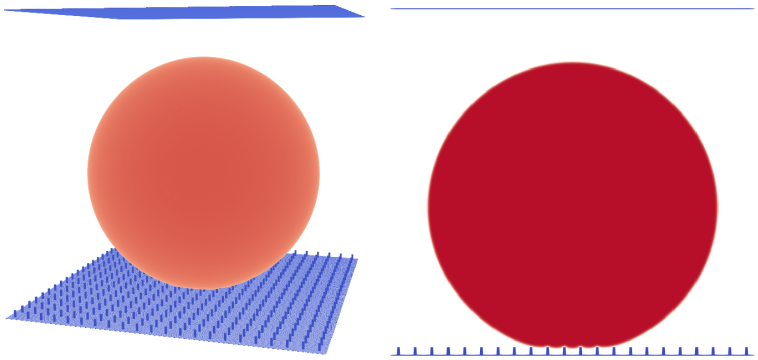

Figure 6. Micro pillar structure with $P = 17\,\text{lu}$, pillar height $H = 8\,\text{lu}$, and $A_{top} = 3{\times}3\,\text{lu}^2$. A droplet in the Cassie–Baxter state. Liquid phase is shown in red and micropillar structure is shown in blue.

We then performed a series of simulations with different starting conditions and different pillar distances P. The CB state is, in contrast to the Wenzel state, a meta-stable equilibrium state, where small perturbations can lead to a switch from the CB to the Wenzel state [18]. This is something we observed in our simulations, where different initial states led to different equilibrium states for certain geometries. Two initial states were tested. The first was a "cubic droplet" and the second was a spherical droplet, both above the rough surface. Similar to the work of Peng et al. [22], we used Equation (14) to initialise the spherical droplet. For $P = 12\,\text{lu}$, both initial states led to a CB state. For $P = 17\,\text{lu}$, only the spherical droplet led to a CB state and the cubical droplet led to a Wenzel state.

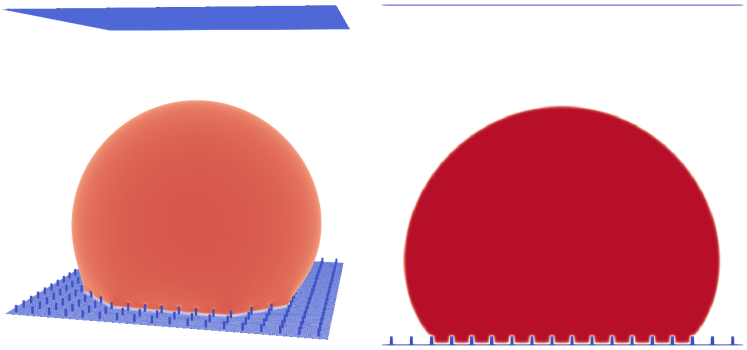

Figure 7. Micro pillar structure with $P = 20\,\text{lu}$, pillar height $H = 8\,\text{lu}$, and $A_{top} = 3{\times}3\,\text{lu}^2$. A droplet in the Wenzel state. Liquid phase is shown in red and micropillar structure is shown in blue.

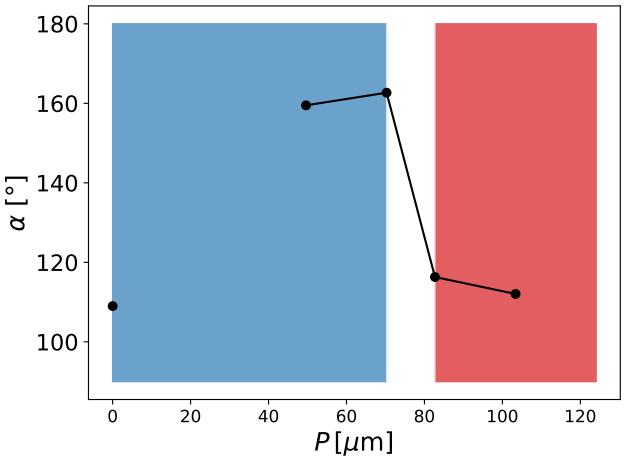

Figure 8. Contact angle α in dependence of the pitch between pillars (P). For the blue area, the droplet is in the Cassie–Baxter state and for the red area, the droplet is in the Wenzel state; $1\,\text{lu} \equiv 4.135\,\mu\text{m}$, droplet volume is $1\,\mu\text{L}$, $H = 33\,\mu\text{m}$, and $A_{top} = 153.88\,\mu\text{m}^2$.

The simulation results in Figure 8 were initialised with a spherical droplet. At about $P = 70\,\mu\text{m}$, we observed a transition from the CB to the Wenzel state. The geometries shown in Figure 8 are similar to the experimental results of Jung and Bhushan [10]. The droplet volume in the experiment was about $5\,\mu\text{L}$ and was larger than the present droplets ($1\,\mu\text{L}$) but still of the same magnitude. The reasons for this discrepancy are the computational limitations and long convergence times. The two contact angles in the Cassie–Baxter state are very similar to the observed values in the experiment, e.g., for $P = 70\,\mu\text{m}$, we observed 162.68° and Jung and Bhushan [10] observed about 163°. The transition from the CB state to the Wenzel state occurred between $P = 70\,\mu\text{m}$ and $P = 82\,\mu\text{m}$ (see Figure 8), whereas Jung and Bhushan [10] observed the transition at about $P = 130\,\mu\text{m}$. This difference might be explained by the smaller size of the droplets and the difference in the surface tension, which in our case was 0.00022 N/m (La = 75), being two orders of magnitude smaller than the surface tension of water. On this basis, one can conclude that the surface tension does not have a big effect on the apparent contact angle in the CB or Wenzel states. This is in agreement with Equations (12) and (13), which are independent of the surface tension. Furthermore, one can conclude that besides the initial condition and pillar distance, the surface tension also seems to have a significant impact on the state of the droplet (either CB or Wenzel).

$$\rho(x,y,z) = \frac{\rho_l + \rho_g}{2} + \frac{\rho_g - \rho_l}{2} \cdot \tanh\left(\frac{2\left[\sqrt{(x-x_0)^2 + (y-y_0) + (z-z_0)^2} - r\right]}{5}\right) \quad (14)$$

Table 3 shows a comparison of our results for the apparent contact angle (α_{app}) obtained with LB simulations to the theoretical values (α_{app}^{theor}) calculated with the CB or Wenzel equations (Equations (12) and (13), respectively). Examples for the simulation results can be seen in Figure 6, 7 and 9.

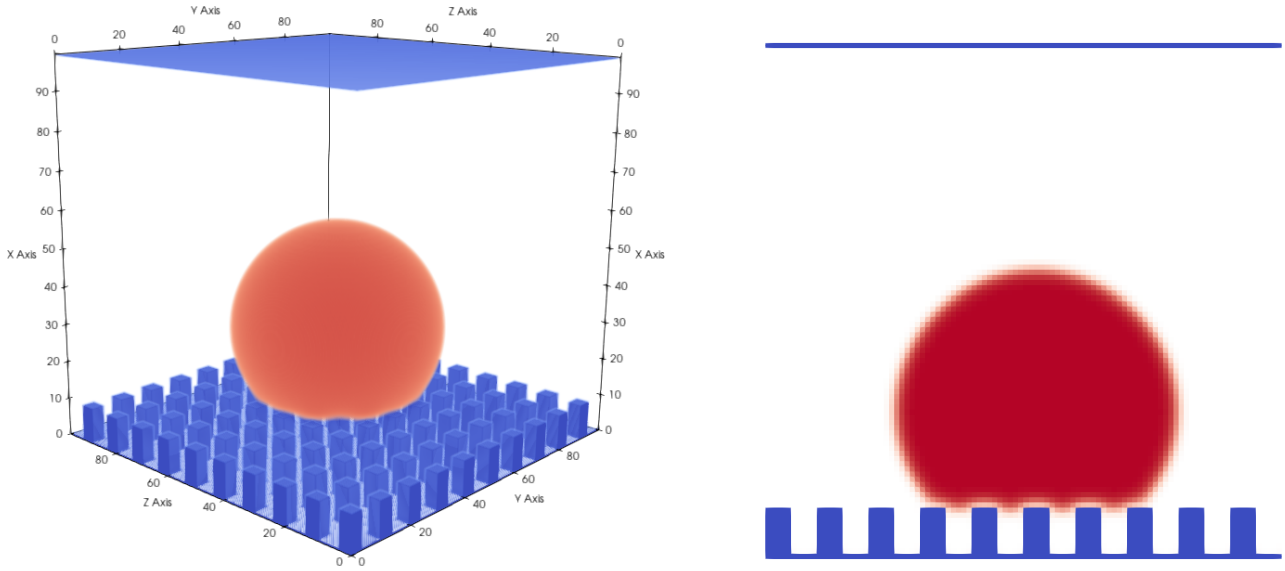

Figure 9. Droplet on a rough hydrophobic surface in the Cassie–Baxter state, with a total domain size of $100 \times 100 \times 100$ voxels. Gaseous phase is not shown for better visibility. The roughness of the surface has an impact on the apparent contact angle, which in this case is 130.82° ($G_{ads} = -157.16$, $G = -120.0$, $P = 10$, $H = 9$, $A_{top} = 5 \times 5$ lu^2).

Table 3. The apparent contact angle α_{app} on a rough surface is compared to the predictions using the Cassie–Baxter (CB) and Wenzel equations. Values in parentheses show the deviations from the LB simulations as percentages.

State	Size [voxel^3]	V_{drop} [voxel^3]	P	H	α [°] Flat LBM	α_{app} [°] Rough LBM	$\alpha_{app}^{theor,*}$ [°]	f_{SL}^{*}	α_{app}^{theor} [°]	f_{SL}	R_f
CB	$100 \times 100 \times 100$	$9 \cdot 10^4$	10	10	126.75	145.99	152.40 (4.4%)	0.2834	154.10 (5.6%)	0.25	-
CB	$100 \times 100 \times 100$	$9 \cdot 10^4$	10	10	119.76	143.24	148.99 (4.0%)	0.2838	150.94 (5.4%)	0.25	-
CB	$100 \times 100 \times 100$	$9 \cdot 10^4$	10	10	110.6	130.82	145.31 (11%)	0.2675	146.93 (12%)	0.25	-
CB	$121 \times 175 \times 175$	$5 \cdot 10^5$	20	15	119.76	131.57	-	-	138.15 (5.0%)	0.51	-
CB	$320 \times 380 \times 380$	$8 \cdot 10^6$	20	15	109	151.20	158.73 (5.0%)	0.101	159.65 (5.6%)	0.0925	-
CB	$342 \times 384 \times 384$	$14.7 \cdot 10^6$	12	8	109	159.50	162.88 (2.0%)	0.0657	163.31 (2.3%)	0.0625	-
CB	$357 \times 374 \times 374$	$14.1 \cdot 10^6$	17	8	109	162.68	167.465 (3.0%)	0.0353	168.24 (3.4%)	0.0311	-
Wenzel	$340 \times 360 \times 360$	$14.1 \cdot 10^6$	20	8	109	116.90	-	-	113.81 (−2.6%)	-	1.24
Wenzel	$357 \times 374 \times 374$	$14.1 \cdot 10^6$	25	8	109	111.58	-	-	112.06 (0.43%)	-	1.1536

To calculate the theoretical apparent contact angle in the CB state using the CB equation, one needs to determine f_{SL}, the fraction of the bottom surface of the liquid droplet in contact with the solid. Based on the micropillar structure, one can estimate $f_{SL} = \frac{A_{top}}{P^2}$. Alternatively, one can use the yellow surface in Figure 10 to determine the fraction of the bottom surface of the liquid droplet f_{SL}^* in contact with the solid more precisely, leading to slightly higher values (see Table 3). Using the simulation results to calculate f_{SL}^*, the CB equation predicted the apparent contact angles $\alpha_{app}^{theor,*}$ which were closer to our simulation results (see Table 3).

In general, it was observed that the predictions using the CB equation were closer to our simulation results for larger ratios of droplet sizes over P. This indicates that the difference between the CB equation and our simulations became larger as fewer pillars were in contact with the droplet. For higher hydrophobicities, the predictions of the CB equation were closer to our simulation results. This could indicate that the apparent contact angle also depends on other parameters such as the hydrophobicity (nanostructure) of the material and the droplet size. The simulation with a size of 121 × 175 × 175, as seen in Table 3, was equivalent to the geometry used by Xiong and Cheng [32]. They observed a contact angle of 135° for the rough surface, which was about 3° higher than our simulation results but also about 3° below the predictions from the Cassie–Baxter equation. It should be noted that, in general, our contact angle measurements were highly sensitive to the location of the reference plane. Changing the location of the reference plane by one voxel could already lead to a 3° difference in the contact angle.

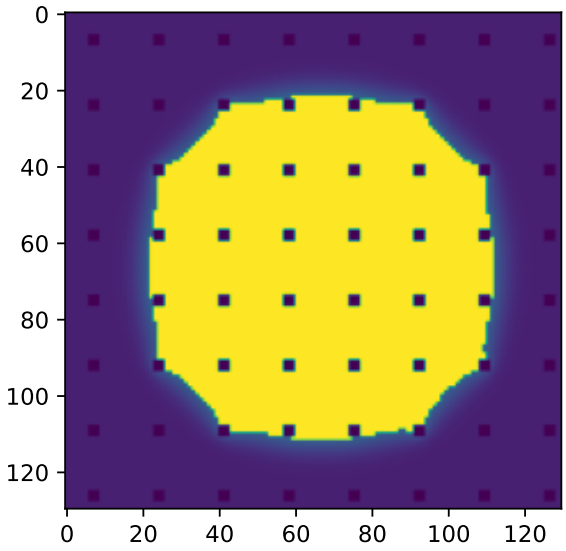

Figure 10. Slice through the droplet parallel to the surface right above the micropillars of the results seen in Figure 6. Liquid phase is shown in yellow and pillars are shown in dark blue. The yellow surface area can be used to calculate f_{SL}^*.

3.4. Liquid Entry Pressure

3.4.1. Cylindrical Pore

The liquid entry pressure (LEP) is the pressure difference between the hot water channel and the air gap, which is needed to make the water enter the pores of the hydrophobic membrane. For a perfect cylindrical pore with a radius (r_c), the LEP can be calculated using the following formula [33]:

$$\text{LEP} = \frac{-2\gamma \cos \beta_0}{r_c} \tag{15}$$

β_0 is the contact angle of a water droplet on the flat surface of the membrane material. With increasing pressure difference, the contact angle starts increasing until it reaches the critical value of β_0. After this point, the membrane material can no longer prevent the intrusion of

water. The formula for the LEP can be easily derived from the Young–Laplace equation ($\Delta p = \frac{2\gamma}{r}$), where r is the radius of the spherical meniscus, by using $-\cos\beta = \frac{r_c}{r}$. This formula is only correct if the pressure in the meniscus is constant.

To force the water to enter the membrane, we applied a constant pressure gradient along the direction that the water flow was moving (z-axis) over the full domain. This led to a non-constant pressure field in the meniscus and ultimately to a non-spherical meniscus shape (see Figure 11). The pressure decreased along the z-axis (excluding pressure jumps at the liquid–gas interfaces), which stretched the meniscus in the z-direction, leading to a "ellipsoidal like" meniscus. Lubarda and Talke [34], who analysed the equilibrium droplet shape for a similar problem (droplet on a flat surface in a gravitational field), found ellipsoidal droplets under certain conditions, supporting our observations of an ellipsoidal meniscus shape.

With $\frac{\rho(x,y,z)-\rho_c}{\rho_c} < 0.01$, we extracted the points in the vicinity of the liquid–gas interface and fitted these points to two geometrical models, a spherical $\frac{(x-x_c)^2+(y-y_c)^2+(z-z_c)^2}{r^2} = 1$ and an ellipsoid $\frac{(x-x_c)^2}{a^2} + \frac{(y-y_c)^2}{a^2} + \frac{(z-z_c)^2}{b^2} = 1$. Using the ellipsoid model led to a more than one order of magnitude lower root mean square (RMS) deviation from the data points: $\mathrm{RMS}_{ellipsoid} = 2.8 \cdot 10^{-4}$ $(3.2 \cdot 10^{-4})$ compared to $\mathrm{RMS}_{sphere} = 7.2 \cdot 10^{-3}$ $(7.3 \cdot 10^{-3})$. The values in parentheses show the RMS for a set of 20% data points (randomly chosen), which were not used for the previous calculation, to check if overfitting occurred. In addition, the lengths of the axes $a = 106.89$ and $b = 188.75$ deviated significantly from $r = 69.12$. This indicates that we indeed had an ellipsoidal-like meniscus shape rather than a spherical one.

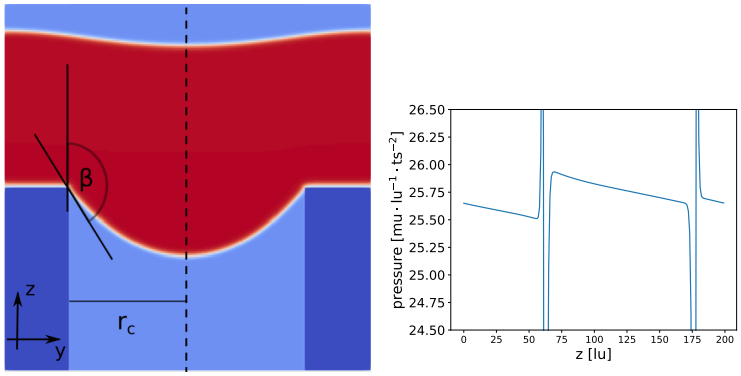

(**a**) (**b**)

Figure 11. Constant pressure gradient is applied along the z-axis (from bottom to top) in the full domain. Total domain size is $200 \times 200 \times 200$ lu^3 and the pore radius is 64 lu. In (**a**), a slice at $x = 100$ is shown; membrane material is dark blue, liquid is red, and gas is light blue. In (**b**), the pressure profile at the center of the cylindrical pore (dashed line in (**a**) at $x = 100$, $y = 100$) is shown.

A second simulation was also executed, setting a nearly constant pressure (density) for the liquid and gas phases (see Figure 12). To determine the LEP of a cylindrical pore, we chose the following setup: we removed the PBC in the z-direction (the direction of the water movement) and closed our domain at $z = 0$ and $z = 199$, initialized the fluid above the pore with a liquid density higher than the equilibrium liquid density, and chose $\rho_l = 559.4$ for the upper half of the domain $z > 99$. The pore was initialized with the equilibrium density for gas $\rho_g = 85.7$ (lower half of the domain $z < 100$). Initially, the liquid had a higher pressure, which led to an expansion of the liquid into the cylindrical pore. The pressure in the liquid started to decrease and a meniscus began to form, increasing the contact angle. If the initial pressure was sufficiently high, the critical angle β_0 was reached and the liquid started to enter the cylinder. The liquid continued entering the pore until the pressure difference between the liquid and gas was equal to the LEP.

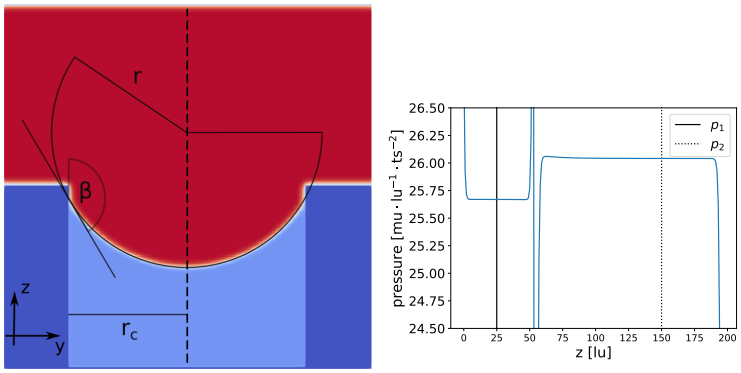

(**a**) (**b**)

Figure 12. Constant pressure in liquid and gas phases. Total domain size is $200 \times 200 \times 200$ lu^3 and the pore radius is 64 lu. In (**a**), a slice at $x = 100$ is shown; membrane material is dark blue, liquid is red, and gas is light blue. In (**b**), the pressure profile at the center of the cylindrical pore (dashed line in (**a**) at $x = 100$, $y = 100$) is shown.

The RMS for the spherical model $\text{RMS}_{sphere} = 2.1 \cdot 10^{-3} (2.2 \cdot 10^{-3})$ and the ellipsoidal model $\text{RMS}_{ellipsoid} = 1.4 \cdot 10^{-3} (1.5 \cdot 10^{-3})$ were of the same order of magnitude, and $a = 77.89$ and $b = 82.91$ deviated only slightly from $r = 75.08$, indicating that a spherical model can be applied. The values in parentheses show the RMS for a set of 20% data points (randomly chosen), which were not used for the previous calculation, to check if overfitting occurred. In addition, the contact angle $\beta_0 = 148.48$ was similar to the contact angle of a droplet on a flat surface (148.25°). The contact angle β_0 was calculated with $\cos(\beta_0) = -\frac{r_c}{r}$. Finally, we compared the LEP from our LB simulation $\Delta p = 0.3716\,\text{mu} \cdot \text{lu}^{-1} \cdot \text{ts}^{-2}$ to the value from Equation (15) $\Delta p_{pred} = 0.3740\,\text{mu} \cdot \text{lu}^{-1} \cdot \text{ts}^{-2}$. The small deviation can be explained by the discrepancies between the theoretical values of the surface tension and the contact angle, as shown in the Young–Laplace and wettability benchmarks. Overall, we found very good agreement between the LEP from the LB simulations and the predictions from Equation (15).

To validate the density (pressure) BC mentioned in the Methods section, we fixed the density at $x = 0$ and $x = x_{max}$. According to the equation of state (see Equation (7)), this will also prescribe the pressure and the phase at $x = 0$ and $x = x_{max}$. We used these BC to apply a pressure difference to one cylindrical pore. The BC in the y- and z-directions were periodic (see Figure 13).

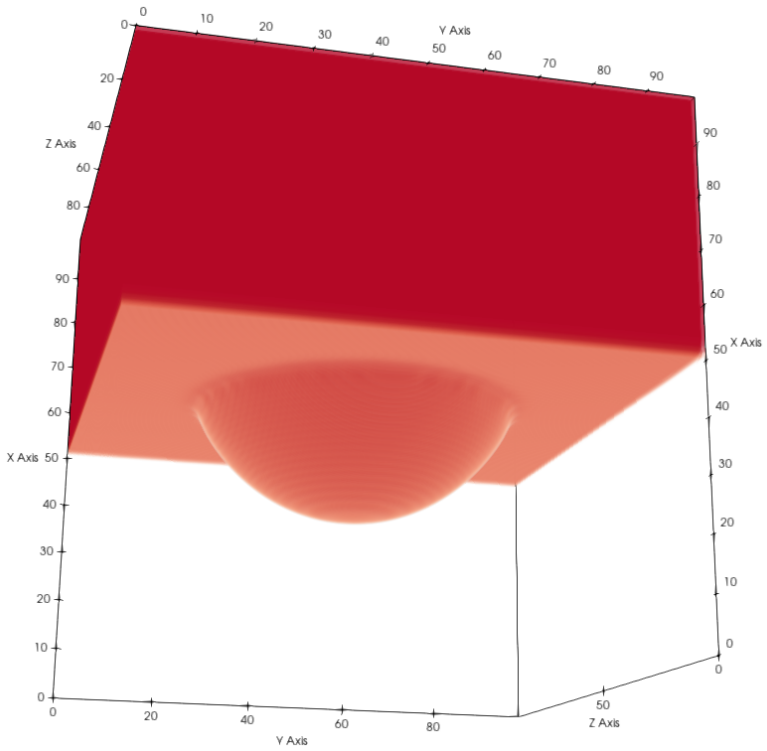

Figure 13. Liquid (red) entering a cylindrical pore. Gaseous phase and solid voxels are not shown for better visibility. We chose for this test $G_{ads} = -75.0$ and $G = -180.0$.

The pressure difference can be calculated from the radius of the spherical meniscus and the surface tension as $\Delta p_{cal} = \frac{2\gamma}{r} = 4.2468\,\mathrm{mu} \cdot \mathrm{lu}^{-1} \cdot \mathrm{ts}^{-2}$ and the prescribed pressure difference through the density BC as $\Delta p = p(\rho(x = 0)) - p(\rho(x = x_{max})) = 4.2302\,\mathrm{mu} \cdot \mathrm{lu}^{-1} \cdot \mathrm{ts}^{-2}$. The radius r can be calculated by a fit similar to the geometrical models described above. The small difference between the pressure differences can be explained by the uncertainty of the radius.

3.4.2. Realistic Distillation Membrane

To investigate the LEP of realistic membranes, we applied the aforementioned pressure boundary conditions with multiple pressure differences, as shown in Table 4, Figure 14 and Figure 15, to realistic distillation membranes. The space above the membrane material was initially filled with liquid and the rest of the domain with gas. Because of the pressure difference between $x = 0$ and $x = x_{max}$, the liquid started to penetrate the membrane structure. Depending on the magnitude of the pressure difference, we observed different liquid entry depths (LED) into the membrane structures, as shown in Table 4. Therefore, we were able to determine the breakthrough pressure of the membrane subsamples. Since the LED depends on the porosity we include the porosity profils of the invesigated subsamples in Figure 16.

For the simulations with the membrane geometry, we chose $G_{ads} = -275.0$, which corresponds to a contact angle of about 105°, which is the contact angle reported experimentally for a water droplet on a flat PTFE surface [35,36]. We report the pressure differences and the LEP for different membrane subsamples in Table 4. The results are in good agreement with the literature (measured experimentally and the values from the manufacturer). According to Racz et al. [33], the LEP for these membranes lies between 1 and 4 bar (see Table 1). The LEP for samples 1 and 4 was 2.8 bar and the LEP for sample 2 was 3.68 bar [33]. Since we used a thin membrane sample, we expected the calculated LEP to be below the value in the literature.

A necessary remark is that our model does not represent the correct density ratios between the liquid and gaseous phases (See Table 2). Since we were not interested in the dynamics of the entering process but rather whether a membrane breakthrough occurred, the mismatch of the liquid–gas density ratio should not have significantly affected the results. Due to the high hydrophobicity, the water entered the membrane relatively slowly. The liquid-entering depth was mainly governed by the contact angle (through the hydrophobicity) of the material and the surface tension of the liquid. To verify this, we calculated the liquid-entering velocity and the capillary number for the entering process ($v_{enter} = 1.5\,\mathrm{cm/s}$ and $\mathrm{Ca} = 0.00022$). The very small value of the capillary number shows that the surface tension forces are far more important than the viscous forces, similar to the Bond number and the gravity forces mentioned previously.

Table 4. Liquid entry depth in the x-direction and pressure differences for multiple membrane subsamples obtained from the LB simulations are compared to the liquid entry pressures from the experiments. Predictions are in close agreement with the experimental values.

Sample	Membrane Dimensions ($x \times y \times z$) [μm^3]	[voxels]	Δp [bar]	Liquid Entry Depth in x [μm]	LEP Experiments [33] [bar]
1	$15.6 \times 11.7 \times 11.7$	$400 \times 300 \times 300$	3.112	>15.6 (breakthrough)	2.8
	$15.6 \times 11.7 \times 11.7$	$400 \times 300 \times 300$	2.510	>15.6 (breakthrough)	(from manufacturer)
	$15.6 \times 11.7 \times 11.7$	$400 \times 300 \times 300$	1.912	2.262	
	$15.6 \times 11.7 \times 11.7$	$400 \times 300 \times 300$	0.732	0.897	
	$3.9 \times 19.5 \times 19.5$	$100 \times 500 \times 500$	0.182	0.975	
2	$15.6 \times 11.7 \times 11.7$	$400 \times 300 \times 300$	2.510	>15.6 (breakthrough)	3.68 ± 0.01
	$15.6 \times 11.7 \times 11.7$	$400 \times 300 \times 300$	1.912	3.315	
	$11.7 \times 15.6 \times 15.6$	$300 \times 400 \times 400$	2.21	10.608	
	$11.7 \times 15.6 \times 15.6$	$300 \times 400 \times 400$	1.912	6.474	
	$11.7 \times 15.6 \times 15.6$	$300 \times 400 \times 400$	1.320	1.716	
	$3.9 \times 15.6 \times 15.6$	$100 \times 400 \times 400$	0.182	0.585	
3	$11.7 \times 15.6 \times 15.6$	$300 \times 400 \times 400$	1.912	>11.7 (breakthrough)	
	$11.7 \times 15.6 \times 15.6$	$300 \times 400 \times 400$	1.320	9.789	
	$3.9 \times 19.5 \times 19.5$	$100 \times 500 \times 500$	0.182	0.897	
4	$11.7 \times 15.6 \times 15.6$	$300 \times 400 \times 400$	1.912	>11.7 (breakthrough)	2.8
	$11.7 \times 15.6 \times 15.6$	$300 \times 400 \times 400$	1.320	>11.7 (breakthrough)	(from manufacturer)
	$11.7 \times 15.6 \times 15.6$	$300 \times 400 \times 400$	1.025	9.243	
	$3.9 \times 19.5 \times 19.5$	$100 \times 500 \times 500$	0.182	0.975	

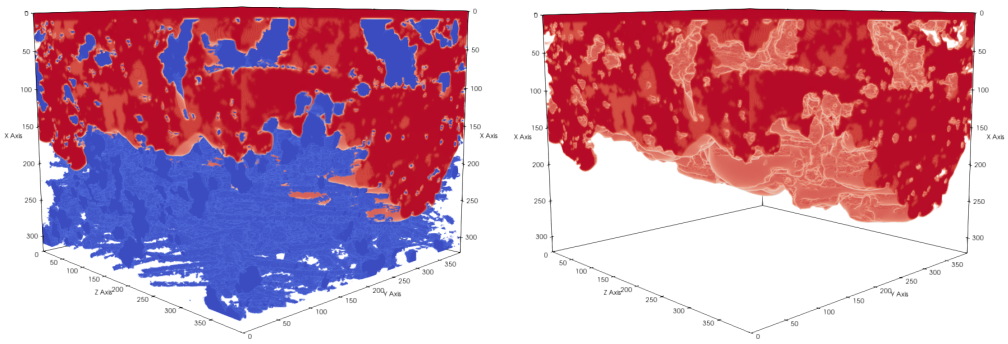

Figure 14. Subsection of sample 3 with membrane dimensions $11.7 \times 15.6 \times 15.6\,\mu\mathrm{m}^3$. The pressure difference between the top and bottom sides of a membrane is $\Delta p = 1.320$ bar. Membrane material is shown in blue and liquid in red. Liquid did not completely cross the membrane geometry.

An important property for membrane distillation is the surface area of the liquid–gas interface since it will have an impact on the evaporation flux. With the current model, we were able to determine the liquid–gas surface areas for our membrane samples (See

Figure 17). We calculated the areas in Tables 5 and 6 with the marching cubes algorithm [37] implemented in the Python skimage library [38]. Because recent work has shown that micropillars on membranes increase hydrophobicity and reduce scaling effects [9], we also added pillars on top of the membrane structure to investigate the influence on the liquid–membrane contact interface. The distance between the pillars was $P = 3.9$ µm, the pillar radius was 0.39 µm, and the pillar height was $H = 1.95$ µm. The pillars only led to a small decrease in the liquid–gas contact surface area (see Table 5), which can be explained due to the fact that they blocked the pore space. Apart from that, the impact of the pillars seemed to be negligible for the liquid–gas surface area.

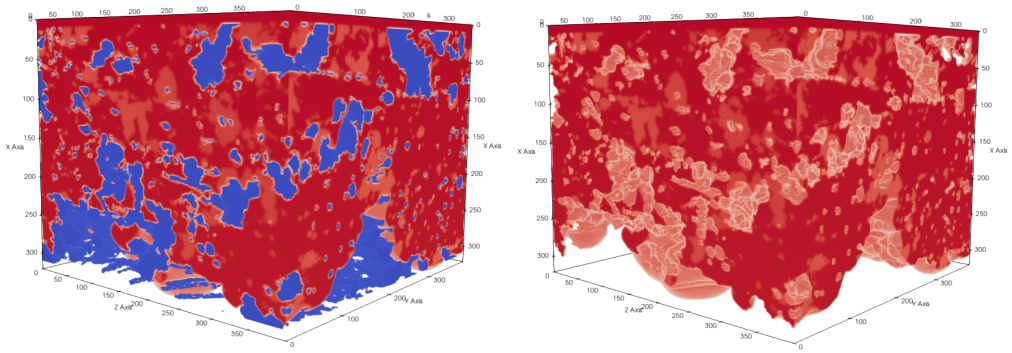

Figure 15. Subsection of sample 3 with membrane dimensions $11.7 \times 15.6 \times 15.6\,\mu m^3$. The pressure difference between the top and bottom sides of a membrane is $\Delta p = 1.912$ bar. Membrane material is shown in blue and liquid in red. Liquid fully crossed the membrane geometry.

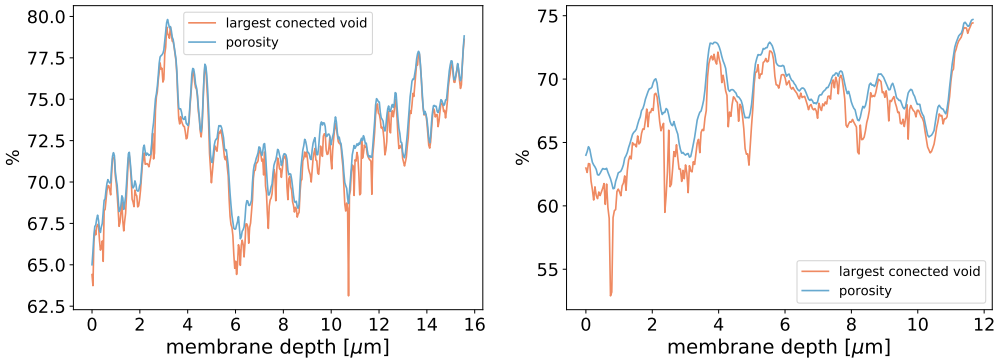

(**a**) Sample 1.

(**b**) Sample 2.

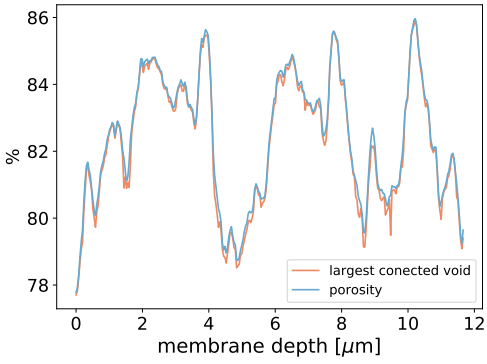

(**c**) Sample 3.

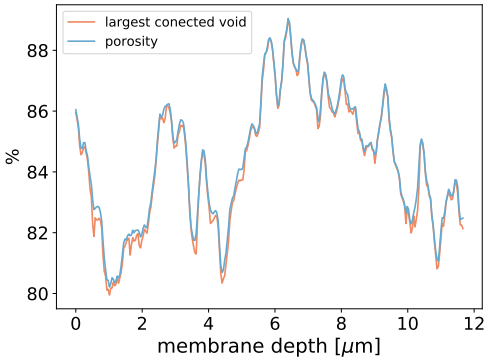

(**d**) Sample 4.

Figure 16. Porosity in dependence of the membrane depth (x-direction) for the membrane subsamples used in Table 4.

Table 5. Liquid–gas contact area. Membrane subsample size is $3.9 \times 19.5 \times 19.5$ µm^3 for sample 1, 3, and 4 and $3.9 \times 15.6 \times 15.6$ µm^3 for sample 2. $\Delta p = 0.182$ bar. $A_{l,g}$ is the liquid–gas contact surface area, A_l is the total surface area of the liquid, and A_{yz} is the area of the membrane cross-section. The velocity v is introduced parallel to the membrane plane and at a distance of 5.85 µm from the membrane plane.

Sample	v [cm/s]	Pillars	$A_{l,g}/A_l$ [%]	$A_{l,g}/A_{yz}$ [%]	A_l/A_{yz} [%]
1	0.0	no	51.96	64.48	124.10
2	0.0	no	51.3	63.99	124.74
3	0.0	no	62.4	76.96	123.33
3	1.7	no	62.4	76.96	123.33
3	0.0	yes	44.24	71.73	162.14
3	1.7	yes	44.25	71.74	162.12
4	0.0	no	64.08	81.88	127.78

Comparing the liquid–gas area ($A_{l,g}/A_{yz}$) in Table 5 to the porosity in Figure 16, one can conclude that they correlate and that the porosity is the limiting factor for the liquid–gas interface.

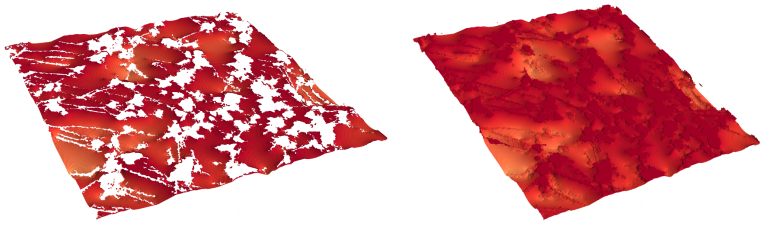

(**a**) (**b**)

Figure 17. Example of the liquid–gas contact area in (**a**) and the liquid surface area in (**b**).

3.5. Liquid–Vapour Interface within a Realistic Distillation Membrane

In MD distillation, the air in the membrane and the air gap are expected to be close to saturation, which makes condensation within the membrane material possible; therefore, we investigated the water droplet distribution within the membrane structure. Similar to Pot et al. [39], we initialized the membrane geometry with a homogeneous density between the equilibrium liquid and vapour density. As the simulation started, the two phases started to separate and the location of air–water interfaces was determined. Pot et al. [39] found a remarkably accurate prediction of the air–water interfaces within a porous medium by comparing the LB model to the experimental results. Depending on the initial mean density, different saturation states were realised.

The saturation for our simulations was $S = \frac{\rho_{init} - \rho_g}{\rho_l - \rho_g} \approx 10\%$. For the following simulations, we again chose $G_{ads} = -275.0$ and $G = -180.0$. The density field was initialized with a mean density of $\rho_{init} = 150\,\mathrm{mu\,lu^{-3}}$ with a random perturbation of up to 1%, leading to static phase separation. This allowed us to determine the water droplet agglomeration spots in the membrane structure. In Table 6, we reported some characteristics of the droplet distribution. The last column in Table 6 shows the ratio of the surface area of all liquid droplets to a single sphere with the same volume. This value correlates with the number of droplets and the droplet shape, showing that more droplets lead to a higher value.

Table 6. Surface area between liquid and gaseous phases ($A_{l,g}$) compared to the surface area of a sphere with the same volume (A_{sphere}) and the total surface area of all droplets, which includes the surface area of the droplets that are in contact with the membrane material ($A_{l,gs}$).

Sample	Domain Dimensions	V_{liquid} [%]	V_{gas} [%]	V_{solid} [%]	$A_{l,g}/A_{l,gs}$ [%]	$A_{l,g}/A_{sphere}$ [%]	$A_{l,gs}/A_{sphere}$ [%]
1	1535 × 575 × 575	7.61	69.25	23.14	48.72	328.84	674.96
2	1660 × 400 × 400	7.57	68.8	23.63	57.66	222.17	385.31
3	1601 × 550 × 550	8.42	76.62	14.96	60.53	239.15	395.09
4	650 × 950 × 950	8.33	75.9	15.77	53.29	350.47	657.66

For samples 1, 2, and 3, we found that in areas of higher porosity, the agglomerated droplets were bigger compared to areas with low porosity (See Figure 18, 19 and 20). In addition, more liquid was agglomerated in the areas of high porosity. If water droplets were formed during MD in the center of the membrane structure, it was likely that the performance decreased because of the blockage of the pores. To avoid such a scenario, a positive gradient in the porosity of the membrane material, as was the case for samples 1, 2, and 3, could be beneficial since droplet formation was more likely at the end of the membrane and not in the center. Sample 4 had the most homogeneous distribution of droplets, which was in line with the homogeneous porosity of this sample (See Figure 21).

The presented multi-phase model predicted where water droplets agglomerated if condensation took place. When droplets are formed, two processes are competing. One process is the minimisation of the surface area due to the surface tension and the other process is linked to the hydrophobicity of the membrane material. Since we are dealing with hydrophobic membrane material, the liquid has a higher chance of preferentially concentrating in high-porosity areas because more space is available and less liquid is in contact with the membrane material. Condensation can happen at nucleation sites in the steam or on the membrane surface. The hydrophobic membrane structure and the gradient in the porosity could transport small droplets towards areas of high porosity during the formation process.

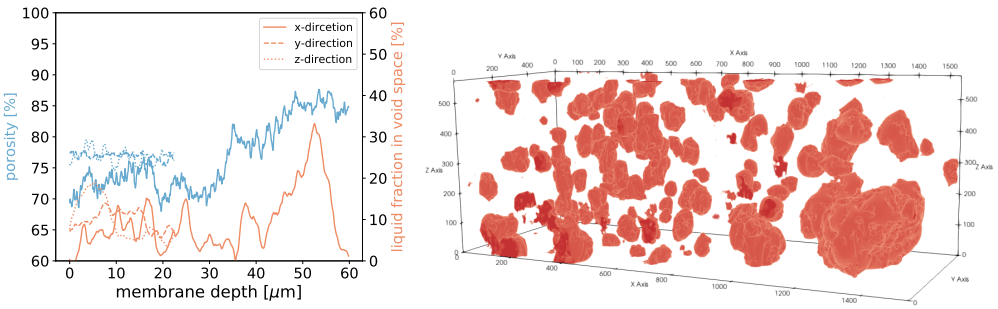

(**a**) (**b**)

Figure 18. In (**a**), the porosities along the *x*-, *y*-, and *z*-axes are shown for sample 1. Moreover, we display the fraction of void space that is occupied by liquid at a given membrane depth. In (**b**), liquid droplets are shown in red for sample 1. Gaseous phase and membrane material is not shown for better visibility. It should be noted that the convergence criterion in Equation (11) only reached $4.6 \cdot 10^{-5}$.

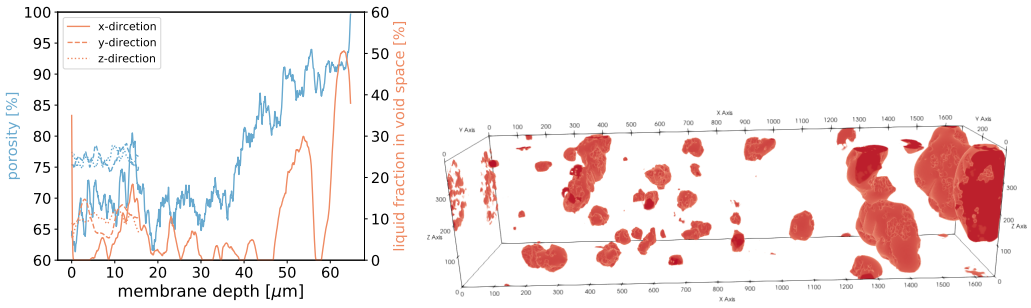

(**a**) (**b**)

Figure 19. In (**a**), the porosities along the *x*-, *y*-, and *z*-axes are shown for sample 2. Moreover, we display the fraction of void space that is occupied by liquid at a given membrane depth. In (**b**), liquid droplets are shown in red for sample 2. Gaseous phase and membrane material is not shown for better visibility. It should be noted that the convergence criterion in Equation (11) only reached $1.7 \cdot 10^{-5}$.

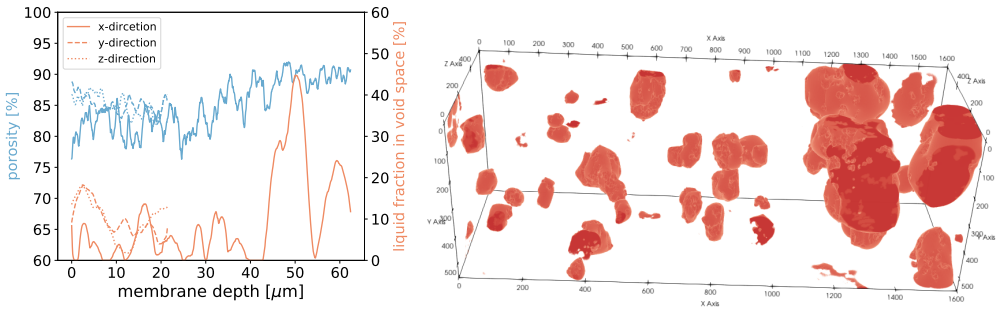

(**a**) (**b**)

Figure 20. In (**a**), the porosities along the *x*-, *y*-, and *z*-axes are shown for sample 3. Moreover, we display the fraction of void space that is occupied by liquid at a given membrane depth. In (**b**), liquid droplets are shown in red for sample 3. Gaseous phase and membrane material is not shown for better visibility.

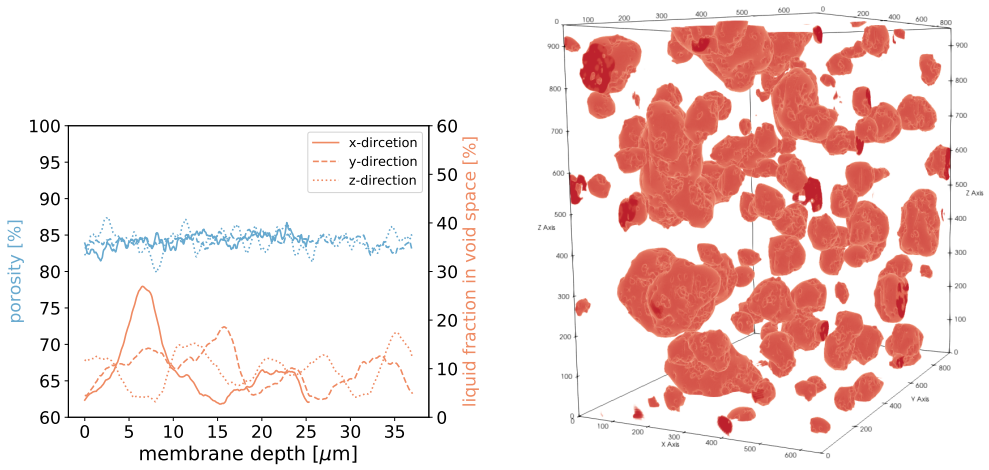

(**a**) (**b**)

Figure 21. In (**a**), the porosities along the *x*-, *y*-, and *z*-axes are shown for sample 4. Moreover, we display the fraction of void space that is occupied by liquid at a given membrane depth. In (**b**), liquid droplets are shown in red for sample 4. Gaseous phase and membrane material is not shown for better visibility. It should be noted that the convergence criterion in Equation (11) only reached $3.8 \cdot 10^{-5}$.

4. Conclusions

We performed 3D multi-phase LB simulations to gain an understanding of the phase distribution within the microporous structure of a realistic distillation membrane. We validated the model, showing good agreement with various benchmarks. Besides the typical benchmarks such as the Laplace law and the contact angle benchmark on a flat surface, we also validated the applicability to more complex membrane geometries. In particular, we validated the apparent contact angle of droplets on a rough micropillar structure against theoretical predictions and compared the LEP of our model to the values of the manufacturers and found good agreement for these benchmarks. Finally, we were able to determine the realistic contact surfaces between typical distillation membranes and water at the pore level. Additionally, we determined the air–water interface within a partially saturated membrane, finding that the droplet size and distribution correlated with the porosity of the membrane.

In future works, the surface areas reported in Table 5 and Figure 17 can be used as boundary conditions for a multi-component LB model including the evaporation and diffusion of water vapour through the porous membrane material. More investigation is needed on the influence of micropillars and flow on the liquid–gas interface. For the pillars and flow tested in this work, we found that they did not significantly influence the shape of the liquid–gas interface (see Table 5). Different micropillar structures and coatings with different hydrophobicities can be added easily to the membrane structures in future works, which can then be used to optimize the membrane structure to increase the evaporation flux.

Understanding the underlying interactions at the pore level within the membranes, as well as the interaction of membrane surface characteristics and mass transport mechanisms, is key to optimizing desalination units that work on the principle of membrane distillation. Within the framework of the lattice Boltzmann method, other physical mechanisms may be added in the future such as the precipitation and transport of contaminants within the pore structure.

Author Contributions: Conceptualization, N. I. Prasianakis and S. Leyer; methodology, T. Jäger, N. I. Prasianakis and S. Leyer; software, T. Jäger, N. I. Prasianakis and A. Mokos; validation, T. Jäger, A. Mokos, N. I. Prasianakis and S. Leyer; formal analysis, T. Jäger, N. I. Prasianakis and S. Leyer; investigation, T. Jäger, A. Mokos, N. I. Prasianakis and S. Leyer; resources, N. I. Prasianakis and S. Leyer; data curation, T. Jäger and A. Mokos; writing—original draft preparation, T. Jger and A. Mokos; writing—review and editing, T. Jäger, A. Mokos, N. I. Prasianakis and S. Leyer; visualization, T. Jäger and A. Mokos; supervision, A. Mokos, N. I. Prasianakis and S. Leyer; project administration, N. I. Prasianakis and S. Leyer; funding acquisition, N. I. Prasianakis and S. Leyer. All authors have read and agreed to the published version of the manuscript.

Funding: University of Luxembourg, Paul Scherrer Institute. This research received no external funding.

Institutional Review Board Statement: Not Applicable

Informed Consent Statement: Not Applicable

Data Availability Statement: The data presented in this study are available on request from the corresponding author.

Acknowledgments: We are thankful for the many fruitful discussions with Marie-Alix Dalle, Jemp Keup, Jerry Owusu, Fabrizio Vicari, and Filip Janasz. Moreover, we appreciate the help provided by Melvin Eichner to create the figures in this paper. The calculations in this paper were carried out using the HPC facilities at the University of Luxembourg [40] and the Swiss Supercomputing Center CSCS (project s1155). We also thank the University of Luxembourg and SwissNuclear for their support.

Conflicts of Interest: The authors declare no conflicts of interest.

References

1. Programme, U.W.W.A. *The United Nations World Water Development Report 2020: Water and Climate Change*; UNESCO: 2010.
2. Feria-Díaz, J.J.; López-Méndez, M.C.; Rodríguez-Miranda, J.P.; Sandoval-Herazo, L.C.; Correa-Mahecha, F. Commercial Thermal Technologies for Desalination of Water from Renewable Energies: A State of the Art Review. *Processes* **2021**, *9*, 262. https://doi.org/10.3390/pr9020262.
3. Ng, K.C.; Burhan, M.; Chen, Q.; Ybyraiymkul, D.; Akhtar, F.H.; Kumja, M.; Field, R.W.; Shahzad, M.W. A thermodynamic platform for evaluating the energy efficiency of combined power generation and desalination plants. *NPJ Clean Water* **2021**, *4*, 25. https://doi.org/10.1038/s41545-021-00114-5.
4. Alkhudhiri, A.; Darwish, N.; Hilal, N. Membrane distillation: A comprehensive review. *Desalination* **2012**, *287*, 2–18. Special Issue in honour of Professor Takeshi Matsuura on his 75th Birthday. https://doi.org/10.1016/j.desal.2011.08.027.
5. Chen, Q.; Burhan, M.; Akhtar, F.H.; Ybyraiymkul, D.; Shahzad, M.W.; Li, Y.; Ng, K.C. A decentralized water/electricity cogeneration system integrating concentrated photovoltaic/thermal collectors and vacuum multi-effect membrane distillation. *Energy* **2021**, *230*, 120852. https://doi.org/10.1016/j.energy.2021.120852.
6. Al-Karaghouli, A.; Kazmerski, L.L. Energy consumption and water production cost of conventional and renewable-energy-powered desalination processes. *Renew. Sustain. Energy Rev.* **2013**, *24*, 343–356. https://doi.org/10.1016/j.rser. 2012.12.064.
7. Saffarini, R.B.; Summers, E.K.; Arafat, H.A.; Lienhard V, J.H. Economic evaluation of stand-alone solar powered membrane distillation systems. *Desalination* **2012**, *299*, 55–62. https://doi.org/10.1016/j.desal.2012.05.017.
8. Souhaimi, M.K. *Membrane Distillation: Principles and Applications*; 2011.
9. Xiao, Z.; Zheng, R.; Liu, Y.; He, H.; Yuan, X.; Ji, Y.; Li, D.; Yin, H.; Zhang, Y.; Li, X.M.; He, T. Slippery for scaling resistance in membrane distillation: A novel porous micropillared superhydrophobic surface. *Water Res.* **2019**, *155*, 152–161. https://doi.org/10.1016/j.watres.2019.01.036.
10. Jung, Y.; Bhushan, B. Wetting behaviour during evaporation and condensation of water microdroplets on superhydrophobic patterned surfaces. *J. Microsc.* **2008**, *229*, 127–40. https://doi.org/10.1111/j.1365-2818.2007.01875.x.
11. Luo, K.; Xia, J.; Monaco, E. Multiscale modelling of multiphase flow with complex interactions. *J. Multiscale Model.* **2009**, *1*, 125–156.
12. Cramer, K.; Prasianakis, N.I.; Niceno, B.; Ihli, J.; Leyer, S. Three-Dimensional Membrane Imaging with X-ray Ptychography: Determination of Membrane Transport Properties for Membrane Distillation. *Transp. Porous Media* **2021**, *138*, 265–284..
13. Persad, A.H. Statistical Rate Theory Expression for Energy Transported during Evaporation. Ph.D. Thesis, Mechanical and Industrial Engineering University of Toronto, 2014.
14. Persad, A.H.; Ward, C.A. Expressions for the Evaporation and Condensation Coefficients in the Hertz-Knudsen Relation. *Chem. Rev.* **2016**, *116*, 7727–7767. https://doi.org/10.1021/acs.chemrev.5b00511.
15. Prasianakis, N.I.; Rosén, T.; Kang, J.; Eller, J.; Mantzaras, J.; Büichi, F.N. Simulation of 3D Porous Media Flows with Application to Polymer Electrolyte Fuel Cells. *Commun. Comput. Phys.* **2013**, *13*, 851–866. https://doi.org/10.4208/cicp.341011.310112s.
16. Rosen, T.; Eller, J.; Kang, J.; Prasianakis, N.I.; Mantzaras, J.; Büchi, F.N. Saturation dependent effective transport properties of PEFC gas diffusion layers. *J. Electrochem. Soc.* **2012**, *159*, F536.
17. Khayet, M.; Godino, P.; Mengual, J. Modelling Transport Mechanism Through A Porous Partition. *J.-Non-Equilib. Thermodyn.* **2001**, *26*, 1–14. https://doi.org/10.1515/JNETDY.2001.001.
18. Gong, W.; Zu, Y.; Chen, S.; Yan, Y. Wetting transition energy curves for a droplet on a square-post patterned surface. *Sci. Bull.* **2017**, *62*, 136–142. https://doi.org/10.1016/j.scib.2016.12.003.
19. Cassie, A.B.D.; Baxter, S. Wettability of porous surfaces. *Trans. Faraday Soc.* **1944**, *40*, 546–551. https://doi.org/10.1039/TF9444000546.
20. Prasianakis, N.I.; Karlin, I.V.; Mantzaras, J.; Boulouchos, K.B. Lattice Boltzmann method with restored Galilean invariance. *Cphysical Rev. E* **2009**, *79*, 066702. https://doi.org/10.1103/PhysRevE.79.066702.
21. Qian, Y.H.; D'Humières, D.; Lallemand, P. Lattice BGK Models for Navier-Stokes Equation. *Europhys. Lett. (EPL)* **1992**, *17*, 479–484. https://doi.org/10.1209/0295-5075/17/6/001.
22. Peng, C.; Tian, S.; Li, G.; Sukop, M.C. Single-component multiphase lattice Boltzmann simulation of free bubble and crevice heterogeneous cavitation nucleation. *Phys. Rev. E* **2018**, *98*, 023305. https://doi.org/10.1103/physreve.98.023305.
23. Kunes, J. *Dimensionless Physical Quantities in Science and Engineering*; 2012.
24. Safi, M.A.; Mantzaras, J.; Prasianakis, N.I.; Lamibrac, A.; Büchi, F.N. A pore-level direct numerical investigation of water evaporation characteristics under air and hydrogen in the gas diffusion layers of polymer electrolyte fuel cells. *Int. J. Heat Mass Transf.* **2019**, *129*, 1250–1262. https://doi.org/10.1016/j.ijheatmasstransfer.2018.10.042.
25. Shan, X.; Chen, H. Lattice Boltzmann model for simulating flows with multiple phases and components. *Phys. Rev. E* **1993**, *47*, 1815–1819. https://doi.org/10.1103/PhysRevE.47.1815.
26. Shan, X.; Chen, H. Simulation of nonideal gases and liquid-gas phase transitions by the lattice Boltzmann equation. *Phys. Rev. E* **1994**, *49*, 2941. https://doi.org/10.1103/PhysRevE.49.2941.
27. Sukop, M.C.; Thorne, D.T. *Lattice Boltzmann Modeling*; 2006.
28. Zou, Q.; He, X. On pressure and velocity boundary conditions for the lattice Boltzmann BGK model. *Phys. Fluids* **1997**, *9*, 1591–1598, https://doi.org/10.1063/1.869307.
29. Zong, Y.; Li, M.; Wang, K. Outflow boundary condition of multiphase microfluidic flow based on phase ratio equation in lattice Boltzmann method. *Phys. Fluids* **2021**, *33*, 073304, https://doi.org/10.1063/5.0058045.

30. Safi, M.A.; Prasianakis, N.I.; Mantzaras, J.; Lamibrac, A.; Büchi, F.N. Experimental and pore-level numerical investigation of water evaporation in gas diffusion layers of polymer electrolyte fuel cells. *Int. J. Heat Mass Transf.* **2017**, *115*, 238–249. https://doi.org/10.1016/j.ijheatmasstransfer.2017.07.050.
31. Wenzel, R.N. Resistance of Solid Surfaces to Wetting by Water. *Ind. Eng. Chem.* **1936**, *28*, 988–994.
32. Xiong, W.; Cheng, P. Mesoscale simulation of a molten droplet impacting and solidifying on a cold rough substrate. *Int. Commun. Heat Mass Transf.* **2018**, *98*, 248–257. https://doi.org/10.1016/j.icheatmasstransfer.2018.09.001.
33. Racz, G.; Kerker, S.; Kovács, Z.; Vatai, G.; Ebrahimi, M.; Czermak, P. Theoretical and Experimental Approaches of Liquid Entry Pressure Determination in Membrane Distillation Processes. *Period. Polytech. Chem. Eng.* **2014**, *58*, 81–91. https://doi.org/10.3311/PPch.2179.
34. Lubarda, V.; Talke, K. Analysis of the Equilibrium Droplet Shape Based on an Ellipsoidal Droplet Model. *Langmuir ACS J. Surfaces Colloids* **2011**, *27*, 10705–10713. https://doi.org/10.1021/la202077w.
35. 2021. Available online: https://www.accudynetest.com/polymer_surface_data/ptfe.pdf (accessed on 1 January 2020).
36. Rezaei, M.; Warsinger, D.M.; Lienhard V, J.H.; Duke, M.C.; Matsuura, T.; Samhaber, W.M. Wetting phenomena in membrane distillation: Mechanisms, reversal, and prevention. *Water Res.* **2018**, *139*, 329–352. https://doi.org/10.1016/j.watres. 2018.03.058.
37. Lorensen, W.E.; Cline, H.E. Marching Cubes: A High Resolution 3D Surface Construction Algorithm. *SIGGRAPH Comput. Graph.* **1987**, *21*, 163–169. https://doi.org/10.1145/37402.37422.
38. van der Walt, S.; Schönberger, J.L.; Nunez-Iglesias, J.; Boulogne, F.; Warner, J.D.; Yager, N.; Gouillart, E.; Yu, T.; the scikit-image contributors. scikit-image: Image processing in Python. *PeerJ* **2014**, *2*, e453. https://doi.org/10.7717/peerj.453.
39. Pot, V.; Peth, S.; Monga, O.; Vogel, L.; Genty, A.; Garnier, P.; Vieublé-Gonod, L.; Ogurreck, M.; Beckmann, F.; Baveye, P. Three-dimensional distribution of water and air in soil pores: Comparison of two-phase two-relaxation-times lattice-Boltzmann and morphological model outputs with synchrotron X-ray computed tomography data. *Adv. Water Resour.* **2015**, *84*, 87–102. https://doi.org/10.1016/j.advwatres.2015.08.006.
40. Varrette, S.; Cartiaux, H.; Peter, S.; Kieffer, E.; Valette, T.; Olloh, A. Management of an Academic HPC & Research Computing Facility: The ULHPC Experience 2.0. In Proceedings of the 6th ACM High Performance Computing and Cluster Technologies Conf. (HPCCT 2022), Fuzhou, China, 8–10 July 2022; Association for Computing Machinery (ACM): 2022.

4

THEORETICAL AND NUMERICAL CONSTANT MEAN CURVATURE SURFACE AND LIQUID ENTRY PRESSURE CALCULATIONS FOR A COMBINED PILLAR–PORE STRUCTURE

First author publication in the peer reviewed journal MDPI coatings. URL to the paper: https://www.mdpi.com/2079-6412/13/5/865. A detailed list of the author contribution can be found at the end of the paper.

Having developed and validated a powerful 3D multiphase model presented in chapter 3, which also allows the simulation of fluid–solid interactions, we can now apply it to specific 3D geometries.

In general, it is desirable to gain a better understanding of the interface shape of pressurized liquids, which is important for various applications, including microfluidics and biochemical analysis.

Advanced techniques in microfabrication have sparked increased interest in various rough structures such as for example pillar–pore formations [1]. For many applications it is crucial to prevent or facilitate liquid intrusion into rough structures which finds application e.g. for low–surface–tension liquids in oil transportation, water/oil separation and thermal management of micro/power electronic systems. This paper explores the liquid entry pressure of such a hydrophobic pillar–pore structure and the corresponding shape of the liquid–gas interface under pressurized conditions. We conducted a theoretical analysis of the constant mean curvature problem for rotationally symmetric cases, providing an analytical expression for the liquid entry pressure of such structures. Additionally, we derived the shape of the liquid–gas interface and formulated a method for locating the minimum of the interface.

To validate our results, we compared them with multiphase Lattice Boltzmann simulations, where equilibrium contact angles ranging from 157° to 102° were examined and we found a very good agreement for the interface shape. The cases presented in this study can also serve as benchmarks for developing and validating numerical multiphase models.

coatings

MDPI

Article

Theoretical and Numerical Constant Mean Curvature Surface and Liquid Entry Pressure Calculations for a Combined Pillar–Pore Structure

Tobias Jäger [1,*], Jemp Keup [1], Nikolaos I. Prasianakis [2] and Stephan Leyer [1]

[1] Department of Engineering, Faculty of Science, Technology and Medicine, University of Luxembourg, L-1359 Luxembourg, Luxembourg; stephan.leyer@uni.lu (S.L.)
[2] Transport Mechanisms Group, Laboratory for Waste Management, Paul Scherrer Institute, 5232 Villigen, Switzerland; nikolaos.prasianakis@psi.ch
* Correspondence: tobias.jaeger@uni.lu; Tel.: +352-466-644-9621

Abstract: Modern microfabrication techniques have led to a growing interest in micropillars and pillar–pore structures. Therefore, in this paper a study of the liquid entry pressure of a hydrophobic pillar–pore structure and the corresponding liquid–gas interface shape for the pressurized liquid is presented. We theoretically analysed the constant mean curvature problem for the rotationally symmetric case and determined an analytical expression for the liquid entry pressure of a hydrophobic pillar–pore structure. Furthermore, the shape of the liquid–gas interface as well as a formula for the location of the minimum were derived. The results are useful for designing geometries with specific properties, such as preventing or facilitating liquid intrusion into rough structures. We compared these results to multiphase lattice Boltzmann simulations where equilibrium contact angles in the range of 157° to 102° were tested. In our further analysis, we compared theoretical findings from previous works to our lattice Boltzmann simulations. The presented cases can serve as a benchmark for the development and validation of numerical multiphase models.

Keywords: lattice Boltzmann method; multiphase flow; liquid entry pressure; constant mean curvature surface; pillar; pore; interface shape

Citation: Jäger, T.; Keup, J.; Prasianakis, N.I.; Leyer, S. Theoretical and Numerical Constant Mean Curvature Surface and Liquid Entry Pressure Calculations for a Combined Pillar–Pore Structure. *Coatings* **2023**, *13*, 865. https://doi.org/10.3390/coatings13050865

Academic Editor: Emerson Coy

Received: 14 March 2023
Revised: 17 April 2023
Accepted: 27 April 2023
Published: 3 May 2023

1. Introduction

Materials with hydrophobic surfaces are of interest for many industrial applications. Recently, there has been a great deal of interest in so-called superhydrophobic surfaces, which are created by a combination of chemical treatment and local roughness to increase hydrophobicity, i.e., to reduce the wettability of a surface. Microfabrication techniques have made it possible to produce a variety of artificial superhydrophobic surfaces with precisely controlled local roughness on the micrometer scale [1–3]. In addition, membrane treatments such as micropillars and hydrophobic coatings can reduce scaling and extend the lifetime of a membrane [3]. Following Agonafer et al. [4], the ability to manipulate fluid interfaces, such as retaining fluid behind or within porous structures, is useful in numerous applications, including microfluidics and biochemical analysis. In their work they fabricated customized pillar–pore structures at micrometer scale and analysed the wetting behaviour. Many applications, such as oil transportation [5], water/oil separation [6,7], and thermal management of micro/power electronic systems [8], call for porous structures with the ability to retain low-surface-tension liquids (such as dielectric refrigerants and oils) against an imposed pressure difference [4].

Among other properties, hydrophobic porous membranes are characterised by their liquid entry pressure (LEP). The LEP is the pressure difference that needs to be applied to a dry membrane in order to force the liquid to penetrate the interior of the membrane. For structures such as a cylindrical or a torus–shaped pore, analytical expressions for the LEP have been derived [9,10].

The shape of the liquid–gas interface for a pressurized liquid on top of a hydrophobic structure is governed by the Young–Laplace equation, which describes the capillary pressure difference sustained across the interface between two static fluids. The three–phase gas–liquid–solid contact line is assumed to be attached to the outer edge of the hydrophobic structure [11]. The most general form of the Young—Laplace equation is given by [9,12]:

$$\Delta p = \gamma \operatorname{div} \hat{\mathbf{n}} = 2\gamma H_f = \gamma \left(\frac{1}{R_1} + \frac{1}{R_2} \right) \tag{1}$$

Here γ is the surface tension, $\operatorname{div} \hat{\mathbf{n}}$ is the divergence of the unit normal vector of the liquid–gas interface, H_f is the mean curvature, and R_1 and R_2 are the principal radii of curvature at a given point on the liquid–gas interface.

For a static situation without body forces such as, e.g., gravity, the pressure within each fluid phase is constant, leading to a surface of constant mean curvature (CMC) [11]. This also means that Δp is constant at every point of the liquid–gas interface. It follows directly that solely $q := \Delta p / \gamma$ and the boundary condition, in the form of the three-phase gas–liquid–solid contact line, define the shape of the liquid–gas interface.

The LEP for a cylindrical pore is the pressure difference that is required for water to enter a hydrophobic cylindrical pore and wet the pore wall. For a perfect cylindrical pore with a radius (r_c), the LEP can be calculated using the following formula [9,10,13]:

$$\mathrm{LEP} = \frac{-2\gamma \cos \alpha_0}{r_c} \tag{2}$$

Thereby α_0 is the equilibrium contact angle of a water droplet on a flat surface of the pore material. The equilibrium contact angle α_0 increases with increasing hydrophobicity. The magnitude of the contact angle can be calculated using Young's equation [14]. A material is considered hydrophobic if the equilibrium contact angle is bigger than 90°. More details regarding equilibrium contact angle determination can be found, e.g., in [15–17].

For a vanishing pressure difference, the liquid–gas interface is flat. Applying a pressure difference leads to a spherical meniscus with radius r_m (see Figure 1). As the pressure difference increases, r_m shrinks. This results in an increase in the contact angle until it reaches the critical value of α_0. At this point, the hydrophobic material can no longer prevent the intrusion of water. The corresponding formula for this LEP can be derived directly from the Young–Laplace Equation (1) with $R_1 = R_2 = r_m$ and by using the trigonometric relation $-\cos \alpha = r_c / r_m$. Equation (2) is only correct if the pressure in the meniscus is constant and gravitational effects are negligible. In [18], we showed that a multiphase LB method can correctly predict the LEP pressure for a cylindrical pore.

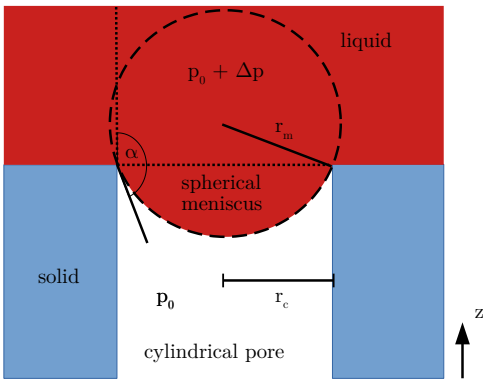

Figure 1. Side view of a cylindrical pore with spherical meniscus.

Zheng et al. [19] showed that the critical pressure difference Δp_{crit} to enter a structure decorated with periodic micropillars can be calculated with the following force balance approach:

$$\Delta p_{crit}(A_c - A) = -\gamma l \cos(\alpha_0) \quad (3)$$

A_c is the area of the periodically repeated cell, l is the perimeter of the pillar, and A is the pillar cross-sectional area. In this work we focus on the special case of round pillars with radius r_p. Therefore, $A_c = P \times P$, $A = \pi r_p^2$, and $l = 2\pi r_p$ (see Figure 2).

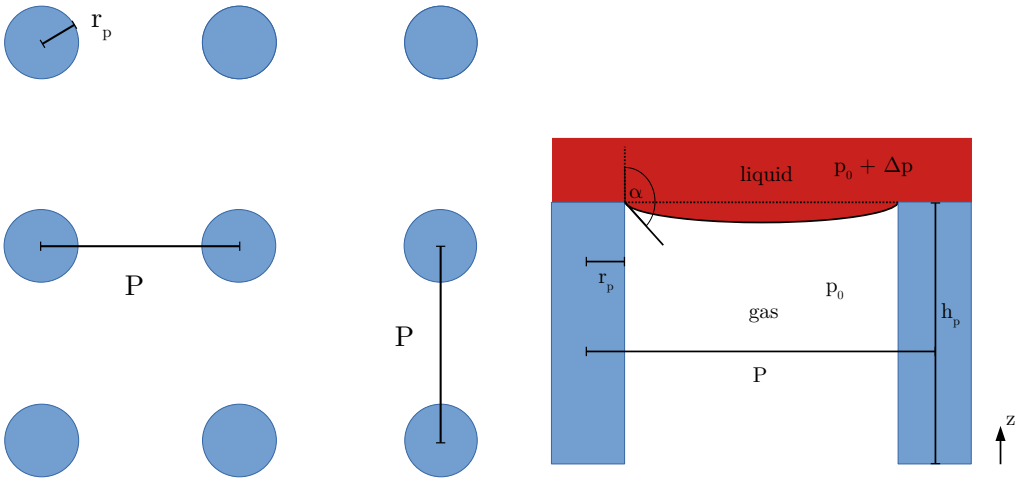

(**a**) (**b**)

Figure 2. Top view (**a**) and side view (**b**) for a periodically repeated pillar structure.

Zheng et al. [19] have addressed the issue of interfacial deformation by using a finite element method to calculate the shape of the liquid–gas interface for a statically pressurized liquid in contact with a superhydrophobic surface. Zheng et al. [19] found good agreement of Equation (3) with the predictions of the finite element method (FEM). Lobaton and Salamon [11] numerically solved a Lagrangian evolution problem to obtain the surface of constant mean curvature for a given pressure difference. In [18] we showed that a multiphase lattice Boltzmann method can also be used to determine the shape of the static liquid–gas interface.

In this work we determine an analytical expression for the LEP of a combined pillar–pore structure. This is the critical pressure difference Δp_{crit} sustained across the liquid–gas interface at which the liquid begins to enter a cylindrical pore with a cylindrical pillar in the centre of the pore (see Figure 3). We also provide a theoretical analysis of the liquid–gas interface shape and compare the theoretical findings with multiphase lattice Boltzmann simulation results. A deeper understanding of the interface shape for this specific pillar–pore structure can be useful for designing surfaces with specific properties, such as preventing or facilitating liquid intrusion. Here we assume that the pillar and the pore wall have the same surface properties, which leads to an identical equilibrium contact angle.

We also compare the critical pressure difference Δp_{crit} to numerical results obtained with the lattice Boltzmann (LB) method. Furthermore, we compare the predictions of Equation (3) from Zheng et al. [19] to numerical results obtained with the LB method.

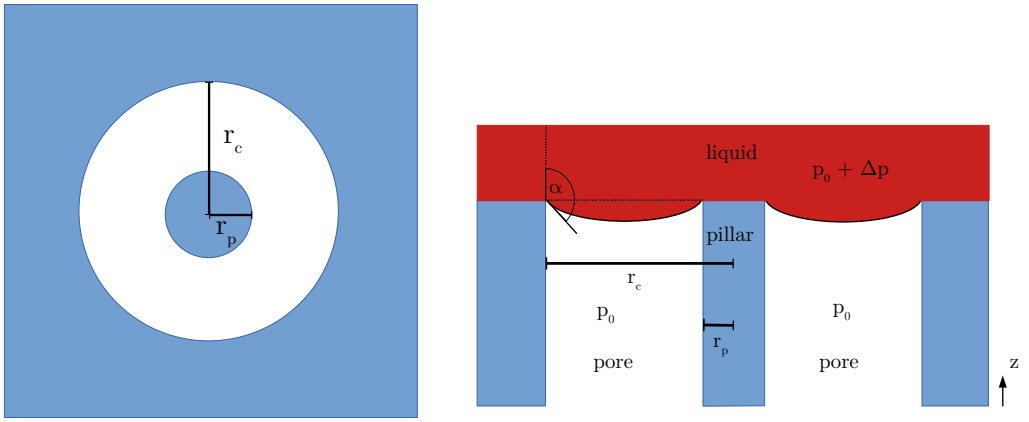

(**a**) (**b**)

Figure 3. Top view (**a**) and side view (**b**) for a combined pillar–pore structure. Here r_c is the radius of the cylindrical pore and r_p is the radius of the cylindrical pillar.

2. Mathematical Background

The relationship $g(x,y,z) = f(x,y) - z = 0$ defines a surface, and $\mathbf{n} = \nabla g(x,y,z)$ is a vector normal to this surface. With the norm $|\mathbf{n}| = \sqrt{1 + (\partial_x f(x,y))^2 + (\partial_y f(x,y))^2}$, one obtains the unit normal vector $\hat{\mathbf{n}} = \mathbf{n}/|\mathbf{n}|$. Inserting this into the Young–Laplace Equation (1), one obtains a partial differential equation (PDE) in Cartesian coordinates

$$\partial_x \left(\frac{f(x,y)}{\sqrt{1 + (\partial_x f(x,y))^2 + (\partial_y f(x,y))^2}} \right) + \partial_y \left(\frac{f(x,y)}{\sqrt{1 + (\partial_x f(x,y))^2 + (\partial_y f(x,y))^2}} \right) = -\frac{\Delta p}{\gamma} \quad (4)$$

for a surface of arbitrary shape, as stated, e.g., in [19].

In the case of a combined pillar–pore structure, cylindrical coordinates (r, φ, z) are appropriate to describe the problem. Therefore, we use the corresponding divergence div and gradient ∇.

$$\operatorname{div} \hat{\mathbf{n}} = \frac{1}{r}\frac{\partial}{\partial r}(r\hat{n}_r) + \frac{1}{r}\frac{\partial \hat{n}_\varphi}{\partial \varphi} + \frac{\partial \hat{n}_z}{\partial z} \quad (5)$$

$$\nabla g(r,\varphi,z) = \frac{\partial g}{\partial r}\hat{\mathbf{e}}_r + \frac{1}{r}\frac{\partial g}{\partial \varphi}\hat{\mathbf{e}}_\varphi + \frac{\partial g}{\partial z}\hat{\mathbf{e}}_z \quad (6)$$

Analogous to the expression in Cartesian coordinates, $g(r,\varphi,z) = f(r,\varphi) - z = 0$ defines a surface in cylindrical coordinates and $\mathbf{n} = \nabla g(r,\varphi,z)$ is a vector normal to the surface. For the special case of a rotationally symmetric solution, the definition of the surface simplifies to:

$$g(r,z) = f(r) - z = 0 \quad (7)$$

The normal vector $\mathbf{n}$ can be found with the gradient:

$$\mathbf{n} = \nabla g(r,z) = \frac{\partial f(r)}{\partial r}\hat{\mathbf{e}}_r - \hat{\mathbf{e}}_z \quad (8)$$

$$|\mathbf{n}| = \left(1 + \left(\frac{\partial f(r)}{\partial r}\right)^2\right)^{\frac{1}{2}} \quad (9)$$

The norm $|\mathbf{n}|$ can be used to derive the unit normal vector $\hat{\mathbf{n}}$:

$$\hat{\mathbf{n}} = \frac{\mathbf{n}}{|\mathbf{n}|} = \underbrace{\frac{\partial f(r)}{\partial r}\left(1+\left(\frac{\partial f(r)}{\partial r}\right)^2\right)^{-\frac{1}{2}}}_{\hat{n}_r}\hat{\mathbf{e}}_r \underbrace{-\left(1+\left(\frac{\partial f(r)}{\partial r}\right)^2\right)^{-\frac{1}{2}}}_{\hat{n}_z}\hat{\mathbf{e}}_z \tag{10}$$

3. Numerical Methods

To capture the interface shape of a liquid under pressure, one can solve the PDE (4) numerically, e.g., with the FEM, as done by Zheng et al. [19]. Lobaton and Salamon [11] used a different approach and solved a Lagrangian evolution problem to obtain the static interface shape. Both methods assume a fixed three-phase contact line or a fixed contact angle attached to the hydrophobic solid structure, which then serves as a static boundary condition for the PDE. To overcome this limitation, one can use a multiphase model that includes fluid–solid interaction. Such a model makes it possible to calibrate the equilibrium contact angle that the liquid forms with the solid walls and allows simulation of the flow of liquid and gas. This is at the cost of increased computational complexity, as the entire fluid is resolved, whereas in the above methods only the static interface shape is captured.

Mesoscopic models provide accurate solutions for complex 3D micro- and nano-scale structures. In general, one differentiates between lattice- and particle-based methods [20]. The lattice Boltzmann (LB) framework is a promising approach since it can capture complex boundary conditions such as rough surfaces [21] and is suitable for parallelization and GPU-accelerated computations [20,22,23]. It allows simulations in the continuum flow regime as well as in the slip flow regime [24].

The LB method is a popular method for which a wide range of models exist, capable of solving non-isothermal flow, evaporation [25], and multiphysics problems where several physical phenomena are coupled. This includes simulations of fluid–structure interactions, where the motion of a solid body affects the fluid flow [26,27].

In this work, an isothermal multiphase lattice Boltzmann (LB) method is used to model the liquid–gas interface. We applied a D3Q27 multiphase LB method with 27 discrete velocities ($\mathbf{c}_i$, $i = 0.26$) at every lattice point in a 3D space [28] to validate the theoretical findings. The LB method simulates the evolution of the discrete density distribution function $f_i(\mathbf{x}, t)$, which describes the probability of finding a particle at position $\mathbf{x}$ with velocity $\mathbf{c}_i$ at time t. The time evolution can be written as:

$$f_i(\mathbf{x}+\mathbf{c}_i\Delta t, t+\Delta t) - f_i(\mathbf{x}, t) = -\frac{1}{\tau}\left[f_i(\mathbf{x}, t) - f_i^{eq}(\rho, \mathbf{v}, \mathbf{x}, t)\right] \tag{11}$$

The term on the right is the Bhatnagar–Gross–Krook approximation of the collision operator, reflecting the inter-particle collisions in the fluid [29]. The relaxation time τ is linked to the viscosity of the fluid. In the LB method, the discrete one-body distribution function f_i is relaxed towards a local equilibrium f_i^{eq}. The term on the left represents the propagation of the density distribution function. In this step, the f_is are streamed to their respective neighbouring cells.

The LB method is usually not simulated with SI units but as a similarity problem. For our LB simulation, we used the common LB unit convention: the time step (ts) was set to one, the lattice spacing (Δx) was set to one lattice unit (lu), and the mass of one fluid particle (m) was set to one mass unit (mu). This way, the LB unit convention gave $\Delta t = 1$ ts, $\Delta x = 1$ lu, $m = 1$ mu. Therefore, the speed of sound equalled $c_s = 1/\sqrt{3}\,\mathrm{lu/ts}$ for the D3Q27 lattice. As is typically done for such multiphase LB simulations, e.g., in Peng et al. [30], for increased stability and faster numerical convergence we chose $\tau = 1$ ts for our simulations. This corresponds to a kinematic viscosity of $1/6\,\mathrm{lu}^2/\mathrm{ts}$ ($\nu = c_s^2(\tau - 0.5)\Delta t$).

The Bond number ($\mathrm{Bo} = \Delta\rho g L^2/\gamma$) describes the ratio of gravitational to capillary forces [31]: γ represents the surface tension, $\Delta\rho$ is the density difference between the liquid

and gaseous phases, g is the gravitational acceleration, and L is the characteristic length. In this paper, we focus exclusively on examples with Bo $\ll 1$ so that gravitational effects can be neglected.

The LB method is designed to reproduce the Navier–Stokes equation in the hydrodynamic limit [28]. Macroscopic quantities such as density and velocity can be calculated by summing up the discrete populations f_i and discrete velocities c_i [28].

$$\rho = \sum_{i=0}^{26} f_i \tag{12}$$

$$\mathbf{v} = \frac{1}{\rho} \sum_{i=0}^{26} f_i \mathbf{c}_i \tag{13}$$

In this case, the guided equilibrium (GE) model proposed in [28,32] was used. Further implementation details can be found in [18,28,32].

The Shan–Chen multiphase model was chosen [30,33,34]. The interaction between fluid particles was achieved by including the following force:

$$\mathbf{F} = -G\psi(\mathbf{x}, t) \sum_{i=0}^{26} w_i \psi(\mathbf{x} + \mathbf{c}_i \Delta t, t) \mathbf{c}_i \tag{14}$$

This leads to the non-ideal equation of state shown in Equation (15). The function $\psi(\rho)$ describes the interaction potential and depends on the density, whereas G describes the interaction strength between the fluid particles and allows the surface tension to be adjusted.

$$p(\rho) = \rho RT + \frac{GRT}{2} (\psi(\rho))^2 \tag{15}$$

For the interaction between the fluid and solid, the following force is introduced, with the function $s(\mathbf{x})$ giving 1 for solid nodes and 0 for fluid nodes [30,35].

$$\mathbf{F}_{ads} = -G_{ads} \psi(\mathbf{x}, t) \sum_{i=0}^{26} w_i s(\mathbf{x} + \mathbf{c}_i \Delta t, t) \mathbf{c}_i \tag{16}$$

The parameter G_{ads} correlates linearly with the contact angle α_0 for a given G value, as shown in the contact angle benchmark in [18]. G_{ads} allows tuning the contact angle of a liquid droplet on the flat solid phase. Therefore, with G_{ads} the hydrophobicity can be controlled. Implementation details on how the forces are incorporated into the LB method can be found in [18,30,33,34].

Additionally, a non-slip (bounce-back) boundary condition was employed for the fluid–solid interaction. Periodic boundary conditions (PBCs) were employed at the border of the domain. If not stated otherwise, PBCs were used in all directions, x, y, and z.

For the simulations in this work we used $G = 180.0$, which results in a surface tension of: $\gamma = 68.45\,\mathrm{mu\,ts^{-2}}$ in the LB unit convention. Further implementation details and validation benchmarks for the surface tension calculation can be found in [18]. Since the shape of the CMC surface depends only on the boundary conditions (three-phase contact line) and $q := \Delta p / \gamma\,[\mathrm{lu}^{-1}]$, it is sufficient to ensure that q and α_0 correspond to the real physical problem. Dimensionalization of the problem works as follows: $\Delta p^{SI} / \gamma^{SI} = q^{SI} = q / \Delta x^{SI}$. Here Δx^{SI} is the lattice spacing in SI units. The convergence criterium stated in Equation (17) was fulfilled with $\epsilon = 10^{-8}$ for all the simulations.

$$\epsilon \geq \max_{x,y,z} \left(\frac{|\rho^t(x,y,z) - \rho^{t-1}(x,y,z)|}{\rho^{t-1}(x,y,z)} \right) \tag{17}$$

For the simulations, a high-performance computing code was adapted [36]. The code uses a hybrid CUDA–MPI programming layout that enables it to be executed on several

NVIDIA GPUs in parallel. In the D3Q27 LB method, the evolution of a 27–distribution function has to be calculated at each lattice node. This includes three major steps: collision, streaming, and force calculation. Since the method is explicit and all calculations are local, multithread parallelization within the GPU can be employed efficiently.

All 3D figures in this work were created using ParaView [37], and all 2D figures were created using the Python package Matplotlib.

4. Results

4.1. Theoretical Analysis of the Constant Mean Curvature Surface for a Combined Pillar–Pore Structure

With Equation (10) and the the divergence in cylindrical coordinates (Equation (5)), the Young–Laplace equation can be expressed in cylindrical coordinates. The origin of the coordinate system is set in the centre of the pillar. In this work, we theoretically analysed the CMC problem only for the much simpler rotationally symmetric case. Therefore, the Young–Laplace equation simplifies to:

$$\operatorname{div} \hat{\mathbf{n}} = \frac{1}{r}\frac{\partial}{\partial r}\left(r\frac{\partial f(r)}{\partial r}\left(1+\left(\frac{\partial f(r)}{\partial r}\right)^2\right)^{-\frac{1}{2}}\right) = \frac{\Delta p}{\gamma} =: q \tag{18}$$

Rearranging and integration yields:

$$rf'(r)\left(1+f'(r)^2\right)^{-\frac{1}{2}} = \frac{1}{2}qr^2 + c_0 \qquad \text{with } c_0 \in \mathbb{R} \tag{19}$$

$$\Leftrightarrow rf'(r) = \left(\frac{1}{2}qr^2 + c_0\right)\left(1+f'(r)^2\right)^{\frac{1}{2}} \tag{20}$$

Finally, one can solve for $f'(r)$

$$f'_{+/-}(r) = \pm\sqrt{\frac{(0.5qr^2+c_0)^2}{r^2-(0.5qr^2+c_0)^2}} = \pm\frac{|0.5qr^2+c_0|}{\sqrt{r^2-(0.5qr^2+c_0)^2}} \tag{21}$$

and one finds two solutions for the original differential equation: $f'_-(r)$ represents a solution with negative slope and $f'_+(r)$ represents a solution with positive slope.

Assuming the extremum is at $r = R > r_p$, then $f'_{+/-}(r)|_{r=R} = 0$ provides the following expression for c_0:

$$c_0 = -0.5qR^2 \tag{22}$$

One can also derive a dimensionless form for $f'_{+/-}$:

$$f'_{+/-}\left(\frac{r}{R}, qR\right) = \pm\sqrt{\frac{\left(\left(\frac{r}{R}\right)^2-1\right)^2}{\frac{4}{(qR)^2}\left(\frac{r}{R}\right)^2-\left(\left(\frac{r}{R}\right)^2-1\right)^2}} \tag{23}$$

Solving Equation (21) for q gives:

$$q = \frac{2r\left|f'_{+/-}(r)\right|}{\sqrt{1+(f'_+(r))^2}|r^2-R^2|} > 0 \tag{24}$$

A geometrical expression for the slope of the function $f(r)$ in terms of α, the angle between the z-axis and $f(r)$, is given by Equation (25).

$$f'_{+/-}(r) = \pm\tan(\alpha - \frac{\pi}{2}) \qquad \text{with } \alpha \in [90°, 180°] \tag{25}$$

Solving Equation (21) for R, inserting Equation (25), and applying the trigonometric relation $\tan(x)/\sqrt{1+\tan^2(x)} = \sin(x)$, one can derive Equation (26).

$$R = \sqrt{r^2 - \frac{2rf'_{+/-}(r)}{q\sqrt{1+(f'_{+/-}(r))^2}}} = \sqrt{r^2 \pm \frac{2r\cos(\alpha)}{q}} \tag{26}$$

For a hydrophobic structure consisting of a cylindrical pore (radius r_c) with a pillar (radius r_p) in the centre (see Figures 3 and 4), the solution can be constructed with $f_-(r)$ for $r_p \leq r \leq R$ and $f_+(r)$ for $R < r \leq r_c$. To ensure continuity, $f'_-(r)|_{r=R} = f'_+(r)|_{r=R} = 0$ and $f_-(R) = f_+(R)$ have to be fulfilled; $f_-(r)$ and $f_+(r)$ both have their minimum at $r = R$ and share the same $c_0 = -0.5qR^2$. The expression for $f'(r)$ is then given by:

$$f'(r) = \frac{0.5qr^2 - 0.5qR^2}{\sqrt{r^2 - (0.5qr^2 - 0.5qR^2)^2}} \tag{27}$$

The integral of $f'(r)$ is an elliptic integral. The general form of an elliptic integral is given by the following equation according to [38]:

$$\int \frac{A(r)}{B(r)\sqrt{S(r)}}\mathrm{d}r \tag{28}$$

Here $A(r)$, $B(r)$ are polynomials in r and $S(r)$ is a polynomial of degree 3 or 4. For our case, it holds that $A(r) = 0.5qr^2 - 0.5qR^2$, $B(r) = 1$, and

$$S(r) = r^2 - (0.5qr^2 - 0.5qR^2)^2 \tag{29}$$

The roots of $S(r)$ are at $r_1 = (1+\sqrt{1+q^2R^2})/q$, $r_2 = (-1+\sqrt{1+q^2R^2})/q$, $r_3 = (1-\sqrt{1+q^2R^2})/q$, and $r_4 = (-1-\sqrt{1+q^2R^2})/q$ for $q \neq 0$.

The integral $\int f'(r)\mathrm{d}r$ has no expression in terms of elementary functions, since $S(r)$ has no repeated roots. With a reduction formula, every elliptic integral can be brought into a form that involves three elementary integrals (elliptic integrals of the first, second, and third kind) [38]. The software Mathematica [39] can calculate the reduction for our problem, and one finds that the solution depends on the elliptic integrals of the first and second kind. Nevertheless, the expression for $f'(r)$ can be used to derive some interesting properties. By a simple numerical integration, $f(r)$ can be determined:

$$f(r) = \int_{r_p}^{r} f'(\tilde{r})\mathrm{d}\tilde{r} + z_p = I(r) + z_p \tag{30}$$

An interesting family of solutions are those with identical contact angles at $r_p < R$ and $r_* > R$. This condition can be expressed by the following equation:

$$|f'(r)|_{r=r_p}| = |f'(r)|_{r=r_*}| \tag{31}$$

Solving for c_0 leads to

$$c_0 = -0.5qr_pr_* \tag{32}$$

Combining Equations (22) and (32) yields the following expression for the minimum's location:

$$R = \sqrt{r_pr_*} \tag{33}$$

This shows that the minimum's location for this specific case is independent of the contact angle.

Let α_p and α_c be the respective contact angles between the liquid and the pillar/pore wall. Combining Equation (26), evaluated at $r = r_p$, and Equation (33) gives:

$$R = \sqrt{r_p r_*} = \sqrt{r_p^2 - \frac{2r_p \cos(\alpha_p)}{q}} \tag{34}$$

$$\Rightarrow r_* = r_p - \frac{2\cos(\alpha_p)}{q} \tag{35}$$

Equipped with this solution, we can now derive an expression for the critical (liquid entry) pressure of a combined pillar–pore structure. For $q = 0$, the liquid–gas interface is flat. With increasing pressure, a torus-like meniscus starts to form (see Figure 3). The contact angles between liquid and pillar wall (α_p) and liquid and pore wall (α_c) begin to increase. In the beginning, water touches neither the pillar's lateral surface nor the pore wall. If the liquid does not wet the pillar and the pore wall it holds $|f'_+(r)|_{r=r_c}| < |f'_-(r)|_{r=r_p}|$, it follows that $\alpha_c < \alpha_p$. For a certain q_1, the equilibrium contact angle is reached at the pillar ($\alpha_p = \alpha_0$); the contact angle at the pore wall is, for this state, still smaller than the equilibrium contact angle ($\alpha_c < \alpha_0$). This state is plotted in Figure 4a; r_* is marked only as an aid line for visualisation purposes but is not part of the actual solution.

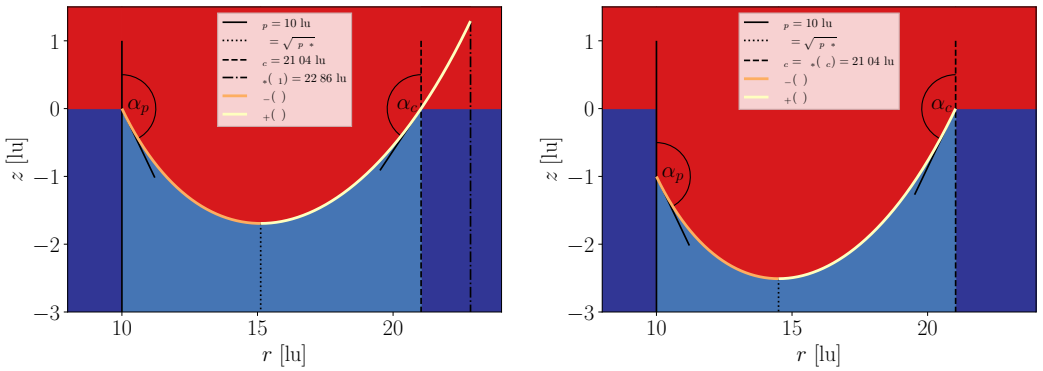

(**a**) (**b**)

Figure 4. Sketch of an intrusion of liquid into the pillar–pore structure. Solid is shown in dark blue, liquid in red, and gas in light blue, and the equilibrium contact angle is at $\alpha_0 = 130°$. Subfigure (**a**) shows a situation for $q_1 = 0.10\,\mathrm{lu}^{-1}$, $\alpha_p = 130°$, and $\alpha_c < 130°$; r_* is solely marked as an aid line for visualisation purposes but is not part of the actual solution. Subfigure (**b**) shows the situation right before the break through with $q_{crit} = 0.12\,\mathrm{lu}^{-1}$, $\alpha_p = 130°$, $\alpha_c = 130°$, and $r_* = r_c$; $f_-(r)$ and $f_+(r)$ form the liquid–gas interface. R is the location of the minimum, r_p is the pillar radius, and r_c is the pore radius.

As the pressure increases further and q exceeds q_1, liquid begins to slide down the pillar wall. As long as $\alpha_c < \alpha_0$, no water will wet the pore wall. While the liquid contact point at the pillar wall slides down, the contact angle at the pore wall increases and R shifts towards r_p. This process continues until the contact angle at the pore wall reaches the equilibrium contact angle ($\alpha_c = \alpha_p = \alpha_0$). At this point, $r_* = r_c$ (see Figure 4b), which, inserted in Equation (35), yields:

$$q_{crit} = \frac{-2\cos(\alpha_0)}{r_c - r_p} \tag{36}$$

In this critical state, a complete breakthrough occurs and the LEP (q_{crit}) is reached. Expressed in terms of Δp_{crit} and γ, one gets:

$$\Delta p_{crit} = \frac{-2\gamma \cos(\alpha_0)}{r_c - r_p} \tag{37}$$

The location of the minimum in the critical state is

$$R_{crit} = \sqrt{r_p r_c} \tag{38}$$

For $q \geq 2/(r_c - r_p)$, water will always intrude into the pillar–pore structure, independent of the hydrophobicity of the solid. In the limit of $r_p = 0$, we find the well-known equation for the LEP of a cylindrical pore (see Equation (2)).

Using the force-balance approach of Zheng et al. [19], one can directly derive the expression of the LEP, but without gaining any information about the shape of the liquid–gas interface.

$$F_z = \Delta p_{crit} \underbrace{(\pi r_c^2 - \pi r_p^2)}_{\substack{\text{cross sectional} \\ \text{area of pillar–} \\ \text{pore structure}}} + \gamma \underbrace{(2\pi r_p + 2\pi r_c)}_{\substack{\text{three-phase} \\ \text{contact line} \\ \text{length}}} \underbrace{\cos(\alpha_0)}_{\substack{\text{projection} \\ \text{along } z\text{-axis}}} = 0 \tag{39}$$

With the third binomial formula, one gets the following:

$$\Delta p_{crit} \pi (r_c - r_p)(r_c + r_p) = -2\gamma\pi \cos(\alpha_0)(r_p + r_c) \tag{40}$$

Simplification leads again to Equation (37).

One can also generalise this for the case where the pillar and the pore material have different equilibrium contact angles, α_0^p and α_0^c, respectively. In the critical state, it holds that at location r_p, $\alpha = \alpha_0^p$, and at location r_c, $\alpha = \alpha_0^c$. Combining these two conditions with Equation (26) gives:

$$\begin{aligned} R_{crit}^2 &= r_p^2 + \frac{2 r_p \cos(\alpha_0^p)}{q_{crit}} \\ &= r_c^2 - \frac{2 r_c \cos(\alpha_0^c)}{q_{crit}} \end{aligned} \tag{41}$$

Solving Equation (41) for q_{crit}, one can derive a generalised expression for the LEP of the pillar–pore structure:

$$q_{crit} = -2 \frac{r_p \cos(\alpha_0^p) + r_c \cos(\alpha_0^c)}{r_c^2 - r_p^2} \tag{42}$$

Inserting Equation (42) into Equation (26) with $r = r_p$ and $\alpha = \alpha_0^p$, one can derive a generalised form for R in the critical state.

$$\begin{aligned} R_{crit} &= \sqrt{r_p^2 + \frac{r_p \cos(\alpha_0^p)(r_c^2 - r_p^2)}{r_p \cos(\alpha_0^p) + r_c \cos(\alpha_0^c)}} \\ &= \sqrt{\frac{r_p r_c (r_c \cos(\alpha_0^p) + r_p \cos(\alpha_0^c))}{r_p \cos(\alpha_0^p) + r_c \cos(\alpha_0^c)}} \end{aligned} \tag{43}$$

The location of the minimum in the critical state depends on the two equilibrium contact angles. For the special case $\alpha_0^p = \alpha_0^c = \alpha_0$, the cosines cancel out and one finds again Equation (38). Combining R_{crit} and q_{crit} gives:

$$c_{0,crit} = -0.5 q_{crit} R_{crit}^2 = \frac{r_p r_c (r_c \cos(\alpha_0^p) + r_p \cos(\alpha_0^c))}{r_c^2 - r_p^2} \tag{44}$$

4.2. Numerical Calculation of the Constant Mean Curvature Surface and the Liquid Entry Pressure with the Lattice Boltzmann Method

4.2.1. Single Circular Pillar with Periodic Boundary Conditions

As a validation benchmark, we simulated a single pillar with periodic boundary conditions in the x- and y-directions and a closed boundary in the z-direction. At $z = 0$ lu, the domain boundary was closed with a slice of solid voxels, as well as on the opposite side of the domain at $z = 149$ lu. The total domain size was $200 \times 200 \times 150$ lu^3 (see Figure 5). These boundary conditions mimic a domain with periodically repeated pillars, as shown in Figure 2. The domain was initialized partly with water density and partly with gas density. Initially, the water was already surrounding part of the pillar and filled the entire upper part above the pillar. The simulation was then run until a static equilibrium state was reached. For the equilibrium state, the contact angle around the pillar was equal to the equilibrium contact angle and therefore the pressure difference between liquid and gas corresponded to the critical pressure calculated with Equation (3) from Zheng et al. [19].

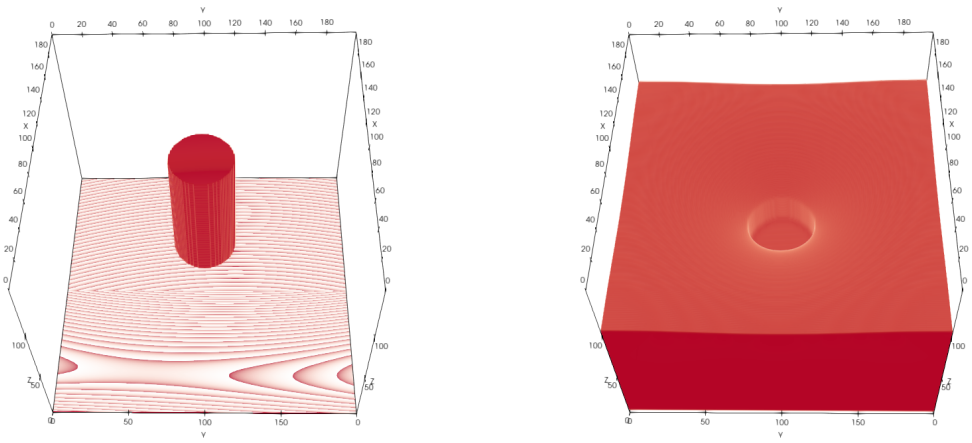

(**a**) (**b**)

Figure 5. (**a**) Solid domain structure with a single round pillar with PBC in x- and y-directions and a closed boundary in z-direction. At $z = 0$ lu, the domain boundary was closed with a slice of solid voxels, as well as on the other side of the domain at $z = 149$ lu. Boundary at $z = 149$ lu is not shown for better visibility. (**b**) Example of the density field after convergence of the multiphase LB simulation. Equilibrium state of the liquid (in red) for $r_p = 20$ lu and $\alpha_0 = 156.61°$. Gas and solid are not shown for better visibility.

As can be seen in Figure 6, we found that our LB simulations produced results which were in good agreement with the predictions from Equation (45) from Zheng et al. [19].

$$q_{crit}^{Zheng} = \frac{\Delta p_{crit}}{\gamma} = -\frac{2\pi r_p \cos(\alpha_0)}{P^2 - \pi r_p^2} \tag{45}$$

The value of q_{crit} from the LB simulation in Figure 6 was calculated with the equation of state (15) and $q_{crit} = (\overline{p(\rho_l)} - \overline{p(\rho_g)})/\gamma$. Here ρ_l is the density field of the liquid phase and ρ_g is the density field of the gas phase from the LB simulations; $\overline{p(\rho_l)}$ and $\overline{p(\rho_g)}$ represent the mean values of the liquid and gas pressure fields, respectively. This pressure

variation across the same phase emerges from the spurious velocities at the interface typical for this class of models. To reduce this effect, pressure values close to the interface were omitted. For more information on spurious currents, see Section 5. The errors for q_{crit} in Figure 6 are based on the standard deviation of the pressure field within each phase.

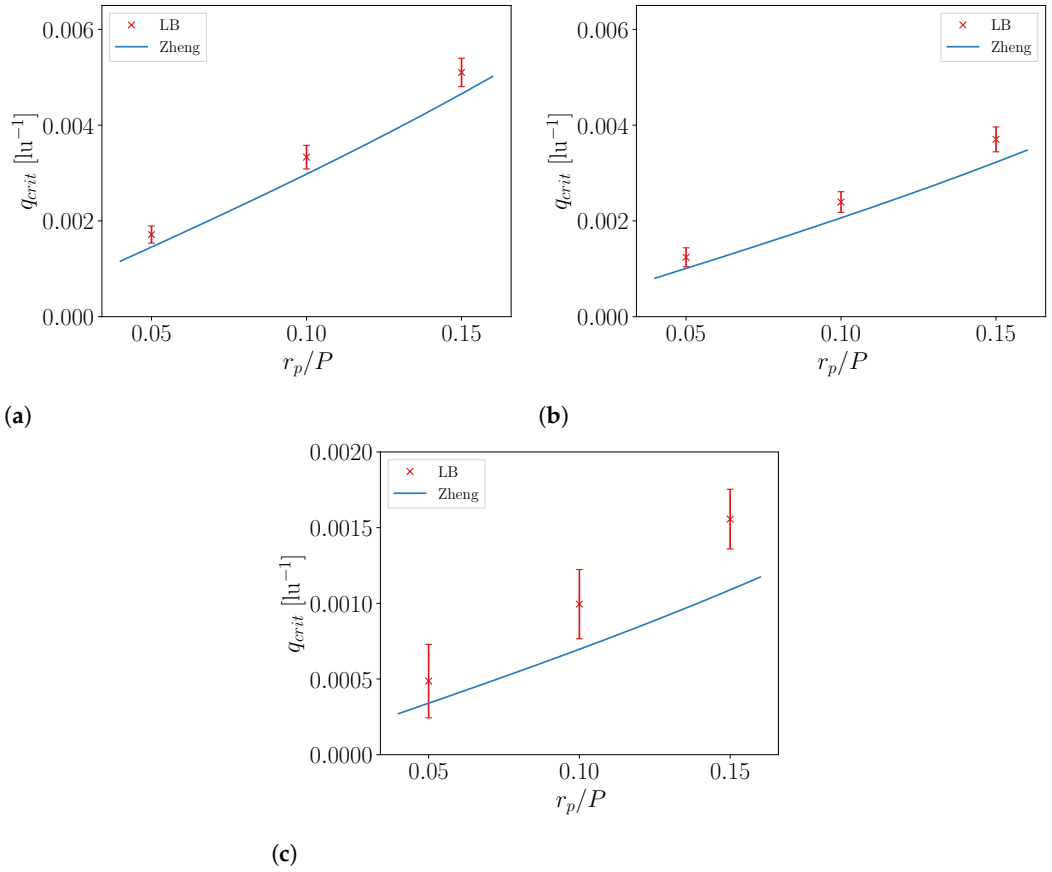

Figure 6. Values of q_{crit} for three different equilibrium contact angles and three different r_p values with $P = 200$ lu. Comparison between the LB results and Equation (45) from Zheng et al. [19]. In (**a**), $\alpha_0 = 156.61°$; in (**b**), $\alpha_0 = 129.51°$, and in (**c**), $\alpha_0 = 102.40°$.

4.2.2. Combined Pillar–Pore Structure

To validate our findings in Section 4.1, we ran 3D LB simulations. The upper boundary of the domain at $z = 0$ lu as well as the lower boundary at $z = 149$ lu were closed with a slice of solid voxels. In the centre we placed a cylindrical pore with radius $r_c = 99$ lu and a cylindrical pillar with radius $r_p = 20$ lu. The heights of the pillar and the pore were $h = 90$ lu. Above and below the pillar–pore structure was void space (see Figure 7). The total domain size was $200 \times 200 \times 150$ lu^3. For the simulations, the pillar and pore material had identical surface properties and therefore had the same equilibrium contact angle.

The domain was initialized partly with water density and partly with gas density. Initially, the water already filled part of the pillar–pore space and the entire upper part above the pillar–pore structure. The simulation was then run until a static equilibrium state was reached.

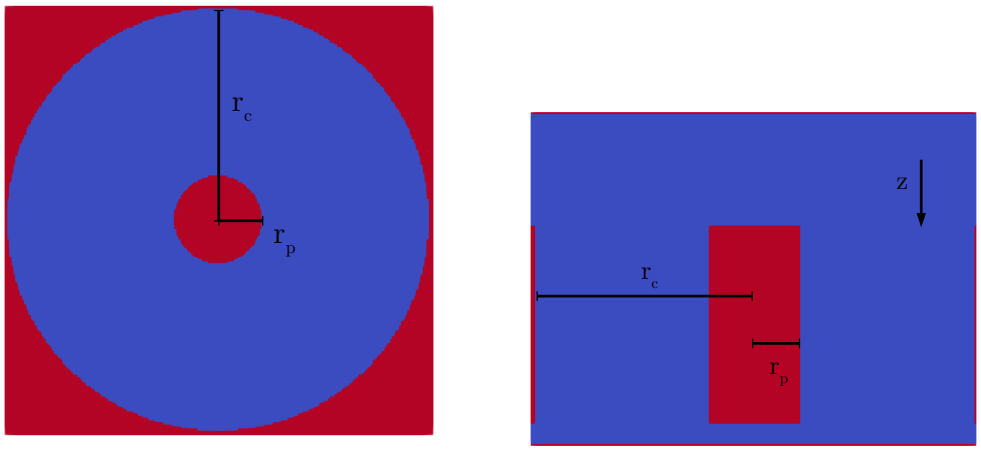

(**a**) (**b**)

Figure 7. Geometry of the combined pillar–pore structure: (**a**) top view and (**b**) side view. Solid is in red and void space in blue.

In an equilibrium state, the contact angles at the pillar wall and the pore wall will reach the equilibrium contact angle α_0. This is analogous to a droplet on a flat surface, for which the contact angle also becomes the equilibrium contact angle α_0 for the static state. The pressure difference will exactly be the critical pressure difference predicted by Equation (36) (see Figure 8).

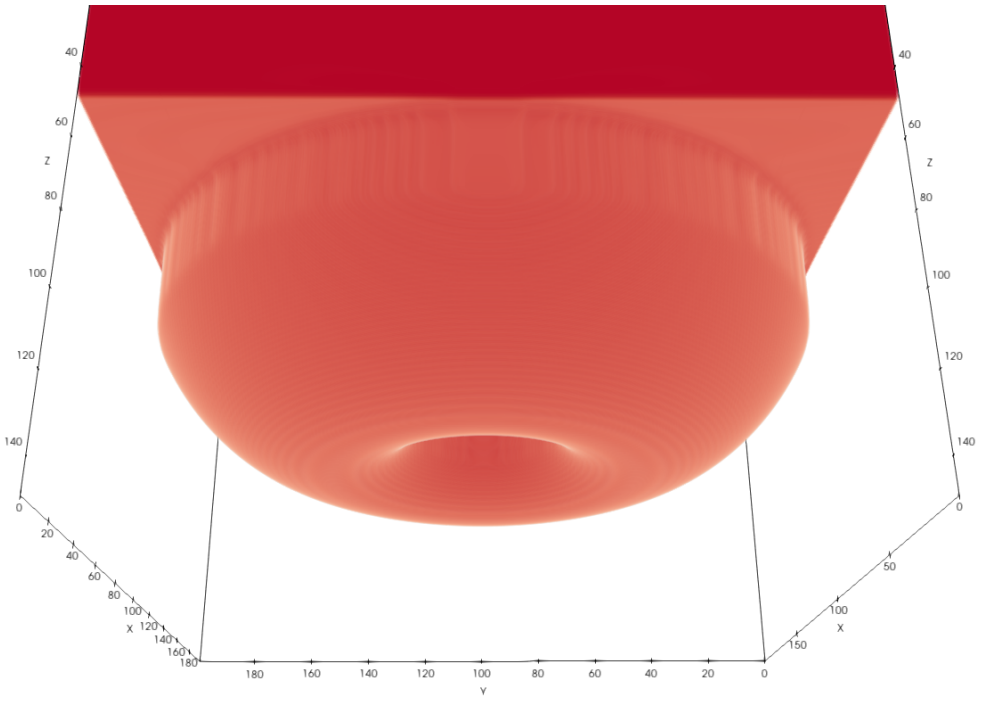

Figure 8. Liquid–gas interface within a combined pillar–pore structure. Example of the density field after convergence of the multiphase LB simulation for $\alpha_0 = 156.61°$, $r_p = 20$ lu, $r_c = 99$ lu, and a domain size of $200 \times 200 \times 150$ lu^3. Liquid is in red; gas and solid are not shown for better visibility.

Based on α_0, pill radius $r_p = 20$ lu, and pore radius $r_* = r_c = 99$ lu, we used Equation (36) to compute q_{crit} analytically and compared it to the LB simulation results (see Table 1); q_{crit}^{LB} from the LB simulation was again calculated with $q_{crit} = (\overline{p(\rho_l)} - \overline{p(\rho_g)})/\gamma$. The results are displayed in Table 1.

Table 1. Comparison between the LB simulation results and Equation (36). Respective q_{crit} values for $r_p = 20$ lu, $r_c = 99$ lu, and three different equilibrium contact angles. The error in parentheses was calculated based on the standard deviation of the pressure field within each phase. The last row shows the absolute deviation between LB simulation and theory.

G_{ads}	-80.0	-180.0	-280.0
α_0 (°)	156.61	129.51	102.40
q_{crit}^{LB} (lu^{-1})	0.02461	0.01781	0.00762
	(0.00042)	(0.00047)	(0.00035)
Equation (36) q_{crit} (lu^{-1})	0.02324	0.01610	0.00544
deviation (lu^{-1})	0.00137	0.00171	0.00218

To compare the shape of the interfaces with the LB simulation results, we numerically integrated Equation (27) with $c_0 = -0.5qr_pr_c$ and $q = q_{crit}^{LB}$ to obtain $f(r)$. These results are plotted together with the LB simulation results in Figure 9. For the numerical integration, we used the cumulative trapezoid method from the python3 package scipy (version 1.9.1) [40] with 1×10^4 points.

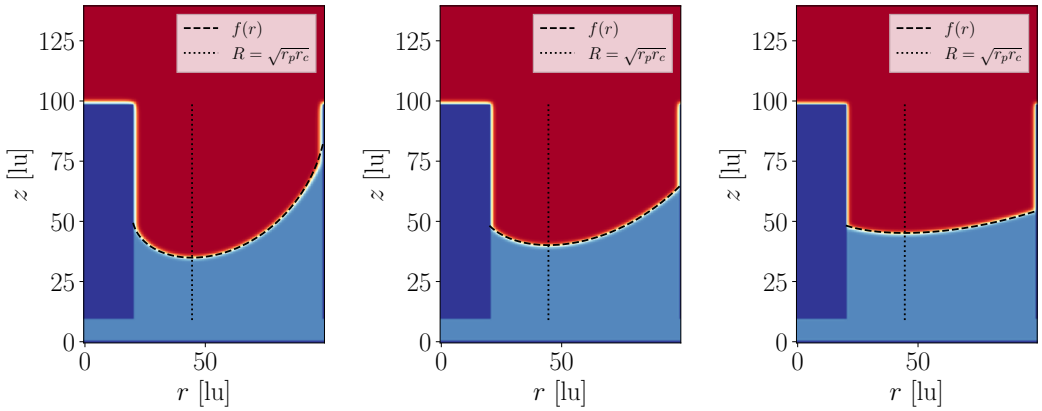

(**a**) (**b**) (**c**)

Figure 9. Shape of the liquid–gas interface for three different equilibrium contact angles. For a pillar radius of $r_p = 20$ lu and a pore radius of $r_c = 99$ lu. Cross-sections through $x = 99$ lu of the 3D density field from the multiphase LB simulation. The liquid is visualized in red, the gas in light blue, and the solid in dark blue; $f(r)$ shows the results based on the integral of Equation (27). In (**a**), $\alpha_0 = 156.61°$, in (**b**), $\alpha_0 = 129.51°$, and in (**c**), $\alpha_0 = 102.40°$.

To quantify the difference in the interface shape between the LB simulation and $f(r)$ from Equation (30), we calculated the normalised root mean square deviation (NRMSD) given in Equation (46). The lattice points right next to the solid walls were omitted because the boundary condition disturbs the density field close to the walls.

$$\mathrm{NRMSD} = \frac{100\,\%}{z_{max} - z_{min}} \times \sqrt{\frac{\sum_{j=r_p+2}^{r_c-2} [z_{IF,LB}(j) - f(j)]^2}{r_c - r_p - 3}} \tag{46}$$

First, we extracted the location of the liquid–gas interface (IF) from the LB simulation results. Based on the two-dimensional slice of the density field ($\rho_{j,k}$) shown in Figure 9 and the linear interpolation given in Equation (47), we were able to calculate the z positions of the liquid–gas interface from the LB simulations ($z_{IF,LB}$).

$$z_{IF,LB}(j) = k + \frac{\rho_c - \rho_{j,k}}{\rho_{j,k+1} - \rho_{j,k}} \qquad \text{with} \qquad \rho_{j,k} < \rho_c < \rho_{j,k+1} \tag{47}$$

Here $\rho_c = 0.5 \times (\rho_l + \rho_g)$ describes a critical density that defines the liquid–gas interface, $j \in [0, 1, \ldots, 99]$ is the position on the lattice in the r-direction, and $k \in [0, 1, \ldots, 149]$ is the position on the lattice in the z-direction.

$$z_p = \frac{\sum_{j=r_p+2}^{r_c-2} [z_{IF,LB}(j) - I(j)]}{r_c - r_p - 3} \tag{48}$$

The integral $I(r)$ in Equation (30) can be solved numerically, but $z_p = f(r_p)$ must also be determinant. To compute z_p, we used Equation (48), which minimizes the NRMSD in Equation (46). The results are shown in Figure 10.

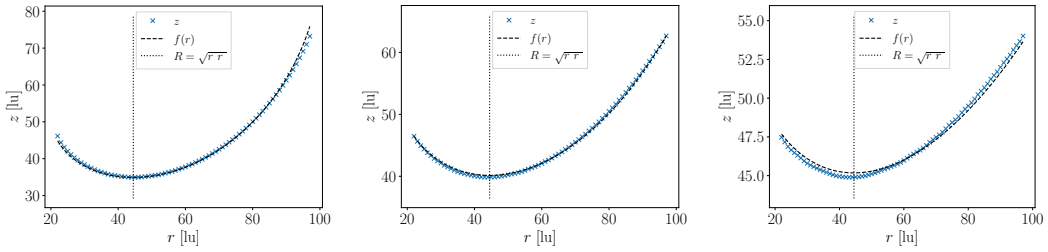

(**a**) (**b**) (**c**)

Figure 10. Shape of the liquid–gas interface for three different equilibrium contact angles: $f(r)$ shows the results based on the integral of Equation (27), and $z_{IF,LB}$ is the position of the interface predicted by the LB simulation. In (**a**), $\alpha_0 = 156.61°$, NRMSD = 1.53 %; in (**b**), $\alpha_0 = 129.51°$, NRMSD = 0.98 %, and in (**c**), $\alpha_0 = 102.40°$, NRMSD = 2.76 %.

5. Discussion

In this paper, we have derived an analytical expression for the liquid entry pressure of a combined pillar–pore structure and found good agreement with the predictions of the LB method. In all cases, the predictions for q_{crit} by the LB simulations were larger than the values predicted by the analytical analysis (see Table 1 and Figure 6). The largest deviation for q_{crit} was found for the smallest equilibrium contact angle ($\alpha_0 = 102.40°$; see Table 1). We identified three main sources of error. One error originates from the numerical limitations of the multiphase LB simulation, which was estimated by the standard deviation of the pressure field within each phase. This error in the pressure field originates from the spurious currents close to the interface that are typical for pseudo potential multiphase models [41]. This error could be minimized by an improved LB multiphase model and/or a higher resolution, which increases the computational cost of the simulation. Possible improvements are multi relaxation time [42] or entropic [43] LB models. A detailed discussion of contact angles in the pseudo-potential lattice Boltzmann modelling can be found in [17]. Changing model parameters such as the G parameter could also lead to smaller spurious currents and reduce the perturbation in the pressure field. However, this can only partially explain the deviation between the values of q_{crit} reported in Table 1. Other sources of error are the equilibrium contact angle calculations and the surface tension calculations based on benchmarks to calibrate the model. These systematic errors explain why we found consistently higher values in Table 1 and Figure 6 for the LB results compared to the theory. Moreover, the $\cos(\alpha_0)$ dependence of q_{crit} (see, e.g., Equation (36)) explains why the biggest error was found for the smallest equilibrium contact angle in Table 1. The equilibrium contact angle calculation can have an uncertainty of several degrees, and for values close to 90°, this error is amplified much more since the cosine has its largest derivative at 90°. Error propagation gives $\Delta q_{crit} = |2\sin(\alpha_0)/(r_c - r_p)|\Delta\alpha_0$. For more information on the equilibrium contact angle and surface tension calculations for the LB simulation results, see [18]. The shape of the interface and the location of the minimum calculated with Equations (30) and (38), respectively, agree very well with the predictions of the LB simulation. The NRMSD of the interface shape lies, for all three test cases, below

3 %, where the largest deviation was found, again, for the smallest equilibrium contact angle (See Figures 9 and 10).

In this paper, we only considered the case for which the cylindrical pore and the pillar have the same height. However, the reasoning in Section 4.1 can be applied in a similar way to a structure for which the pillar height exceeds or falls below that of the pore height, so that Equation (42) is universally applicable to any hydrophobic rotationally symmetric pillar–pore structure. Moreover the presented pillar–pore structure case can serve as a benchmark for the development and validation of numerical multiphase models.

Author Contributions: Conceptualization, T.J.; methodology, T.J., N.I.P. and S.L.; software, T.J. and N.I.P.; validation, T.J., J.K., N.I.P. and S.L.; formal analysis, T.J.; investigation, T.J., J.K., N.I.P. and S.L.; resources, N.I.P. and S.L.; data curation, T.J.; writing—original draft preparation, T.J.; writing—review and editing, T.J., J.K., N.I.P. and S.L.; visualization, T.J. and J.K.; supervision, N.I.P. and S.L.; project administration, T.J., N.I.P. and S.L.; funding acquisition, N.I.P. and S.L. All authors have read and agreed to the published version of the manuscript.

Funding: University of Luxembourg, Paul Scherrer Institute.

Informed Consent Statement: Not applicable.

Data Availability Statement: Simulation results from Section 4.2 are available at the following links: https://doi.org/10.6084/m9.figshare.22574173, https://doi.org/10.6084/m9.figshare.22574176.

Acknowledgments: We are thankful for the many fruitful discussions with Filip Janasz. The calculations in this paper were carried out using the HPC facilities of the University of Luxembourg [44] (see `hpc.uni.lu`) and the Swiss Supercomputing Center CSCS (project s1155). We also thank the University of Luxembourg and SwissNuclear for their support.

Conflicts of Interest: The authors declare no conflicts of interest.

Abbreviations

CMC	Constant mean curvature
PDE	Partial differential equation
Δp_{crit}	Liquid entry pressure (LEP)
γ	Surface tension
q	$\Delta p/\gamma$
r_p	Pillar radius
r_c	Pore radius
R	Location of the minimum
α_p	Contact angles between the liquid and the pillar wall
α_c	Contact angles between the liquid and the pore wall
α_0	Equilibrium contact angle between liquid and solid
P	Pitch pillar (periodicity in x- and y-directions)
A_c	Area of the periodically repeated cell ($A_c = P \times P$)
A	Top area of the pillar ($A = \pi r_p^2$)
l	Perimeter of the pillar ($l = 2\pi r_p$)
$\hat{\mathbf{n}}$	Unit normal vector of the liquid–gas interface
LB	lattice Boltzmann
NRMSD	normalised root mean square deviation
p	Pressure
ρ	Density
ρ_l	Liquid density
ρ_g	Gas density
$\mathbf{F}$	Force
Δx	Lattice spacing
Δt	Time step
m	Fluid particle mass

G_{ads}	LB parameter to tune the equilibrium contact angle
G	LB parameter to control the fluid–fluid interaction strength
τ	Relaxation time
ν	Kinematic viscosity
c_s	Speed of sound
g	Gravitation acceleration
$\mathbf{v}$	Velocity
$\mathbf{c_i}$	Discrete lattice velocity

References

1. Jung, Y.; Bhushan, B. Wetting behaviour during evaporation and condensation of water microdroplets on superhydrophobic patterned surfaces. *J. Microsc.* **2008**, *229*, 127–140. [CrossRef] [PubMed]
2. Gogolides, E.; Ellinas, K.; Tserepi, A. Hierarchical micro and nano structured, hydrophilic, superhydrophobic and superoleophobic surfaces incorporated in microfluidics, microarrays and lab on chip microsystems. *Microelectron. Eng.* **2015**, *132*, 135–155. [CrossRef]
3. Xiao, Z.; Zheng, R.; Liu, Y.; He, H.; Yuan, X.; Ji, Y.; Li, D.; Yin, H.; Zhang, Y.; Li, X.M.; et al. Slippery for scaling resistance in membrane distillation: A novel porous micropillared superhydrophobic surface. *Water Res.* **2019**, *155*, 152–161. [CrossRef] [PubMed]
4. Agonafer, D.D.; Lee, H.; Vasquez, P.A.; Won, Y.; Jung, K.W.; Lingamneni, S.; Ma, B.; Shan, L.; Shuai, S.; Du, Z.; et al. Porous micropillar structures for retaining low surface tension liquids. *J. Colloid Interface Sci.* **2018**, *514*, 316–327. [CrossRef]
5. Yao, X.; Gao, J.; Song, Y.; Jiang, L. Superoleophobic Surfaces with Controllable Oil Adhesion and Their Application in Oil Transportation. *Adv. Funct. Mater.* **2011**, *21*, 4270–4276. [CrossRef]
6. Xue, Z.; Wang, S.; Lin, L.; Chen, L.; Liu, M.; Feng, L.; Jiang, L. A Novel Superhydrophilic and Underwater Superoleophobic Hydrogel-Coated Mesh for Oil/Water Separation. *Adv. Mater.* **2011**, *23*, 4270–4273. [CrossRef] [PubMed]
7. Field, R.W. Separation by reconfiguration. *Nature* **2012**, *489*, 41–42. [CrossRef]
8. Sridhar, A.; Ong, C.L.; Paredes, S.; MicheL, B. Thermal Design of a Hierarchical Radially Expanding Cavity for Two-Phase Cooling of Integrated Circuits. In Proceedings of the International Electronic Packaging Technical Conference and Exhibition, Changsha, China, 11–14 August 2015; Volume 1. [CrossRef]
9. Kim, B.S.; Harriott, P. Critical entry pressure for liquids in hydrophobic membranes. *J. Colloid Interface Sci.* **1987**, *115*, 1–8. [CrossRef]
10. Rahimpour, M.R.; Esmaeilbeig, M.A. Chapter 6—Membrane Wetting in Membrane Distillation. In *Current Trends and Future Developments on (Bio-) Membranes*; Basile, A., Curcio, E., Inamuddin, Eds.; Elsevier: Amsterdam, The Netherlands, 2019; pp. 143–174. [CrossRef]
11. Lobaton, E.; Salamon, T. Computation of constant mean curvature surfaces: Application to the gas–liquid interface of a pressurized fluid on a superhydrophobic surface. *J. Colloid Interface Sci.* **2007**, *314*, 184–198. [CrossRef]
12. Laplace, P.S. Supplément au dixième livre du Traité de Mécanique Céleste. *J.B.M. Duprat* **1805**, *4*, 1–79.
13. Racz, G.; Kerker, S.; Kovács, Z.; Vatai, G.; Ebrahimi, M.; Czermak, P. Theoretical and Experimental Approaches of Liquid Entry Pressure Determination in Membrane Distillation Processes. *Period. Polytech. Chem. Eng.* **2014**, *58*, 81–91. [CrossRef]
14. Young, T. III. An essay on the cohesion of fluids. *Philos. Trans. R. Soc. Lond.* **1805**, *95*, 65–87. [CrossRef]
15. Kwok, D.; Neumann, A. Contact angle measurement and contact angle interpretation. *Adv. Colloid Interface Sci.* **1999**, *81*, 167–249. [CrossRef]
16. Ruiz-Cabello, F.J.M.; Rodríguez-Valverde, M.A.; Marmur, A.; Cabrerizo-Vílchez, M.A. Comparison of Sessile Drop and Captive Bubble Methods on Rough Homogeneous Surfaces: A Numerical Study. *Langmuir* **2011**, *27*, 9638–9643. [CrossRef] [PubMed]
17. Li, Q.; Luo, K.H.; Kang, Q.J.; Chen, Q. Contact angles in the pseudopotential lattice Boltzmann modeling of wetting. *Phys. Rev. E Stat. Nonlin. Soft Matter. Phys.* **2014**, *90*, 053301. [CrossRef] [PubMed]
18. Jäger, T.; Mokos, A.; Prasianakis, N.I.; Leyer, S. Pore-Level Multiphase Simulations of Realistic Distillation Membranes for Water Desalination. *Membranes* **2022**, *12*, 1112. [CrossRef]
19. Zheng, Q.S.; Yu, Y.; Zhao, Z.H. Effects of hydraulic pressure on the stability and transition of wetting modes of superhydrophobic surfaces. *Langmuir* **2005**, *21*, 12207–12212. [CrossRef]
20. Schiller, U.D.; Krüger, T.; Henrich, O. Mesoscopic modelling and simulation of soft matter. *Soft Matter* **2018**, *14*, 9–26. [CrossRef]
21. Xiong, W.; Cheng, P. Mesoscale simulation of a molten droplet impacting and solidifying on a cold rough substrate. *Int. Commun. Heat Mass Transf.* **2018**, *98*, 248–257. [CrossRef]
22. Prasianakis, N.I.; Rosén, T.; Kang, J.; Eller, J.; Mantzaras, J.; Büichi, F.N. Simulation of 3D Porous Media Flows with Application to Polymer Electrolyte Fuel Cells. *Commun. Comput. Phys.* **2013**, *13*, 851–866. [CrossRef]
23. Rosen, T.; Eller, J.; Kang, J.; Prasianakis, N.I.; Mantzaras, J.; Büchi, F.N. Saturation dependent effective transport properties of PEFC gas diffusion layers. *J. Electrochem. Soc.* **2012**, *159*, F536. [CrossRef]
24. Luo, K.; Xia, J.; Monaco, E. Multiscale modelling of multiphase flow with complex interactions. *J. Multiscale Model.* **2009**, *1*, 125–156. [CrossRef]

25. Qin, F.; Del Carro, L.; Mazloomi Moqaddam, A.; Kang, Q.; Brunschwiler, T.; Derome, D.; Carmeliet, J. Study of non-isothermal liquid evaporation in synthetic micro-pore structures with hybrid lattice Boltzmann model. *J. Fluid Mech.* **2019**, *866*, 33–60. [CrossRef]
26. Afra, B.; Amiri Delouei, A.; Mostafavi, M.; Tarokh, A. Fluid-structure interaction for the flexible filament's propulsion hanging in the free stream. *J. Mol. Liq.* **2021**, *323*, 114941. [CrossRef]
27. Afra, B.; Karimnejad, S.; Amiri Delouei, A.; Tarokh, A. Flow control of two tandem cylinders by a highly flexible filament: Lattice spring IB-LBM. *Ocean Eng.* **2022**, *250*, 111025. [CrossRef]
28. Prasianakis, N.I.; Karlin, I.V.; Mantzaras, J.; Boulouchos, K.B. Lattice Boltzmann method with restored Galilean invariance. *Phys. Rev. E* **2009**, *79*, 066702. [CrossRef]
29. Qian, Y.H.; D'Humières, D.; Lallemand, P. Lattice BGK Models for Navier-Stokes Equation. *Europhys. Lett. (EPL)* **1992**, *17*, 479–484. [CrossRef]
30. Peng, C.; Tian, S.; Li, G.; Sukop, M.C. Single-component multiphase lattice Boltzmann simulation of free bubble and crevice heterogeneous cavitation nucleation. *Phys. Rev. E* **2018**, *98*, 023305. [CrossRef]
31. Kunes, J. *Dimensionless Physical Quantities in Science and Engineering*; Elsevier Scientific Pub. Co.: Amsterdam, The Netherlands; New York, NY, USA, 2012.
32. Safi, M.A.; Mantzaras, J.; Prasianakis, N.I.; Lamibrac, A.; Büchi, F.N. A pore-level direct numerical investigation of water evaporation characteristics under air and hydrogen in the gas diffusion layers of polymer electrolyte fuel cells. *Int. J. Heat Mass Transf.* **2019**, *129*, 1250–1262. [CrossRef]
33. Shan, X.; Chen, H. Lattice Boltzmann model for simulating flows with multiple phases and components. *Phys. Rev. E* **1993**, *47*, 1815–1819. [CrossRef]
34. Shan, X.; Chen, H. Simulation of nonideal gases and liquid-gas phase transitions by the lattice Boltzmann equation. *Phys. Rev. E* **1994**, *49*, 2941. [CrossRef] [PubMed]
35. Sukop, M.C.; Thorne, D.T. *Lattice Boltzmann Modeling*; Springer: Berlin/Heidelberg, Germany, 2006.
36. Safi, M.A.; Prasianakis, N.I.; Mantzaras, J.; Lamibrac, A.; Büchi, F.N. Experimental and pore-level numerical investigation of water evaporation in gas diffusion layers of polymer electrolyte fuel cells. *Int. J. Heat Mass Transf.* **2017**, *115*, 238–249. [CrossRef]
37. Ahrens, J.; Geveci, B.; Law, C. ParaView: An End-User Tool for Large Data Visualization. In *Visualization Handbook*; Elesvier: Amsterdam, The Netherlands, 2005; ISBN 978-0123875822.
38. Weisstein, E.W. Elliptic Integral. From MathWorld—A Wolfram Web Resource. 2023. Available online: https://mathworld.wolfram.com/EllipticIntegral.html (accessed on 9 March 2023).
39. Wolfram Inc. *Mathematica, Version 13.2*; Wolfram Inc.: Champaign, IL, USA, 2022.
40. Virtanen, P.; Gommers, R.; Oliphant, T.E.; Haberland, M.; Reddy, T.; Cournapeau, D.; Burovski, E.; Peterson, P.; Weckesser, W.; Bright, J.; et al. SciPy 1.0: Fundamental Algorithms for Scientific Computing in Python. *Nat. Methods* **2020**, *17*, 261–272. [CrossRef]
41. Chen, L.; Kang, Q.; Mu, Y.; He, Y.L.; Tao, W.Q. A critical review of the pseudopotential multiphase lattice Boltzmann model: Methods and applications. *Int. J. Heat Mass Transf.* **2014**, *76*, 210–236. [CrossRef]
42. Peng, H.; Zhang, J.; He, X.; Wang, Y. Thermal pseudo-potential lattice Boltzmann method for simulating cavitation bubbles collapse near a rigid boundary. *Comput. Fluids* **2021**, *217*, 104817. [CrossRef]
43. Mazloomi M., A.; Chikatamarla, S.S.; Karlin, I.V. Entropic lattice Boltzmann method for multiphase flows: Fluid-solid interfaces. *Phys. Rev. E* **2015**, *92*, 023308. [CrossRef] [PubMed]
44. Varrette, S.; Cartiaux, H.; Peter, S.; Kieffer, E.; Valette, T.; Olloh, A. Management of an Academic HPC & Research Computing Facility: The ULHPC Experience 2.0. In Proceedings of the 6th ACM High Performance Computing and Cluster Technologies Conference (HPCCT 2022), Fuzhou, China, 8–10 July 2022; Association for Computing Machinery (ACM): Fuzhou, China, 2022.

5

VALIDATING THE TRANSITION CRITERIA FROM THE CASSIE–BAXTER TO THE WENZEL STATE FOR PERIODICALLY PILLARED SURFACES WITH LATTICE BOLTZMANN SIMULATIONS

First author publication in the peer reviewed journal ACS Omega. URL to the paper: https://pubs.acs.org/doi/10.1021/acsomega.3c08862. A detailed list of the author contribution can be found at the end of the paper.

Previous experiments by Xiao et al. [49] have shown that certain membrane structures, such as micropillars arranged in a periodic pattern and hydrophobic coatings, can mitigate scaling problems and prolong membrane lifetime. A possible explanation for this improvement is that the pillar structure prevents the water from wetting the membrane structure and remains in a state where it only touches the top of the pillars and air remains trapped between the pillars. Zheng, Yu, and Zhao [52] derived a formula for the critical pressure difference between a liquid film above the pillars and the trapped air at which a fully wetted state occurs. In the experimental study of these periodically pillared structures, droplets are often placed on top of the columns and the conditions under which the droplet remains in the elevated non–wetting (Cassie-Baxter) state are investigated. Patankar [30] derived a condition based on the Young–Laplace pressure difference due to the curvature of the droplet for which this transition occurs. These theoretical investigations allow to gain a better understanding on the wetting behavior of such pillar structures and are important for experimental investigations and could help to design even more scaling resistant membranes in the future.

In the work presented in this chapter, we continue our work from chapter 3. One of the benchmarks used to validate the Lattice Boltzmann multiphase model presented in 3 was to place liquid droplets on a rough hydrophobic surface created by pillars arranged in a periodic pattern. Jung and Bhushan [15] fabricated such a hydrophobic surface with pillars and observed that when the distance between the pillars exceeded a certain critical value, the droplet switched from an elevated (Cassie-Baxter) state to a fully wetted (Wenzel) state. We observed the same qualitative behavior for a smaller droplet volume (1 μL compared to 5 μL), due to computational limitations, and a different value for the surface tensions. The question that arose was, which parameters determine the critical pillar distance?

To answer this question we analyzed the stability and energy barrier of droplets in the Cassie–Baxter state on such periodic patterns. In

addition, we further develop the transition criterion from Patankar [30] and derive an improved version which allows predicting for which pillar distance, equilibrium contact angles and droplet volumes the Cassie–Baxter state switches from a meta stable to an unstable state. This enables a comparison with existing experiments and 3D multiphase Lattice Boltzmann simulations for different pillar geometries and equilibrium contact angles, where a good agreement has been found. We were also able to answer the initial question and can conclude that for low Bond numbers (gravitation can be neglected) the critical pillar distance is independent of the surface tension, but strongly dependent on the droplet radius and thus on the droplet volume.

ACS OMEGA

http://pubs.acs.org/journal/acsodf
Article

Validating the Transition Criteria from the Cassie−Baxter to the Wenzel State for Periodically Pillared Surfaces with Lattice Boltzmann Simulations

Tobias Jäger,* Athanasios Mokos,* Nikolaos I. Prasianakis,* and Stephan Leyer*

Cite This: https://doi.org/10.1021/acsomega.3c08862

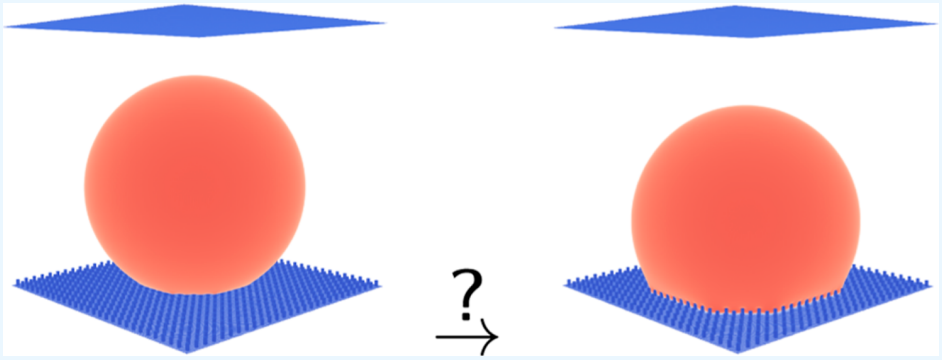

ABSTRACT: Microfabrication techniques allow the development and production of artificial superhydrophobic surfaces that possess a precisely controlled roughness at the micrometer level, typically achieved through the arrangement of micropillar structures in periodic patterns. In this work, we analyze the stability and energy barrier of droplets in the Cassie−Baxter (CB) state on such periodic patterns. In addition, we further develop a transition criterion using the CB equation and derive an improved version which allows predicting for which pillar geometries, equilibrium contact angles, and droplet volumes the CB state switches from a metastable to an unstable state. This enables a comparison with existing experiments and three-dimensional multiphase Lattice Boltzmann simulations for different pillar distances, two contact angles, and two droplet volumes, where a good agreement has been found.

INTRODUCTION

Superhydrophobic surfaces have garnered significant attention because of their outstanding wetting properties and various potential technological applications.[1] Their production has significantly advanced due to improved microfabrication techniques that allow for controlled local roughness at the micrometer scale. Often, these roughnesses are created by periodically arranged micropillar structures.[2−7] Among other applications, this is especially interesting for membrane distillation; Xiao et al.[7] showed that micropillars and hydrophobic coatings have the capability to decrease scaling and extend the operational duration of a membrane. While the development of artificial superhydrophobic surfaces has made progress, certain fundamental aspects regarding the wetting behavior of these surfaces still raise debate. One particular unresolved issue concerns the transition from the superhydrophobic state,[1] known as the Cassie−Baxter (CB) state,[8] for which gas is trapped within the surface roughness, to the completely wet state, known as the Wenzel (W) state.[9] During the transition, the apparent contact angle is decreased, and most of the desirable superhydrophobic characteristics of the surface are lost.[4,7]

It is generally accepted that for many common geometries, the CB state is metastable or unstable. If an energy barrier between the two states is overcome, the transition to the energetically stable Wenzel state occurs.[10−13] This energy barrier can already be overcome due to small perturbations such as surface waves created by gravitational or capillary forces at the liquid−air interface.[4] The transition behavior is often approached by describing the Gibbs free energy for the problem. Based on the function for Gibbs free energy, different transition criteria have been formulated.[3,6,10,12,14,15] An

Received: November 7, 2023
Revised: February 8, 2024
Accepted: February 12, 2024

https://doi.org/10.1021/acsomega.3c08862
ACS Omega XXXX, XXX, XXX−XXX

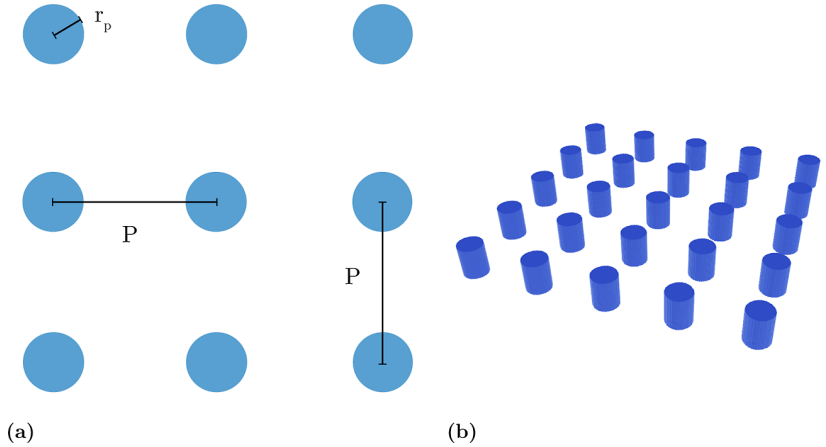

Figure 1. (a) Aerial view (reprinted with permission from Jäger et al.[16] CC BY 4.0) and (b) corresponding 3D structure of a periodically pillared surface with a quadratic unit cell and round pillars.

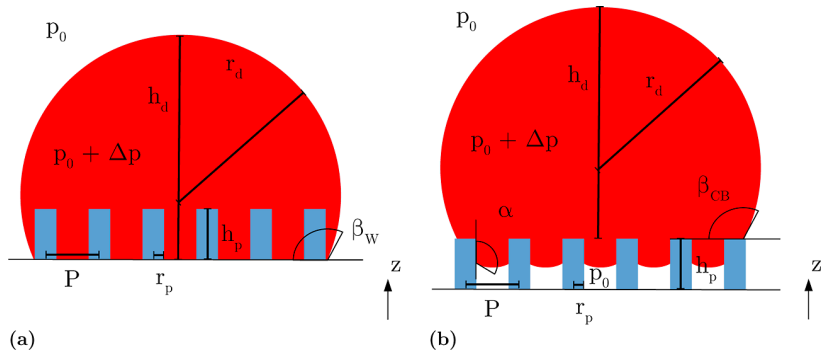

Figure 2. (a) Droplet in the Wenzel state and (b) droplet in an intermediate state. α is the contact angle between the liquid and the vertical pillar wall.

intermediate state, where the liquid wets the pillar walls but does not reach the bottom, also exists.[6]

Jung and Bhushan[4,5] observed in experiments that beyond certain pillar distances, droplets transition from the CB into the Wenzel state. Jäger et al.[16] compared Lattice Boltzmann (LB) simulations to the experimental study from Jung and Bhushan[4] and observed a qualitatively similar behavior for the transition from CB to Wenzel state but observed a much lower critical pillar distance. Zheng et al.[12] and Patankar[11] already developed a transition criterion based on a critical pressure difference and the Young−Laplace pressure difference. In this work, we try to answer the question of which quantities determine the critical pillar distance and aim to derive a formula that allows us to predict the critical pillar distance for a given droplet volume. This allows a comparison to experiments and simulations. In wetting experiments where a droplet is placed on a periodically pillared surface, one can often control the droplet volume; therefore, it is beneficial to know if and how the droplet volume affects the critical pillar distance.

Two mechanisms were identified for this transition: (a) Jung and Bhushan[4] argued that the transition occurs if the droop/sag (δ) at the bottom side of the droplet is much greater than the pillar height (h_p). (b) Patankar[11] derived a transition criterion based on the pressure differences: even before the droop touches the pillar bottom, the Young−Laplace pressure difference Δp between the inside of the liquid droplet and the surrounding air pressure p_0 can result in penetration of liquid between the pillars, ultimately leading to wetting of the bottom between the pillars. Murakami et al.[6] also observed that the Young−Laplace pressure difference is much greater than the hydrostatic pressure on the bottom side of the droplet because of gravity. For small droplets, this suggests that the Young−Laplace pressure difference is an important aspect for the transition from the CB to the Wenzel state. The two aforementioned transition mechanisms can both independently of each other lead to a transition from a CB to the Wenzel state.[11]

The paper is structured as follows: we first give a theoretical background to the problem, particularly regarding the work of Zheng et al.[12] and Patankar,[11] who derived a condition for the critical pressure for an arbitrary periodically pillared surface. We then give a brief overview of the LB multiphase model that is being used to characterize the stability of the CB state. We further develop the condition from Patankar[11] and Zheng[12] using the CB equation[8] and derive a condition which allows predicting for which pillar geometries, equilibrium contact angles, and droplet volumes the CB state switches from a metastable to an unstable state. This condition additionally allows comparison of the theoretical predictions to multiphase LB simulations and existing experiments for multiple pillar geometries.

THEORETICAL BACKGROUND

A periodically pillared surface is characterized by A, the cross-sectional area of the pillar, the rectangular unit cell area A_c which is repeated periodically in x- and y-directions, the pillar

https://doi.org/10.1021/acsomega.3c08862
ACS Omega XXXX, XXX, XXX−XXX

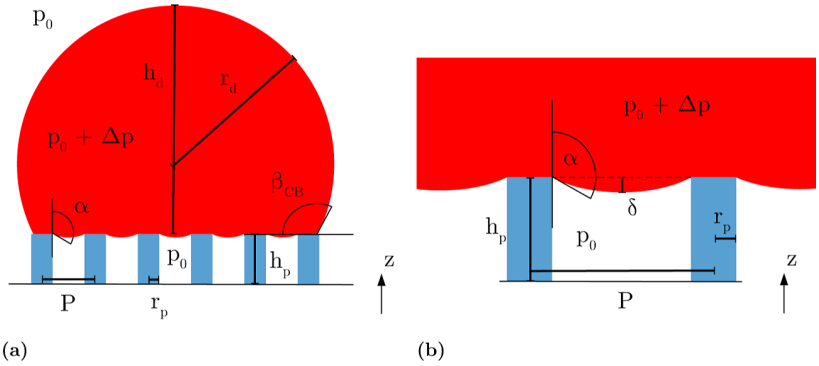

Figure 3. Droplet in the CB state. Full droplet in (a) and the droplet bottom in (b).

perimeter l, and the pillar heights h_p. For a quadratic unit cell with pillar distance P (see Figure 1), $A_c = P \times P$ holds. For pillars with a circular cross section, $l = 2\pi r_p$ and $A = \pi r_p^2$ and for pillars with quadratic cross section, $l = 4d_p$ and $A = d_p^2$ with pillar side length d_p.

Bond number (Bo) is a dimensionless quantity that characterizes the balance between gravitational and capillary forces[17] and is expressed through the subsequent equation: Bo $= \Delta\rho g L^2/\gamma$, where g denotes the gravitational acceleration, $\Delta\rho$ is the difference in the density of liquid and gas, γ denotes the surface tension, and L represents the characteristic length. In the context of liquid droplets, the characteristic length L corresponds to the droplet radius. When the bond number is much smaller than 1 (Bo $\ll$ 1), gravitational effects can be considered negligible.

Wenzel and CB Equation. The equilibrium contact angle α_0 on a flat surface of the same material and the apparent contact angle β_W for a droplet in the Wenzel state (Figure 2) are connected through the Wenzel equation.[9] For details, see the Appendix.

In the case of a droplet in the CB state,[8] in contrast, the equilibrium contact angle α_0 for a similar surface is connected to the apparent contact angle β_{CB} through the subsequent equation

$$\cos\beta_{CB} = \frac{A}{A_c}(\cos\alpha_0 + 1) - 1 \tag{1}$$

If gravitation is negligible, the shape of a droplet in the CB state can be approximated by a spherical cap (see Figure 3), and the droplet radius r_d is given by

$$r_d = \sqrt[3]{\frac{3V_d}{\pi(2+\cos\beta_{CB})(1-\cos\beta_{CB})^2}} = \sqrt[3]{\frac{3V_d}{\pi\left(1+\frac{A}{A_c}(\cos\alpha_0+1)\right)\left(2-\frac{A}{A_c}(\cos\alpha_0+1)\right)}} \tag{2}$$

where V_d is the volume of the droplet (spherical cap). Equation 1 can be used to eliminate the apparent contact angle of the droplet β_{CB} in the equation for the droplet radius.

Stability of the CB and Wenzel States. Based on an equation for the Gibbs free energy by Patankar[10] (shown in the Appendix), Zheng[12] derived a condition to evaluate which of the two droplet states (CB or Wenzel) is the stable state

$$-\cos\beta_W < -\cos\beta_{CB} \tag{3}$$

If that is true, the Wenzel state is stable, whereas the CB wetting mode is meta stable or even unstable.[12,13] In this study, the emphasis is directed toward situations in which the Wenzel state is the stable state with the analysis focusing on which geometries the droplet in the CB state switches from a meta stable to an unstable state.

Young–Laplace Equation. According to Laplace,[18] the pressure difference across a liquid–gas interface Δp is linked to the mean curvature of the interface and the liquid surface tension γ. In a static scenario, where external forces such as gravity are negligible, the pressure difference at the interface is independent of the spatial location. Consequently, the pressure difference Δp is constant everywhere along the liquid–gas interface, including both the liquid–gas interface on top of the droplet and the one between the pillars.

If gravitation is negligible, a droplet in the CB state can be approximated by a spherical cap of radius r_d, and therefore one can calculate the pressure difference according to Laplace[18] by

$$\Delta p = \gamma\frac{2}{r_d} \tag{4}$$

Transition Criterion. *Critical Pressure and Energy Barrier for Periodically Pillared Surfaces.* Zheng et al.[12] used a force balance approach to derive a general expression to calculate the critical pressure for a liquid film on an arbitrary periodically pillared structure and found good agreement with numerical simulations. Jäger et al.[19] were able to confirm their results with multiphase LB simulations. In the critical state, according to[12]

$$F_z = \Delta p_{crit}(A_c - A) + \gamma l \underbrace{\cos(\alpha_0)}_{\substack{\text{projection}\\ \text{along}\\ z\text{-axis}}} = 0 \tag{5}$$

Rearranging gives[12]

$$\Delta p_{crit} = -\frac{\gamma l\cos(\alpha_0)}{A_c - A} \tag{6}$$

Patankar[11] concluded that the CB state transits to the Wenzel state if the Young–Laplace pressure difference ($\Delta p = 2\gamma/r_d$) exceeds the critical value Δp_{crit} (shown in eq 6) and showed that the same condition can be derived when considering the energy barrier and the work done when the liquid moves down the pillar.

If the pressure difference between the liquid above the pillars and the air below exceeds the critical pressure difference Δp_{crit}, the liquid starts to move down the pillars. Based on the work

https://doi.org/10.1021/acsomega.3c08862
ACS Omega XXXX, XXX, XXX−XXX

needed to move down the liquid, Patankar[3] and Zheng[12] calculated the magnitude of the energy barrier per area from CB to Wenzel state by

$$\Gamma_{\mathrm{CB-W}} = h_{\mathrm{p}}\Delta p_{\mathrm{crit}}\frac{A_{\mathrm{c}} - A}{A_{\mathrm{c}}} = -\frac{h_{\mathrm{p}}\gamma l\cos(\alpha_0)}{A_{\mathrm{c}}} \tag{7}$$

Sag Transition. Jäger et al.[4] and Patankar[11] estimated the droop/sag δ by a spherical approximation of the liquid gas interface and obtained $\delta = r_{\mathrm{d}} - \sqrt{r_{\mathrm{d}}^2 - (\sqrt{2}P - 2r_{\mathrm{p}})^2/4}$. Here, $\sqrt{2}P$ is the diagonal distance between two pillar centers, and r_{p} is the pillar radius. For quadratic pillars, the previous equation can be modified as

$$\delta = r_{\mathrm{d}} - \sqrt{r_{\mathrm{d}}^2 - (\sqrt{2}P - \sqrt{2}d_{\mathrm{p}})^2/4} \tag{8}$$

A transition to the Wenzel state occurs when $\delta \geq h_{\mathrm{p}}$.[4,11] Patankar[11] concluded that the sag transition is likely to occur only when the Wenzel state leads to lower energy than the CB state.

NUMERICAL METHOD

To determine the interface of a droplet on top of a rough hydrophobic surface, this study uses a LB multiphase model with additional interactions between fluid and solid. This enables the adjustment of the equilibrium contact angle (α_0) between a flat solid surface and a liquid droplet and allows simulating the liquid−gas flow. Mesoscopic methods, like LB, provide viable predictions for intricate 3D structures, both on the micro- and nano-scales. These methods can be categorized into particle- and lattice-based approaches.[20] The LB framework shows promise due to its ability to handle complex boundary conditions, including rough surfaces.[21] Moreover, it is well-suited for parallelized calculations on GPUs,[20,22,23] enabling simulations in both the continuum and the slip flow regime.[24] In contrast to classical continuum based solvers, the fluid is described by a density distribution function $f(\mathbf{x}, \mathbf{v}, t)$ within the LB framework. $f(\mathbf{x}, \mathbf{v}, t)$ can be seen as an extension to the mass density, also containing information about the velocity distribution.

Similar to previous works, e.g.,[16,21] an isothermal multiphase LB method is employed in this study to predict the shape and state of liquid droplets on micropillar structures and to validate our theoretical findings. A D3Q27 lattice is used, which employs 27 discrete velocities ($\mathbf{c}_i$, i = 0....26) at every lattice node within a three-dimensional (3D) spatial framework.[25] During one time step of length Δt, the discrete distribution function $f_i(\mathbf{x}, t)$ is streamed to its neighboring nodes according to

$$f_i(\mathbf{x} + \mathbf{c}_i\Delta t, t + \Delta t) - f_i(\mathbf{x}, t) = -\frac{1}{\tau}[f_i(\mathbf{x}, t) - f_i^{\mathrm{eq}}(\rho, \mathbf{v}, \mathbf{x}, t)] \tag{9}$$

Typically, the LB method uses the Bhatnagar−Gross−Krook approach to approximate the collisions between the fluid particles.[26] The viscosity is associated with relaxation time τ. Macroscopic quantities like velocity and density are derived by a summation over the discrete distribution function f_i and velocities c_i at a given point in space.[25] The LB method employs a dimensionless approach, where time step (Δt = 1 ts), lattice spacing (Δx = 1lu), and particle mass (m = 1 mu) are set to one unit each, providing stability and faster convergence as commonly done for LB simulations.[27] The method reproduces the Navier−Stokes equation in the hydrodynamic limit.[25]

$$\rho = \sum_{i=0}^{26} f_i \tag{10}$$

$$\mathbf{v} = \frac{1}{\rho}\sum_{i=0}^{26} f_i\mathbf{c}_i \tag{11}$$

In this study, the guided equilibrium model[25,28] was employed to calculate the equilibrium distribution f_i^{eq}. Additional implementation details are given in refs 16, 25, and 28. The selected multiphase model for this research was the Shan−Chen model,[27,29,30] which incorporates a pseudo potential to account for the interactions between fluid particles

$$\mathbf{F} = -G\psi(\mathbf{x}, t)\sum_{i=0}^{26} w_i\psi(\mathbf{x} + \mathbf{c}_i\Delta t, t)\mathbf{c}_i \tag{12}$$

G represents the fluid−fluid interaction strength and controls the surface tension of the fluid. The fluid−solid interaction is modeled by including an additional interaction force $\mathbf{F}_{\mathrm{ads}}$, where $s(\mathbf{x})$ is a step function that takes the value 0 for fluid voxels and 1 for solid voxels.[27,31]

$$\mathbf{F}_{\mathrm{ads}} = -G_{\mathrm{ads}}\psi(\mathbf{x}, t)\sum_{i=0}^{26} w_i s(\mathbf{x} + \mathbf{c}_i\Delta t, t)\mathbf{c}_i \tag{13}$$

The model parameter G_{ads} exhibits a linear correlation with the equilibrium contact angle α_0 measured on a flat solid surface, as demonstrated in a benchmark presented in ref 16 Therefore, this enables the manipulation of the hydrophobicity by adjusting G_{ads}. Detailed information is given in refs 16, 27, and 29.

Furthermore, a nonslip boundary condition (achieved by a bounce-back of the distribution function) was utilized between the fluid and solid surfaces. Unless specified otherwise, periodic boundary conditions were applied in all directions at the boundaries of the computational domain.

For all LB simulations conducted here, we employed G = 120.0, which leads to a surface tension of γ = 14.04 mu ts^{-2} in LB units. This results in ρ_{l} = 524.4 mu lu lu^{-3} (liquid density) and ρ_{g} = 85.7 mu lu^{-3} (gas density) for a flat interface. To realize an equilibrium contact angle of 100°, we used G_{ads} = −174.52.

As the liquid−gas interface shape is solely influenced by the contact line of liquid gas and solid and the parameter $q := \Delta p/\gamma$ [lu^{-1}], it is enough to make sure that q corresponds to the physical problem to capture the correct interface shape. To dimensionalize the problem, the following relationship is used: $\Delta p^{\mathrm{SI}}/\gamma^{\mathrm{SI}} = q^{\mathrm{SI}} = q/\Delta x^{\mathrm{SI}}$, where Δx^{SI} represents the distance between two lattice nodes in SI units. As a consequence, for a droplet on top of the pillar structure, the interface shape is only determined by the droplet radius, the geometry of the pillars, and the equilibrium contact angle α_0. Equation 14 shows the convergence criterion for all simulations conducted in this work, fulfilled with $\varepsilon = 1 \times 10^{-6}$.

$$\varepsilon > \max_{x,y,z}\left(\frac{|\rho^t(x, y, z) - \rho^{t-1}(x, y, z)|}{\rho^{t-1}(x, y, z)}\right) \tag{14}$$

https://doi.org/10.1021/acsomega.3c08862
ACS Omega XXXX, XXX, XXX−XXX

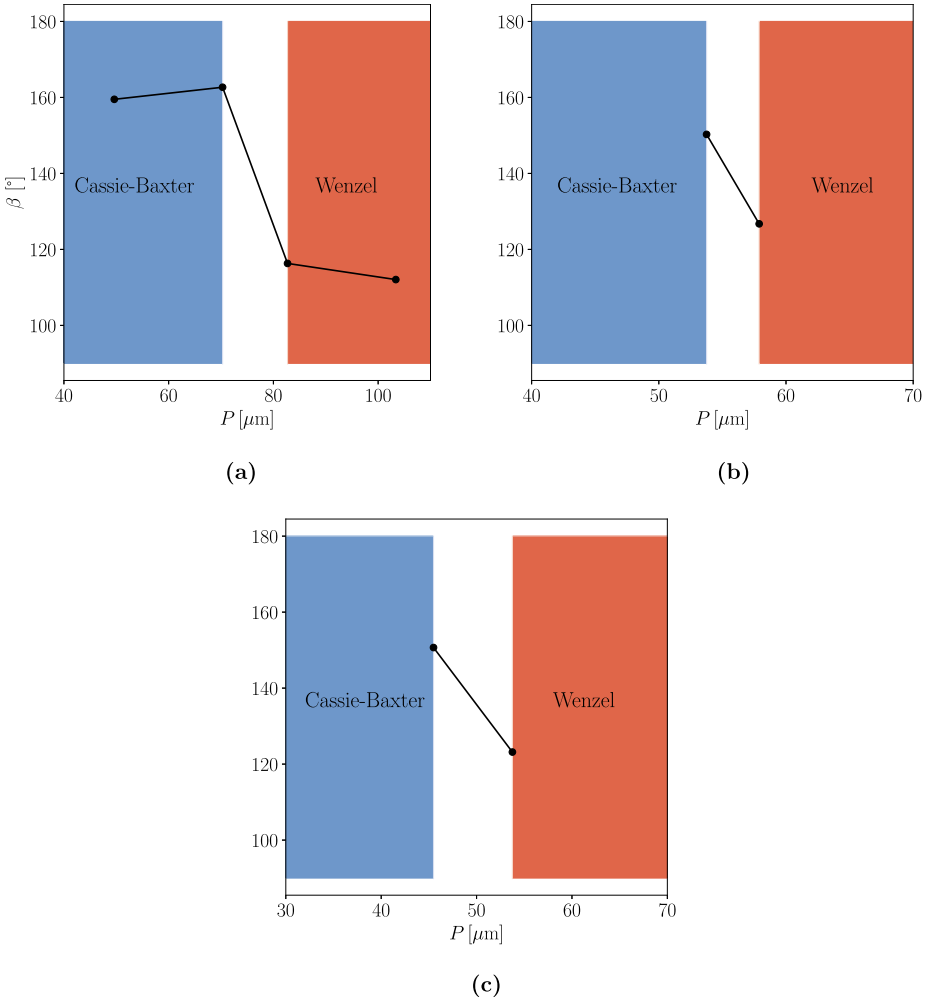

Figure 4. Multiphase simulation results LB1 (Adapted with permission from Jäger et al.[16] CC BY 4.0) in (a). Multiphase simulation results LB2 in (b) and LB3 in (c). The apparent contact angle β for the CB or Wenzel state as a function of the pillar distance P. The blue area marks the CB regime and the red area the Wenzel regime.

All simulations were conducted using an adapted high-performance computing code from Safi.[32] All 3D plots presented in this study were generated using ParaView[33]

RESULTS AND DISCUSSION

Energy Barrier and Transition Criterion for a Finite Droplet. If one places a finite droplet on top of a periodically pillared surface, the Young−Laplace pressure difference effectively lowers the energy barrier per area between the CB and Wenzel states, and a lower external pressure needs to be applied to achieve the transition. Therefore, based on the results from Patankar[11] and Zheng,[12] we propose a modified equation to calculate the energy barrier per area for droplets on periodically pillared surfaces

$$\Gamma_{\mathrm{CB-W,d}} = h_{\mathrm{p}}\left(\Delta p_{\mathrm{crit}} - 2\frac{\gamma}{r_{\mathrm{d}}}\right)\frac{A_{\mathrm{c}} - A}{A_{\mathrm{c}}} \tag{15}$$

Compared to eq 7, which is only applicable if the Young−Laplace pressure difference can be neglected, e.g., for a film on an infinite periodically pillared surface, the new eq 15 takes into account the curvature and is therefore applicable for a finite droplet. Equation 6 was similarly derived for a film on an infinite periodically pillared surface but still remains applicable if the droplet is in contact with multiple pillars. Therefore, it is still used for the calculation of Δp_{crit}. However, a droplet only in contact with a single pillar in the absence of gravity will always remain in a stable state; therefore, eq 6 is not applicable in this case.

It is crucial to keep in mind that this is only valid in the case where gravitation can be neglected, since in this case the pressure difference at the droplet interface does not depend on the direction and the droplet has the shape of a spherical cap with a radius r_{d}. As the bond number approaches 1, the assumption of a spherical cap is no longer reasonable. And an additional term accounting for gravity would enter the equation for the energy barrier and further lower the magnitude of the barrier.

Therefore, we can conclude that in the absence of gravity the energy barrier for a droplet depends not only on h_{p}, γ, l, A, A_{c}, and α_0 but also on r_{d}, the radius of the droplet. The smaller the droplet becomes, the lower the barrier gets. According to the criterion from Patankar[11] ($\Delta p > \Delta p_{\mathrm{crit}}$), an increase of the pressure difference, $\Delta p = 2\gamma/r$, increases the angle α (see Figure 3) until α_0 is reached and eq 4 equals eq 6. When this critical point is reached, the energy barrier vanishes completely, and the CB state switches from a metastable to an unstable

https://doi.org/10.1021/acsomega.3c08862
ACS Omega XXXX, XXX, XXX−XXX

state. From this, one can derive a condition for the critical radius of the droplet

$$r_{\mathrm{d,crit}} = -2\frac{A_c - A}{l\cos(\alpha_0)} \tag{16}$$

It immediately becomes clear that when gravity is absent, the condition for the critical droplet radius in eq 16 is independent of the surface tension.

In experiments, one can often control the volume of the droplet. Therefore, we chose to use the relation for the droplet volume and the droplet (spherical cap) radius in eq 2 to reformulate eq 16.

$$V_{\mathrm{d,crit}}(l, A_c, A, \alpha_0, \beta_{\mathrm{CB}}) = -\frac{8\pi(A_c - A)^3(2 + \cos\beta_{\mathrm{CB}})(1 - \cos(\beta_{\mathrm{CB}}))^2}{3l^3\cos^3(\alpha_0)} \tag{17}$$

Using the CB (1 we can eliminate the apparent contact angle β_{CB}. With $A_c = P \times P$ for a quadratic periodically pillared surface, we then gain a condition (eq 18) for the critical volume which only depends on l the perimeter of the pillar, P the distance between two pillars, A the top area of the pillars, and the equilibrium contact angle α_0.

$$V_{\mathrm{d,crit}}(l, P, A, \alpha_0) = -\frac{8\pi(P^2 - A)^3\left(1 + \frac{A}{P^2}(\cos\alpha_0 + 1)\right)\left(2 - \frac{A}{P^2}(\cos\alpha_0 + 1)\right)^2}{3l^3\cos^3(\alpha_0)} \tag{18}$$

Iterative root-finding procedures can be used to solve eq 18 numerically for the other variables (l, P, A, α_0). We used this procedure to calculate $P_{\mathrm{crit}}(\alpha_0, l, A, V)$ numerically and compare the predictions of condition 18 to experimental results from Jung and Bhushan[4] and multiphase LB simulations from Jäger et al.[16] (see Figure 4a) and new multiphase LB simulations for additional geometries (see Figure 4b,c). In Jung and Bhushan's[4] experiments, a droplet of 5 μL was placed on a periodically pillared surface; then they observed whether the static droplet ended up in either the CB or Wenzel state and measured the apparent contact angle. The experiment was repeated for different pillar distances P. Therefore, Jung and Bhushan[4] were able to determine a range of P for which a transition from CB to Wenzel state takes place.

Numerical and Experimental Validation. Previously, Jäger et al.[16] compared the results from Jung and Bhushan[4] (Exp. 1 and 2) to multiphase LB simulations (LB1) with a similar geometry and equilibrium contact angle but a smaller droplet of only 1 μL volume due to computational limitations. Simulation results from Jäger et al.[16] (LB1) are shown in Figure 4 (a). They observed the same qualitative behavior in the simulations, but the transition from CB to Wenzel state occurred for a smaller P compared to the experimental study by Jung and Bhushan[4] (see Table 1). We also added the theoretical predictions for P_{crit} based on eq 18 in Table 1.

In the LB simulations, the droplet transitions to a different state even in the absence of gravity and with zero initial velocity because, after initializing a spherical droplet just above the pillar structure, small oscillations occur until the liquid and gas density converged to their equilibrium values. This is enough perturbation to make the transition happen if the critical state is reached. These dampened oscillations are typical for LB multiphase simulations and vanish over time.

Table 1. Observed and Theoretically Predicted Critical Pillar Distance P_{crit} for Different Experimental and Numerical (LB1, LB2, LB3) Setups

	Exp. 1 Jung[4]	Exp. 2 Jung[4]	LB1[16]	LB2	LB3
α_0 [°]	109	109	109	100	100
l [μm]	15.708	43.982	49.62	66.16	49.62
A [μm^2]	19.635	153.938	153.88	273.57	153.88
V_{d} [μL]	5	5	1	1	1
h_{p} [μm]	10	30	33.08	33.08	33.08
stable state	Wenzel	Wenzel	Wenzel	Wenzel	Wenzel
δ [μm]	2	4	5	3	2
Bo	0.24	0.24	0.083	0.083	0.082
observed P_{crit} [μm]	44−60	125−167	70−83	54−58	45−54
[lu]			17−20	13−14	11−13
predicted P_{crit} [μm]	52.27	88.03	71.87	61.96	53.17

In this paper, we investigate two additional pillar geometries (LB2 and LB3) with the same multiphase LB method. The corresponding results for the droplet state and the contact angle are shown in Figure 4b,c. An example of a droplet in the CB or the Wenzel state is given in Figure 5. For all LB simulations in this paper, we used rectangular pillars of either $A = 3 \times 3$ lu^3 or $A = 4 \times 4$ lu^3. Here, $\Delta x = 1$ lu $\equiv 4.135$ μm was chosen to match the geometries in the experimental study from Jung and Bhushan.[4] A spherical droplet of volume 1 μL is initialized right above the pillar structure with zero velocity according to eq 19

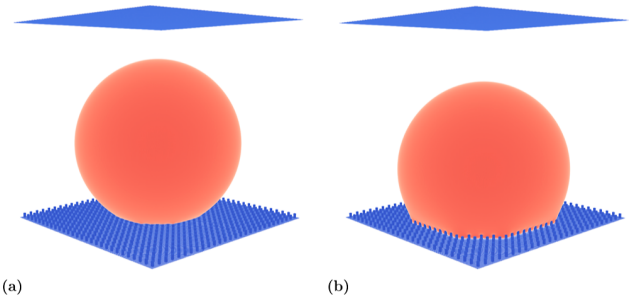

Figure 5. Droplet in contact with geometry LB2. In (a) is shown a droplet in the CB state for $P = 54$ μm and in (b) is shown a droplet in the Wenzel state $P = 58$ μm.

$$\rho(x, y, z) = \frac{\rho_l + \rho_g}{2} + \frac{\rho_g - \rho_l}{2} \times \tanh\left(\frac{2[\sqrt{(x - x_0)^2 + (y - y_0) + (z - z_0)^2} - r]}{5}\right) \tag{19}$$

for every simulation with $r = 150$lu. This leads to a volume of $V_{\mathrm{d}} \approx 1.0$ μL.

Total domain size was about $370 \times 370 \times 370$ lu$^3 \equiv 3.58$ mm^3 for each simulation. For all the setups which we investigated numerically, we ensured full contact with the droplet in the Wenzel state for at least 9 pillars.

In Figure 6 the dependence of the critical volume on the pillar distance P according to eq 18 is shown for the two experiments and the LB simulations. The intersection of $V_{\mathrm{d,crit}}(P)$ with a given droplet volume V_{d} gives a predicted value

https://doi.org/10.1021/acsomega.3c08862
ACS Omega XXXX, XXX, XXX−XXX

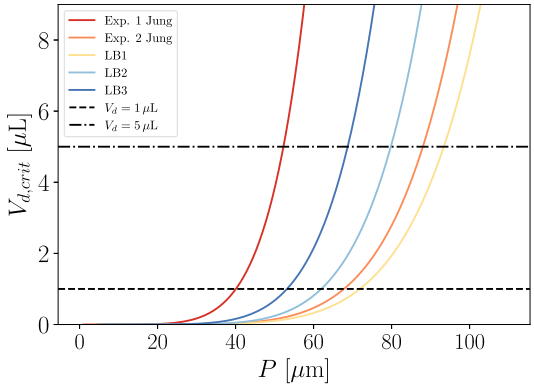

Figure 6. Dependence of the critical droplet volume $V_{d,crit}$ on the pillar distance P according to eq 18 for different experimental[4] and numerical (LB1,[16] LB2, LB3) setups.

for P_{crit}. Table 1 contains the experimental and simulation parameters (experiment 1, experiment 2, and LB simulations LB1, LB2, and LB3), as well as the observed and theoretically predicted values for P_{crit}. For all analyzed geometries, according to eq 3 the Wenzel state is the stable configuration, and since the sag is much smaller than the pillar heights ($\delta < h_p$) the transition occurs due to the Young−Laplace pressure difference (see Table 1). The bond number was calculated to be below 1 for all droplets.

Comparing these results with the two experiments by Jung and Bhushan[4] and LB simulations (see Table 1), we found very good agreement for experiment 1 and the LB simulations; the predicted critical values P_{crit} based on condition 18 lie within the observed range; only for LB simulation 2 the predicted value was slightly high. For the setup from experiment 2, the predicted value (P_{crit} = 88.03 μm) is below the range (125−167 μm) found in the experiment by Jung and Bhushan.[4] Figure 7b,d show the Wenzel and CB states for LB2, respectively.

We also simulated cases with equilibrium contact angles larger than 109°. However, this results in a state in which the droplet is in contact with only a few pillars. Therefore, these results are not comparable to the theoretical transition criterion.

It is important to mention that for the present LB simulations, a change in the pillar height can also change the droplet state. For example, for the LB2 setup, if we increase the pillar height to h_p = 49.62 μm and rerun the simulations, no transition to the Wenzel state was observed for P = 58 μm (see Figure 7a). Whereas for pillars with a height h_p = 33.08 μm, as reported in Table 1, we observed a transition to the Wenzel state for P = 58 μm (see Figure 7b). Increasing P for h_p = 49.62 μm, we can also observe a transition to the intermediate state (see Figure 7c).

To compare the influences of the different variables on the critical droplet volume $V_{d,crit}$, we calculated the partial derivatives of $V_{d,crit}$ in eq 18 with respect to the variables A, l, P, and α_0 and listed the magnitude of the derivatives in Table 2.

$$\frac{\partial V_{d,crit}}{\partial A} = \frac{8(-A + P^2)^2\pi(A - 2P^2 + A\cos(\alpha_0))(2(A^2 - AP^2 - P^4) + A(4A - 3P^2)\cos(\alpha_0) + A(2A - P^2)\cos^2(\alpha_0))}{l^3P^6\cos^3(\alpha_0)} \quad (20)$$

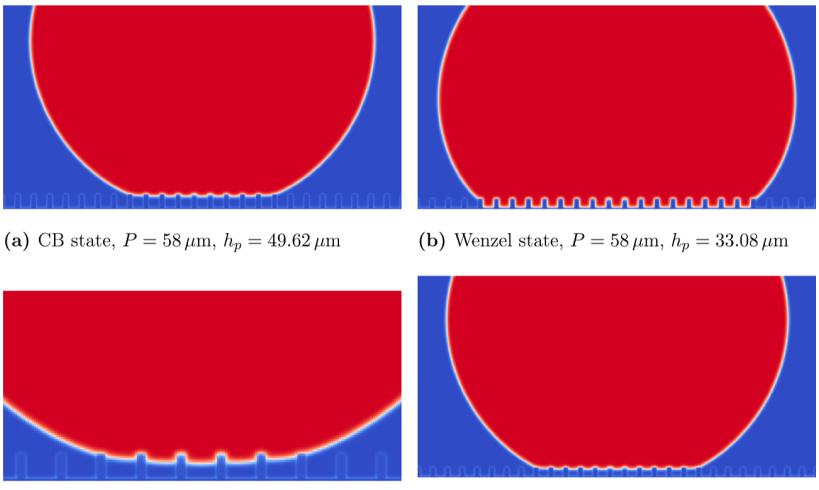

(a) CB state, $P = 58\,\mu$m, $h_p = 49.62\,\mu$m

(b) Wenzel state, $P = 58\,\mu$m, $h_p = 33.08\,\mu$m

(c) Intermediate state, $P = 79\,\mu$m, $h_p = 49.62\,\mu$m

(d) CB state, $P = 54\,\mu$m, $h_p = 33.08\,\mu$m

Figure 7. Slice of a 3D droplet (in red) on a periodically pillared surface from the present LB simulation results. For all setups shown in this figure, $A = 4 \times 4$ lu^3 holds, $\alpha_0 = 100°$.

https://doi.org/10.1021/acsomega.3c08862
ACS Omega XXXX, XXX, XXX−XXX

Table 2. Influence of the Different Variables on $V_{d,crit}$

$\frac{1}{V_{crit}}\frac{\partial V_{d,crit}}{\partial A}$	$\frac{1}{V_{crit}}\frac{\partial V_{d,crit}}{\partial l}$	$\frac{1}{V_{crit}}\frac{\partial V_{d,crit}}{\partial P}$	$\frac{1}{V_{crit}}\frac{\partial V_{d,crit}}{\partial \alpha_0}$	A	l	P	α_0	V_{crit}
[μm^{-2}]	[μm^{-1}]	[μm^{-1}]	[1/°]	[μm^2]	[μm]	[μm]	[deg]	[μL]
−0.00020	−0.03431	0.02077	−0.76282	19.63	15.71	52.27	109	5
−0.000071	−0.01225	0.01249	−0.76285	153.94	43.98	88.03	109	5
−0.00011	−0.01086	0.01546	−0.76288	153.88	49.62	71.87	109	1

$$\frac{\partial V_{d,crit}}{\partial l} = -\frac{8(A - P^2)^3\pi(A - 2P^2 + A\cos(\alpha_0))^2(A + P^2 + A\cos(\alpha_0))}{l^4P^6\cos^3(\alpha_0)} \tag{21}$$

$$\frac{\partial V_{d,crit}}{\partial P} = -\frac{16(-A + P^2)^2\pi(A - 2P^2 + A\cos(\alpha_0))(A^3 - AP^4 - 2P^6 + (2A^3 - AP^4)\cos(\alpha_0) + A^3\cos^2(\alpha_0))}{l^3P^7\cos^3(\alpha_0)} \tag{22}$$

$$\frac{\partial V_{d,crit}}{\partial \alpha_0} = \frac{8(A - P^2)^3\pi(A - 2P^2 + A\cos(\alpha_0))(A^2 - AP^2 - 2P^4 + A(A - P^2)\cos(\alpha_0))\tan(\alpha_0)}{l^3P^6\cos^3(\alpha_0)} \tag{23}$$

As shown in Table 2, we found that the equilibrium contact angle has by far the largest influence among all of the parameters. A 3° higher equilibrium contact angle for experiment 2 (α_0 = 112°) leads to a predicted P_{crit} = 94.3 μm. Therefore, an error in the equilibrium contact angle measurements alone can not explain the difference between observation and theoretical prediction for experiment 2, but it can explain the small difference observed in the LB2 simulations (see Table 1). A possible explanation is that in experiment 2 the droplet switched and maintained the intermediate state instead of fully transitioning to the Wenzel state when reaching P_{crit}. This hypothesis is supported by the equation for the energy barrier (eq 15), which increases linearly with h_p. Experiments 1 and 2 have the same droplet volume, but the pillar heights differ by a factor of 3, which could explain the difference in predictions between experiments 1 and 2.

We also observed in the LB simulations that the transition to the Wenzel state depends on h_p. Even if the energy barrier in eq 15 completely vanished when P_{crit} is reached, one still needs some perturbation to make the transition to the Wenzel state happen. In the absence of gravity, as for our simulation, the oscillation of the droplet after the initialization provides the perturbation needed to make the transition happen. If the pillars are too high the perturbations dampen out before the transition to the Wenzel state is completed, and the droplet remains in the Wenzel or intermediate state. During the transition and especially for high pillars, the droplet radius and therefore the Young−Laplace pressure difference could decrease and the critical pressure might not be reached anymore, and the droplet gets stuck in the intermediate state.

CONCLUSIONS

Based on the work of Patankar[11] and Zheng et al.,[12] we have derived an equation for the energy barrier between CB and Wenzel states for droplets on periodically pillared surfaces. Due to the curvature of the droplets, there is a pressure difference between the droplet and the surrounding air, which lowers the transition barrier from the CB to the Wenzel state. The smaller the droplet becomes, the lower the transition barrier becomes. Furthermore, we derived a condition which allows to calculate the pillar geometries, equilibrium contact angles, and droplet volumes for which the CB state becomes unstable, which is especially useful if one wants to compare the theoretical findings from Patankar[11] and Zheng[12] to experimental results or simulations. The criterion in eq 16 is applicable for droplets on any periodically arranged roughness with vertical lateral surfaces and a flat horizontal top surface if gravitation is negligible and the area of the unit cell A_c is much smaller than the droplet cross section.

Based on theoretical considerations, we can conclude that the droplet size has a significant effect on the stability of the CB state. The surface tension plays a role only in the magnitude of the energy barrier. These findings are validated with experimental results and 3D multiphase LB simulations for two equilibrium contact angles (100 and 109°) and two droplet volumes (1 and 5 μL). The emphasis of this work was on the influence of pillar spacing, for which we found good agreement. To further validate the predictive power of 18 more experiments and LB simulations for different droplet volumes and different equilibrium contact angles are needed.

APPENDIX

Wenzel equation

The Wenzel equation[9] links the apparent contact angle in the Wenzel state to the equilibrium contact angle α_0.

$$\cos\beta_W = R_f\cos\alpha_0 \tag{24}$$

Here, R_f is the roughness factor defined by the ratio of rough to planar surface areas. For periodically repeated pillars, $R_f = 1 + A_l/A_c$, where $A_l = l \times h_p$ is the lateral surface of the pillar.

https://doi.org/10.1021/acsomega.3c08862
ACS Omega XXXX, XXX, XXX−XXX

Gibbs Free Energy for a Droplet

Patankar[10] derived an equation for the Gibbs free energy E_G of a droplet with the shape of a spherical cap in contact with the pillar structure in any state.

$$E_G = (9\pi)^{1/3} V_d^{2/3} \gamma (2 - 3\cos(\beta) + \cos^3(\beta))^{1/3} \quad (25)$$

Since E_G is a strictly monotonically increasing function of $-\cos(\beta)$ in eq 25, the following relation needs to be true for the Wenzel wetting mode to be associated to a lower Gibbs free energy than the CB:[3,10,12,13] $-\cos\beta_W < -\cos\beta_{CB}$

AUTHOR INFORMATION

Corresponding Authors

Tobias Jäger − *Department of Engineering, Faculty of Science, Technology and Medicine, University of Luxembourg, Luxembourg L-1359, Luxembourg;* orcid.org/0000-0002-6588-2417; Email: tobias.jaeger@uni.lu

Athanasios Mokos − *Transport Mechanisms Group, Laboratory for Waste Management, Paul Scherrer Institute, Villigen 5232, Switzerland*; Email: athanasios.mokos@psi.ch

Nikolaos I. Prasianakis − *Transport Mechanisms Group, Laboratory for Waste Management, Paul Scherrer Institute, Villigen 5232, Switzerland*; Email: nikolaos.prasianakis@psi.ch

Stephan Leyer − *Department of Engineering, Faculty of Science, Technology and Medicine, University of Luxembourg, Luxembourg L-1359, Luxembourg*; Email: stephan.leyer@uni.lu

Complete contact information is available at: https://pubs.acs.org/10.1021/acsomega.3c08862

Author Contributions

Conceptualization, T. Jäger; methodology, T. Jäger, N. I. Prasianakis, and S. Leyer; software, T. Jäger, A. Mokos, N.I. Prasianakis; validation, T. Jäger, A. Mokos, N. I. Prasianakis, and S. Leyer; formal analysis, T. Jäger; investigation, T. Jäger, A. Mokos, N. I. Prasianakis, and S. Leyer; resources, N. I. Prasianakis and S. Leyer; data curation, T. Jäger; writing−original draft preparation, T. Jäger ; writing−review and editing, T. Jäger, A. Mokos, N. I. Prasianakis, and S. Leyer; visualization, T. Jäger; supervision, A. Mokos, N. I. Prasianakis, and S. Leyer; project administration, T. Jäger, N. I. Prasianakis, and S. Leyer; funding acquisition, N. I. Prasianakis and S. Leyer. All authors have read and agreed to the published version of the manuscript.

Funding

University of Luxembourg, Paul Scherrer Institute. This research received no external funding.

Notes

The authors declare no competing financial interest.

ACKNOWLEDGMENTS

The calculations in this paper were carried out using the HPC facilities of the University of Luxembourg[34] (see `hpc.uni.lu`) and the Swiss Supercomputing Center CSCS (project s1155). We also thank the University of Luxembourg and SwissNuclear for its support.

NOMENCLATURE

Δp_{crit}	critical pressure difference
γ	surface tension
q	$\Delta p/\gamma$
r_p	pillar radius
α	contact angles between the liquid and the pillar wall
α_0	equilibrium contact angle between liquid and solid
P	pillar distance (periodicity in x- and y-directions)
A_c	area of the periodically repeated cell ($A_c = P \times P$)
A	top area of the pillar
l	perimeter of the pillar
LB	lattice Boltzmann
p	pressure
ρ	density
ρ_l	liquid density
ρ_g	gas density
$\mathbf{F}$	force
Δx	lattice spacing
Δt	time step
m	fluid particle mass
G_{ads}	LB parameter to tune the equilibrium contact angle
G	LB parameter to control the fluid−fluid interaction strength
τ	relaxation time
ν	kinematic viscosity
c_s	speed of sound
g	gravitation acceleration
$\mathbf{v}$	velocity
$\mathbf{c}_i$	discrete lattice velocity

REFERENCES

(1) Giacomello, A.; Chinappi, M.; Meloni, S.; Casciola, C. M. Metastable Wetting on Superhydrophobic Surfaces: Continuum and Atomistic Views of the Cassie-Baxter−Wenzel Transition. *Phys. Rev. Lett.* **2012**, *109*, 226102.

(2) Yoshimitsu, Z.; Nakajima, A.; Watanabe, T.; Hashimoto, K. Effects of Surface Structure on the Hydrophobicity and Sliding Behavior of Water Droplets. *Langmuir* **2002**, *18*, 5818−5822.

(3) Patankar, N. A. *Transition between Superhydrophobic States on Rough Surfaces*, 2004.

(4) Jung, Y.; Bhushan, B. Wetting behaviour during evaporation and condensation of water microdroplets on superhydrophobic patterned surfaces. *J. Microsc.* **2008**, *229*, 127−140.

(5) Bhushan, B.; Chae Jung, Y. Wetting study of patterned surfaces for superhydrophobicity. *Ultramicroscopy* **2007**, *107*, 1033−1041.

(6) Murakami, D.; Jinnai, H.; Takahara, A. Wetting Transition from the Cassie−Baxter State to the Wenzel State on Textured Polymer Surfaces. *Langmuir* **2014**, *30*, 2061−2067. PMID: 24494786

(7) Xiao, Z.; Zheng, R.; Liu, Y.; He, H.; Yuan, X.; Ji, Y.; Li, D.; Yin, H.; Zhang, Y.; Li, X.-M.; He, T. Slippery for scaling resistance in membrane distillation: A novel porous micropillared superhydrophobic surface. *Water Res.* **2019**, *155*, 152−161.

(8) Cassie, A. B. D.; Baxter, S. Wettability of porous surfaces. *Trans. Faraday Soc.* **1944**, *40*, 546−551.

(9) Wenzel, R. N. RESISTANCE OF SOLID SURFACES TO WETTING BY WATER. *Ind. Eng. Chem.* **1936**, *28*, 988−994.

(10) Patankar, N. A. On the Modeling of Hydrophobic Contact Angles on Rough Surfaces. *Langmuir* **2003**, *19*, 1249−1253.

(11) Patankar, N. A. Consolidation of Hydrophobic Transition Criteria by Using an Approximate Energy Minimization Approach. *Langmuir* **2010**, *26*, 8941−8945 PMID: 20158175.

(12) Zheng, Q.-S.; Yu, Y.; Zhao, Z.-H. Effects of hydraulic pressure on the stability and transition of wetting modes of superhydrophobic surfaces. *Langmuir* **2005**, *21*, 12207−12212.

(13) Yeo, J.; Choi, M. J.; Kim, D. S. Robust hydrophobic surfaces with various micropillar arrays. *J. Micromech. Microeng.* **2010**, *20*, 025028.

https://doi.org/10.1021/acsomega.3c08862
ACS Omega XXXX, XXX, XXX−XXX

(14) Xue, Y.; Chu, S.; Lv, P.; Duan, H. Importance of Hierarchical Structures in Wetting Stability on Submersed Superhydrophobic Surfaces. *Langmuir* **2012**, *28*, 9440−9450.
(15) Lv, P.; Xue, Y.; Shi, Y.; Lin, H.; Duan, H. Metastable States and Wetting Transition of Submerged Superhydrophobic Structures. *Phys. Rev. Lett.* **2014**, *112*, 196101.
(16) Jäger, T.; Mokos, A.; Prasianakis, N. I.; Leyer, S. Pore-Level Multiphase Simulations of Realistic Distillation Membranes for Water Desalination. *Membranes* **2022**, *12*, 1112.
(17) Kunes, J. *Dimensionless Physical Quantities in Science and Engineering*; Elsevier Scientific Pub. Co Amsterdam: New York, 2012.
(18) de Laplace, P. S. *Supplément au dixième livre du Traité de Mécanique Céleste*; J.B.M. Duprat, 1805; Vol. *4*, pp 1−79.
(19) Jäger, T.; Keup, J.; Prasianakis, N. I.; Leyer, S. Theoretical and Numerical Constant Mean Curvature Surface and Liquid Entry Pressure Calculations for a Combined Pillar-Pore Structure. *Coatings* **2023**, *13*, 865.
(20) Schiller, U. D.; Krüger, T.; Henrich, O. Mesoscopic modelling and simulation of soft matter. *Soft Matter* **2018**, *14*, 9−26.
(21) Xiong, W.; Cheng, P. Mesoscale simulation of a molten droplet impacting and solidifying on a cold rough substrate. *Int. Commun. Heat Mass Tran.* **2018**, *98*, 248−257.
(22) Prasianakis, N. I.; Rosén, T.; Kang, J.; Eller, J.; Mantzaras, J.; Büichi, F. N. Simulation of 3D Porous Media Flows with Application to Polymer Electrolyte Fuel Cells. *Commun. Comput. Phys.* **2013**, *13*, 851−866.
(23) Rosen, T.; Eller, J.; Kang, J.; Prasianakis, N. I.; Mantzaras, J.; Büchi, F. N. Saturation dependent effective transport properties of PEFC gas diffusion layers. *J. Electrochem. Soc.* **2012**, *159*, F536−F544.
(24) Luo, K.; Xia, J.; Monaco, E. Multiscale modelling of multiphase flow with complex interactions. *J. Multiscale Model.* **2009**, *01*, 125−156.
(25) Prasianakis, N. I.; Karlin, I. V.; Mantzaras, J.; Boulouchos, K. B. Lattice Boltzmann method with restored Galilean invariance. In *Computational methods in fluid dynamics*; Kinetic theory, 2009.
(26) Qian, Y. H.; D'Humières, D.; Lallemand, P. Lattice BGK Models for Navier-Stokes Equation. *Europhys. Lett.* **1992**, *17*, 479−484.
(27) Peng, C.; Tian, S.; Li, G.; Sukop, M. C. Single-component multiphase lattice Boltzmann simulation of free bubble and crevice heterogeneous cavitation nucleation. *Phys. Rev. E* **2018**, *98*, 023305.
(28) Safi, M. A.; Mantzaras, J.; Prasianakis, N. I.; Lamibrac, A.; Büchi, F. N. A pore-level direct numerical investigation of water evaporation characteristics under air and hydrogen in the gas diffusion layers of polymer electrolyte fuel cells. *Int. J. Heat Mass Transfer* **2019**, *129*, 1250−1262.
(29) Shan, X.; Chen, H. Lattice Boltzmann model for simulating flows with multiple phases and components. *Phys. Rev. E* **1993**, *47*, 1815−1819.
(30) Shan, X.; Chen, H. Simulation of nonideal gases and liquid-gas phase transitions by the lattice Boltzmann equation. *Phys. Rev. E: Stat. Phys., Plasmas, Fluids, Relat. Interdiscip. Top.* **1994**, *49*, 2941−2948.
(31) Sukop, M. C.; Thorne, D. T. *Lattice Boltzmann Modeling*; Springer Berlin: Heidelberg, Germany, 2006.
(32) Safi, M. A.; Prasianakis, N. I.; Mantzaras, J.; Lamibrac, A.; Büchi, F. N. Experimental and pore-level numerical investigation of water evaporation in gas diffusion layers of polymer electrolyte fuel cells. *Int. J. Heat Mass Transfer* **2017**, *115*, 238−249.
(33) Ahrens, J.; Geveci, B.; Law, C. *Visualization Handbook*; Elsevier, 2005; ISBN 978−0123875822.
(34) Varrette, S.; Cartiaux, H.; Peter, S.; Kieffer, E.; Valette, T.; Olloh, A. *Proceeding of the 6th ACM High Performance Computing and Cluster Technologies Conference (HPCCT 2022)*; Fuzhou: China, 2022.Management of an Academic HPC & Research Computing Facility: The ULHPC Experience 2.0

https://doi.org/10.1021/acsomega.3c08862
ACS Omega XXXX, XXX, XXX−XXX

6

SATURATION LEVEL IN AIR GAP MEMBRANE DISTILLATION PROCESSES

6.1 INTRODUCTION

When modelling a complete AGMD module it is often assumed that the air inside the air gap and the membrane is fully saturated and the vapor pressure (partial pressure of water vapor) equals the saturation vapor pressure everywhere in the air gap, e.g. Alsaadi et al. [4], Im et al. [13], Karbasi et al. [17], and Kerstin Cramer and Leyer [18]. This is an assumption which is often poorly justified. Since the vapor pressure has a significant impact on the magnitude of the evaporation flux [32] and therefore on the performance of the AGMD module, it is crucial to better understand which vapor pressure can be expected in AGMD modules. Therefore we theoretically investigate which phenomenon between evaporation and diffusion happens at a faster rate in the air–gap. This finally determines the saturation level in the air–gap. We compare the diffusion coefficient with the evaporation coefficient from the Hertz–Knudsen equation (discussed in chapter 2) to determine the influencing parameters and the areas of predominance of each phenomenon.

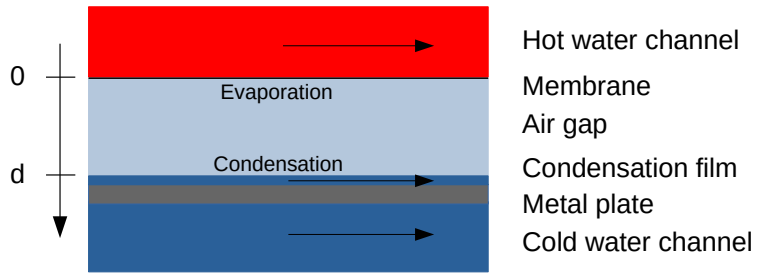

Figure 6.1: Schema of an AGMD module.

6.2 RESULTS

In a first approximation the air gap can be treated as a 1 dimensional problem (see figure 6.1). For the steady–state case in 1D the flux needs to be the same at the evaporation boundary at $x = 0$, everywhere in the domain and at the condensation boundary at $x = d$. The subscript $_0$ indicates a quantity at $x = 0$ and the subscript $_d$ indicates a quantity at $x = d$.

The evaporation (j_e at $x = 0$) and condensation flux (j_c at $x = d$) can be estimated with the Hertz–Knudsen equation 2.16 (introduced in chapter 2). The partial vapor pressure $p^{\bar{V}}$ is calculated with the ideal gas law, p_s is the saturation vapor pressure, $R_{s,w}$ is the specific gas constant of water vapor. As the saturation level we define the ratio of the actual vapor density over the saturation vapor density ($\rho_0/\rho_{0,s}$). Finally the following equations hold for the evaporation and condensation flux:

$$j_e = \sqrt{\frac{m}{2\pi k_B T_0}} \left[\sigma_{e,0} p_s(T_0) - \sigma_{c,0} R_{s,w}\, T_0\, \rho_0\right] \tag{6.1}$$

$$j_c = \sqrt{\frac{m}{2\pi k_B T_d}} \left[\sigma_{c,d} R_{s,w}\, T_d\, \rho_d - P_s(T_d)\sigma_{e,d}\right] \tag{6.2}$$

Since all fluxes are the same at steady state the following equation holds:

$$j_e = j_c \tag{6.3}$$

From this one can deduce the following relations:

$$\frac{\sigma_{e,0} P_s(T_0) - \sigma_{c,0} R_{s,w}\, T_0\, \rho_0}{\sigma_{c,d} R_{s,w}\, T_d\, \rho_d - P_s(T_d)\sigma_{e,d}} = \sqrt{\frac{T_0}{T_d}} \tag{6.4}$$

$$\rho_0 = \frac{\sigma_{e,0} p_s(T_0) - \sqrt{T_0/T_d}(\sigma_{c,d} R_{s,w} T_d \rho_d - p_s(T_d)\sigma_{e,d})}{\sigma_{c,0} R_{s,w} T_0} \tag{6.5}$$

$$\rho_d = \frac{\sigma_{e,d} p_s(T_d) - \sqrt{T_d/T_0}(\sigma_{c,0} R_{s,w} T_0 \rho_0 - p_s(T_0)\sigma_{e,0})}{\sigma_{c,d} R_{s,w} T_d} \tag{6.6}$$

$$j = -\frac{D}{d}(\rho_d - \rho_0) = -v_d(\rho_d - \rho_0) \tag{6.7}$$

Moreover the diffusive flux j within the air–gap needs to be equal to the evaporation (and condensation) flux:

$$j = j_e \tag{6.8}$$

j can be in a first approximation calculated with Fick's law (compare equation 6.7).

Yielding:

$$\rho_d = -\frac{1}{v_D}\sqrt{\frac{m}{2\pi k_B T_0}}\sigma_{e,0} p_s(T_0) + (\frac{1}{v_D}\sqrt{\frac{m}{2\pi k_B T_0}}\sigma_{c,0} R_{s,w} T_0 + 1)\rho_0 \tag{6.9}$$

Combining equation 6.5 and 6.9 one finally gets an expression for ρ_0 and therefore also for ρ_d and j.

$$\rho_0 = \frac{\sigma_{c,d} R_{s,w} T_d \frac{1}{v_D}\sqrt{\frac{m}{2\pi k_B T_0}}\sigma_{e,0} p_s(T_0) + \sigma_{e,d} p_s(T_d) + \sqrt{T_d/T_0} p_s(T_0)\sigma_{e,0}}{\sigma_{c,d} R_{s,w} T_d (\frac{1}{v_D}\sqrt{\frac{m}{2\pi k_B T_0}}\sigma_{c,0} R_{s,w} T_0 + 1) + \sqrt{T_d/T_0}\sigma_{c,0} R_{s,w} T_0} \tag{6.10}$$

Defining $c_0 = \sqrt{\frac{m}{2\pi k_B T_0}}$ and rearranging equation 6.10 one gets:

$$\rho_0 = \frac{p_s(T_0) R_{s,w} T_d c_0 \sigma_{c,d}\sigma_{e,0}\frac{1}{v_D} + p_s(T_d)\sigma_{e,d} + \sqrt{T_d/T_0} p_s(T_0)\sigma_{e,0}}{R_{s,w} T_d \sigma_{c,d}(R_{s,w} T_0 c_0 \sigma_{c,0}\frac{1}{v_D} + 1) + \sqrt{T_d/T_0} R_{s,w} T_0 \sigma_{c,0}} \tag{6.11}$$

In a first investigation we chose $\sigma_{c,0} = \sigma_{c,d} = \sigma_{e,0} = \sigma_{e,d} = \sigma$ and tested two values, $\sigma = 10^{-3}$ and $\sigma = 10^{-2}$. The resulting saturation level at the evaporation ($x = 0$) and condensation ($x = d$) interface is shown in 6.2. The corresponding flux for $\sigma = 10^{-3}$ is shown in figure 6.3

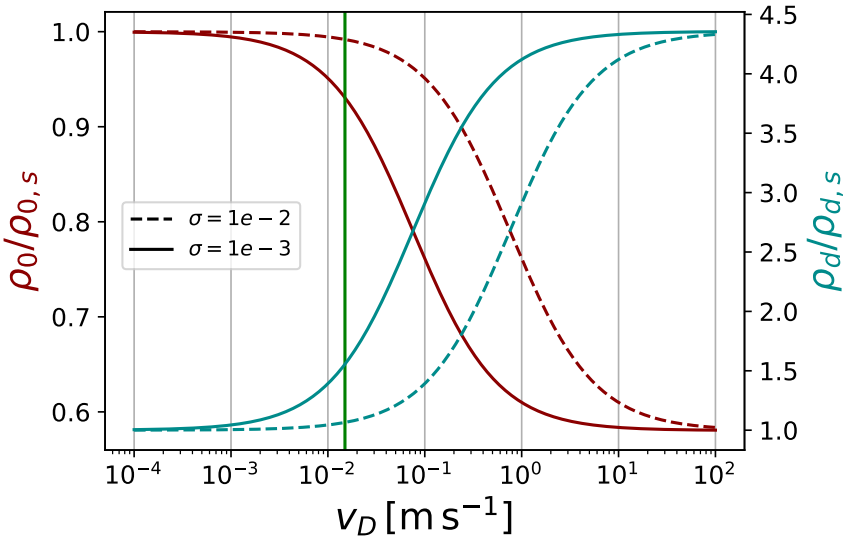

Figure 6.2: Saturation levels for different evaporation and condensation coefficients (σ_e and σ_c) and its dependence on v_D (logarithmic axis). In red the saturation level at the hot evaporation surface ($x = 0$) and in light blue the saturation level at the cold condensation surface ($x = d$). For this example we chose $\sigma_e = \sigma_c = \sigma$. The vertical green line indicates a $v_D = D/d = 1.5 \times 10^{-2}\,\mathrm{m/s}$.

v_D can be used to define two regimes where either diffusion (transport from evaporation to condensation surface) or evaporation is the limiting process for the vapour flux in the domain. For an intermediate v_D both process are relevant.

v_D is defined by the setup of the AGMD module. In a first approximation v_D can be calculated by $v_D = D/d$ where d is the width of the air–gap (and the membrane) and D the mean diffusivity in the air gap (and the membrane). A detailed discussion of the parameter v_D and its calculation can be found in chapter 2. Typical values for AGMD are $D = 3 \times 10^{-5}\,\mathrm{m^2\,s^{-1}}$ and $d = 2 \times 10^{-3}\,\mathrm{m}$ which results in $v_D = 1.5 \times 10^{-2}\,\mathrm{m/s}$ (see green line in figure 6.2).

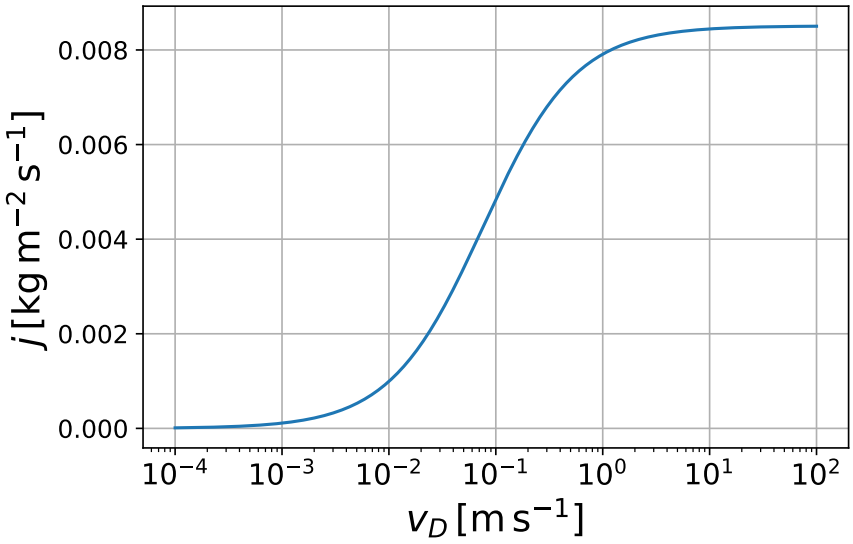

Figure 6.3: The flux in the domain for $\sigma = 10^{-3}$.

For our first study, we adopted uniform condensation and evaporation coefficients throughout the entire domain. Our findings suggest that for this specific setup with $v_D = 1.5 \times 10^{-2}\,\mathrm{m/s}$, saturation is likely to occur in the air gap throughout most areas for a typical AGMD setup, only a magnitude change of v_D would lead to a significant alteration in the saturation level on the evaporation boundary. To observe a substantially less saturated evaporation boundary, it is necessary to reduce the air gap by one order of magnitude or increase the diffusivity by one order of magnitude.

It is not guaranteed that the evaporation and condensation coefficients are equal [32], therefore in the following we investigate the impact of different values for evaporation and condensation coefficients and we chose $\sigma_{c,0} = \sigma_{c,d} = \sigma_c$ and $\sigma_{e,0} = \sigma_{e,d} = \sigma_e$.

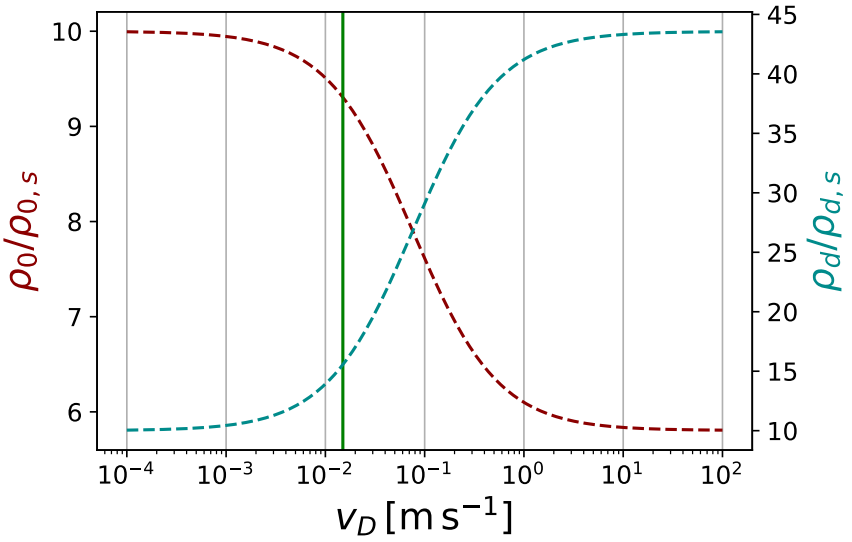

Figure 6.4: Saturation levels for $\sigma_e = 10^{-2}, \sigma_c = 10^{-3}$.

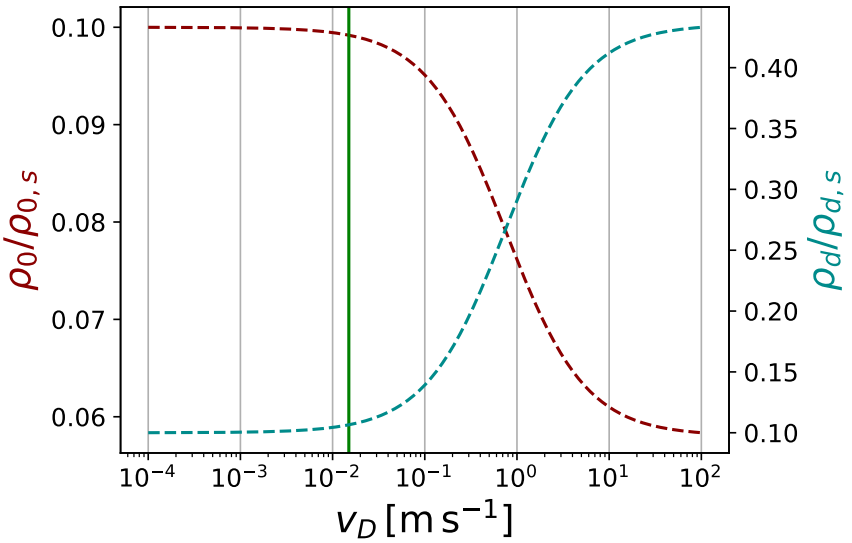

Figure 6.5: Saturation levels for $\sigma_e = 10^{-3}, \sigma_c = 10^{-2}$.

Based on the results shown in figure 6.4 and 6.5, one can see that the difference between evaporation and condensation coefficient has a big impact on the saturation level in the air–gap for the setup investigated here (green vertical line).

Following the results from [32] and [37], evaporation and condensation coefficients are supposed to vary with temperature, and experimental conditions (like flow and contamination). It is therefore possible that condensation and evaporation coefficients on both inter-

faces (at $x = 0$ and $x = d$) in the AGMD configuration might not be equal, resulting in a scenario shown in figure 6.6.

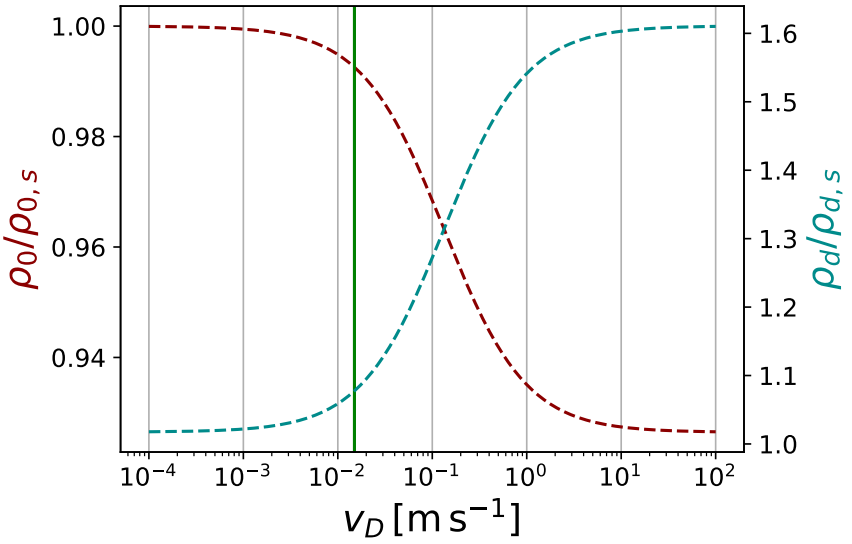

Figure 6.6: Saturation levels for $\sigma_{c,0} = 10^{-2}$, $\sigma_{e,0} = 10^{-2}$, $\sigma_{e,d} = 10^{-3}$ and $\sigma_{e,d} = 10^{-3}$.

6.3 DISCUSSION

Based on this very simple model and the obtained results, it can be concluded that the saturation level in the air–gap depends strongly on the magnitude of the condensation and evaporation coefficients. For the case where condensation and evaporation coefficients are equal at the evaporation and condensation interface one can conclude that the saturation level at the evaporation interface is larger than 90% for the full range of expected σ values (10^{-3} to 1) in the air gap for a v_D value typical for AGMD. As σ increases, the air vapor mixture gets closer to saturation at the evaporation interface. Therefore, if the evaporation and condensation coefficients are the same throughout the domain, full saturation of the air in the air gap is a reasonable assumption.

Since it is not guaranteed that the condensation and evaporation coefficients are equal the predictive power of the model derived in this chapter remains limited and only allows to give reasonable results if the condensation and evaporation coefficients have been determined prior by experiments. An additional weakness of the model presented in this chapter is that it uses a passive scalar model for diffusion neglecting complex multicomponent interactions and convection.

7 EVAPORATION INSIDE REALISTIC MEMBRANES

7.1 INTRODUCTION

In this chapter we investigate two different surface functionalizations for membranes. After determining the liquid–gas interface for a liquid film in contact with the functionalized membrane surface, we evaluate the effect of the liquid distribution on the magnitude of the evaporation flux. In total three different distributions are investigated, a membrane functionalized with hydrophilic/hydrophobic zoning, a membrane functionalized with micro pillars and an untreated membrane material as a reference. All membrane geometries are based on the 3D geometries of [10] presented in chapter 3.

7.2 MODEL PARAMETERS

In this chapter we utilise the multicomponent LB method and the evaporative bounce back boundary condition introduced in chapter 2 to model the evaporation and transport of vapor through the membrane. Species 1 represents the dry air and species 2 represents the water vapor in the binary gas mixture. Similar to the work of [39], the parameters given in table 7.1 were chosen to ensure the correct physical behavior for an air vapor mixture at about 60°C.

Table 7.1: Multi component LB model parameters in LB units.

Parameter name	**Variable**	**Value**
mass species 1	m_1	1.55
mass species 2	m_2	1.0
dynamic viscosity species 1	μ_1	0.075
dynamic viscosity species 2	μ_2	0.0375
diffusivity	D_{12}	0.1
HKS parameter	σ_e	0.2
initial density of the gas mixture	ρ_{init}	1.0
Schmidt number	Sc	$\approx 0.375 - 0.75$

Table 7.2: Relevant quantities in SI units for the binary gas mixture at $T = 333\,\mathrm{K}$.

Name	Variable	Value
lattice spacing (lu)	Δx	$39 \times 10^{-9}\,\mathrm{m}$
atmospheric pressure	p_{atm}	$101325.0\,\mathrm{Pa}$
saturation vapor pressure	p_{sat}	$20061.9\,\mathrm{Pa}$
saturation mole fraction of vapor	$X_{2,sat}$	0.198
dynamic viscosity	μ	$0.00002\,\mathrm{Pa\,s}$
kinematic viscosity	ν	$0.0000188\,\mathrm{m^2\,s^{-1}}$
diffusivity	D_{12}	$0.0000257\,\mathrm{m^2\,s^{-1}}$
Schmidt number	Sc	≈ 0.7315

The evaporation flux in LB units based on the Hertz–Knudsen–Schrage equation, is given by:

$$j_{evap} = \frac{2\sigma_e}{2-\sigma_e}\sqrt{\frac{m_v}{2\pi T k_B}}(p_{sat} - p_v)\frac{\mu_1}{\mu^{SI}}\Delta x^{SI} \tag{7.1}$$

Here $p_v = p_{atm} \times X_2^{inter}$ and X_2^{inter} denotes the mole fraction directly above the liquid interface.

It should be noted that the HKS evaporation coefficient σ_e was set to 0.2. This choice was arbitrary. The exact value of σ_e depends on the experimental setup (see the discussion in chapter 2), but in this study we only want to compare the effect of the water distribution on the magnitude of the evaporation flux. Since the rest of the conditions, such as the temperature, do not change, it makes sense to assume that σ_e is constant for the different water distributions, and it is reasonable to compare the simulation results among each other. The absolute value of the evaporation flux is not important.

$\Delta x^{SI}\mu_1/\mu^{SI} = 0.000146$ is the unit conversion factor from SI to LB units for the evaporation flux. To recover the correct flow the Schmidt number Sc has to match the actual physical problem, this ensures that the momentum diffusivity (kinematic viscosity) and mass diffusivity happen at a rate comparable to the actual physical problem.

$$\mathrm{Sc} = \frac{\nu}{D} = \frac{\mu}{\rho D} \tag{7.2}$$

This can be guaranteed by an appropriate choice of D and μ for the LB simulation (see table 7.1 and 7.2).

7.3 RESULTS

7.3.1 *Model Validation*

To validate the multicomponent LBM code and the evaporation BC described in chapter 2, we run two benchmarks. The first benchmark uses a geometry with a flat liquid–gas interface in the yz plane, defined by two layers of liquid voxels at $x = 96$ and $x = 97$, a layer of solid voxels at $x = 0\,\mathrm{lu}$ to close the domain, and PBC in the y and z directions (see figure 7.1). The total domain size is $98 \times 100 \times 100\,\mathrm{lu}^3$. This benchmark examines the conservation of mass for species 1 and the correct behavior at the BC.

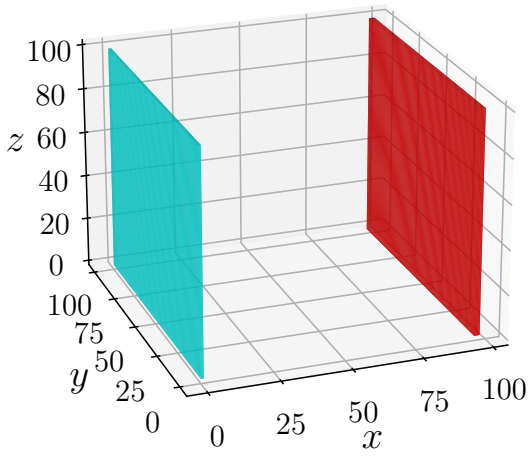

Figure 7.1: Domain of size $98 \times 100 \times 100\,\mathrm{lu}^3$ with a layer of solid voxels at $x = 0$ (in light blue) and two layers of liquid voxels at $x = 96$ and $x = 97$ (in red).

As described in chapter 2 the streaming step for the multi component LB method involves interpolation if the masses of the two species differ. To make sure that the interpolation for the streaming step works properly, we run the test for $m_1 = m_2 = 1$ (no interpolation) and $m_1 = 1.55$, $m_2 = 1$ (interpolation for species 1). The time evolution of the mole fraction X_j, the density ρ_j and the mass flux $j_j = \rho_j \times v_j$ are shown in the figures 7.2 and 7.4.

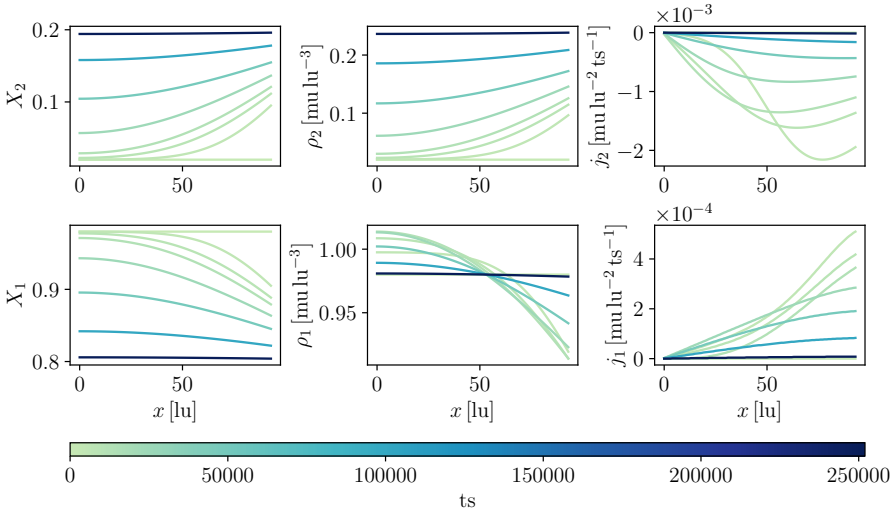

Figure 7.2: Time evolution of the mole fraction X_j, density ρ_j and mass flux $j_j = \rho_j \times v_j$ along the x–axis in a closed domain with evaporation at $x = 96$ lu and $m_1 = m_2 = 1$ (no interpolation).

As expected, the vapor (species 2) enters the domain with negative velocity due to the evaporation at $x = 96$. At the solid BC at $x = 0$ the velocity and the fluxes j_j are zero for both species. X_1 and X_2 are mirrored and add up to 1. ρ_2 increases with time in the whole domain. ρ_1 (vapor density) increases near the solid boundary and decreases near the evaporation interface, which is expected since the total mass for dry air (species 1) should remain constant over time. As time progresses, the solution converges to a constant gas distribution with zero velocity throughout the domain. The density distribution for the dry air (ρ_1) reaches its initial distribution and X_2 of the vapor converges to the saturation value $X_{sat} = 0.198$.

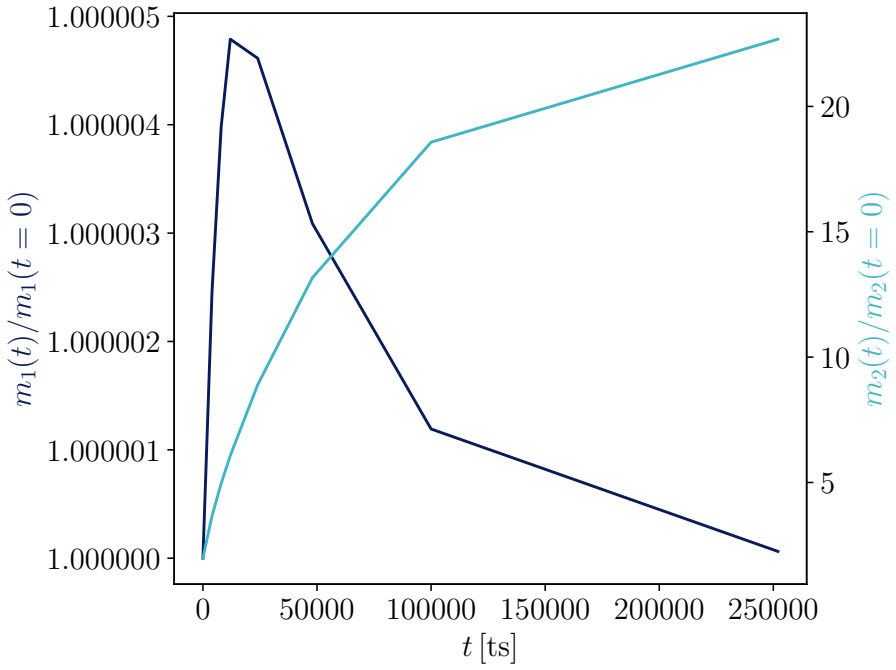

Figure 7.3: Total mass of species 1 and 2 in the domain as a function of time for the closed benchmark with equal species mass.

To verify that the mass of species 1 is conserved, we calculated the mass by integrating $\rho(x)$ over the entire domain and plotted the relative mass change as a function of time in figure 7.3, and found that the deviation was very small. Since the integral is calculated using Simpson's rule and is therefore not exact, that error is expected to be larger when the density distribution is far from equilibrium, as it is the case at the beginning of the simulation.

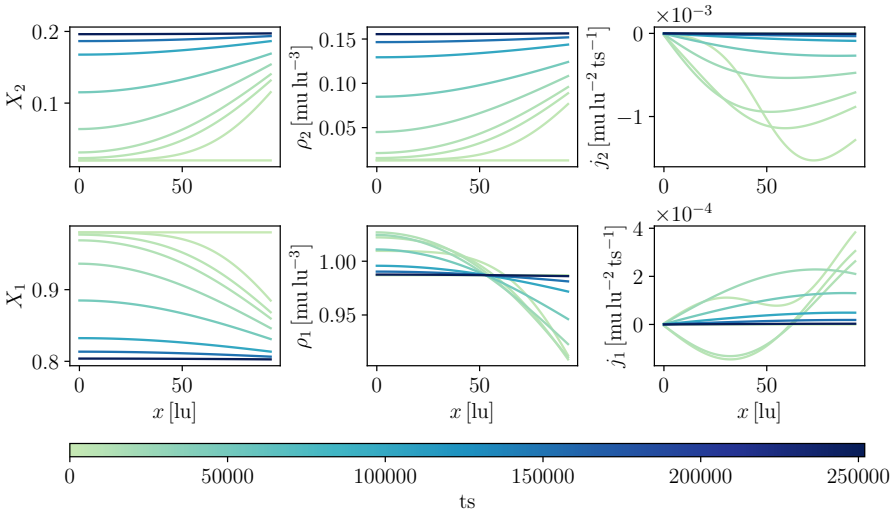

Figure 7.4: Time evolution of the mole fraction X_j, density ρ_j and mass flux $j_j = \rho_j \times v_j$ along the x-axis in a closed domain with evaporation at $x = 94\,\text{lu}$ and $m_1 = 1.55$, $m_2 = 1$ (interpolation for species 1).

After carefully choosing the BC for the interpolation, as described in chapter 2, the benchmark for $m_1 = 1.55$ and $m_2 = 1$ leads to a similar solution. The only notable difference is that j_1 becomes negative for the first part of the domain at the beginning of the simulation.

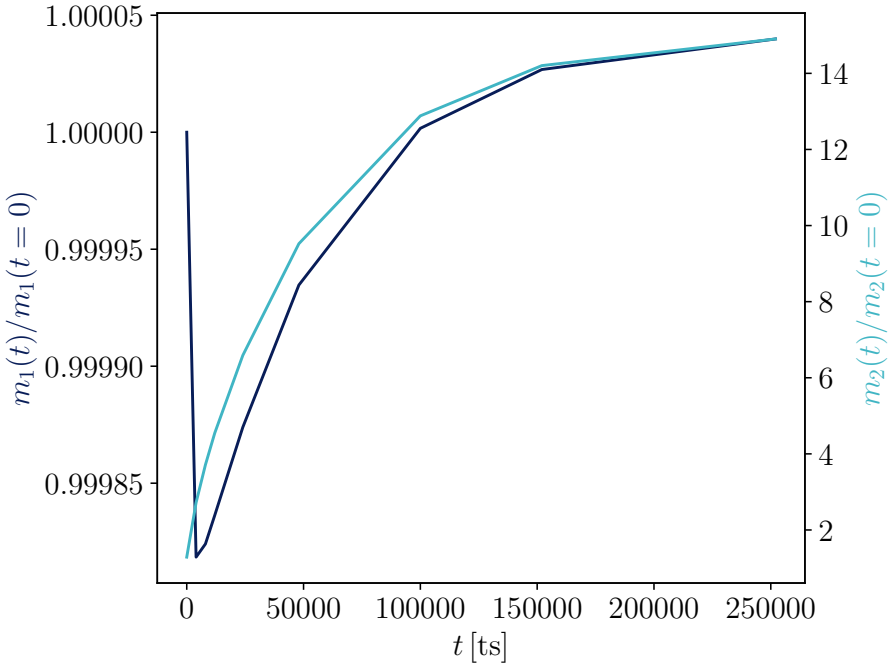

Figure 7.5: Total mass of species 1 and 2 in the domain as a function of the time for the closed benchmark.

Similar to the benchmark with equal mass, the total mass of species 1 only changed by small margin during the simulation for $m_1 = 1.55$ and $m_2 = 1$ (see figure 7.5).

Because of the solid BC at $x = 0$ in the first benchmark, the solution converged to a static state. To model the flow of a MD module correctly the simulation has to converge to a steady state solution, this can be achieved by an outflow BC with fixed outflow density as described in chapter 2. Therefore in a second benchmark we want to validate the correct implementation of the outflow BC. We used the same geometry and domain as shown in figure 7.1, but replaced the solid BC at $x = 0$ by an outflow BC with fixed densities for the two components at $x = 0$. This leads to the results shown in figures 7.6 and 7.7.

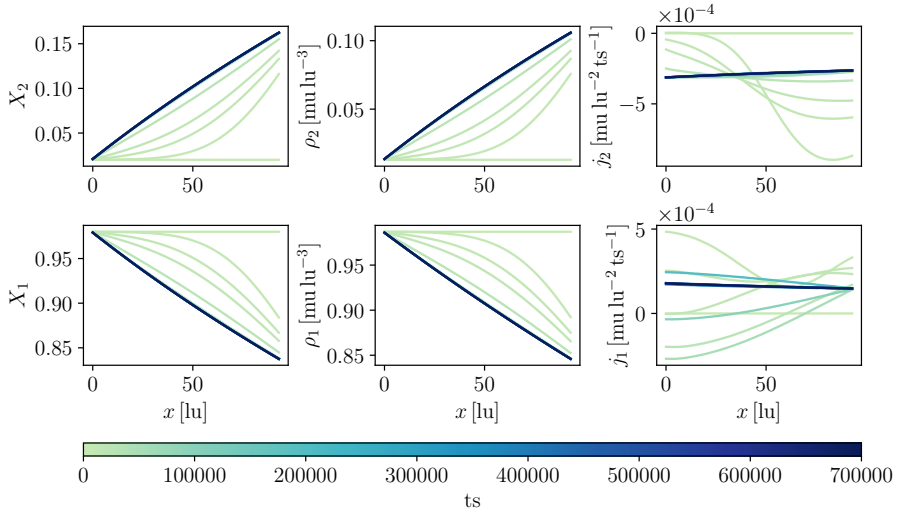

Figure 7.6: Time evolution of the mole fraction X_j, density ρ_j and mass flux $j_j = \rho_j \times v_j$ along the x-axis with evaporation at $x = 94$ lu, outflow at $x = 0$ and $m_1 = 1.55$, $m_2 = 1$ (with interpolation).

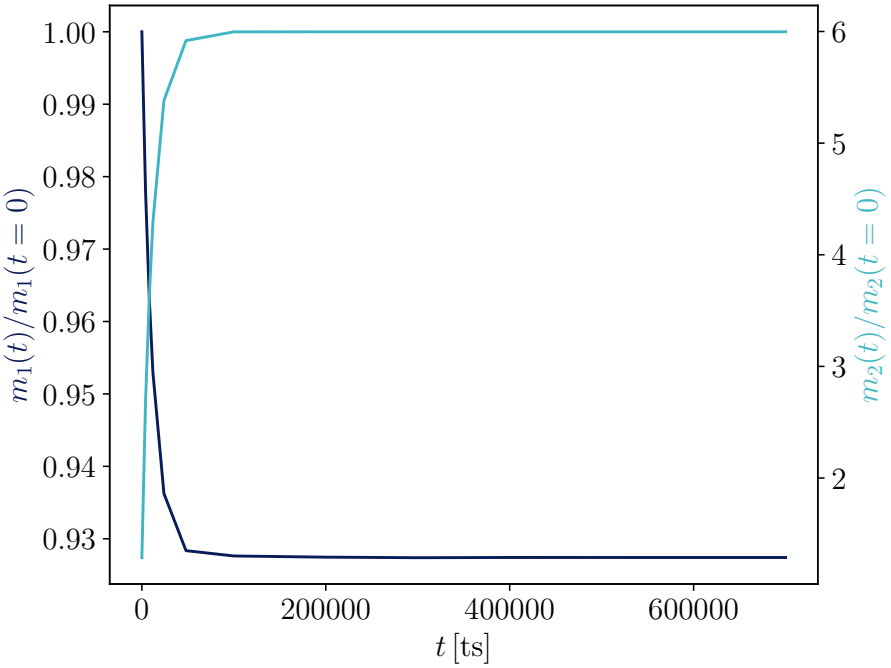

Figure 7.7: Total mass of species 1 and 2 in the domain as a function of the time for the outflow benchmark.

The momentum density injected into the domain at the evaporation boundary is equal to j_{HKS} from the Hertz–Knudsen–Schrage equation 7.1. Therefore, the total mass flux $j_{tot} = j_1 + j_2$ in the full domain should equal j_{HKS} at steady state. In the benchmark we found that j_{tot} oscillated around j_{HKS} and converged to it in a damped manner.

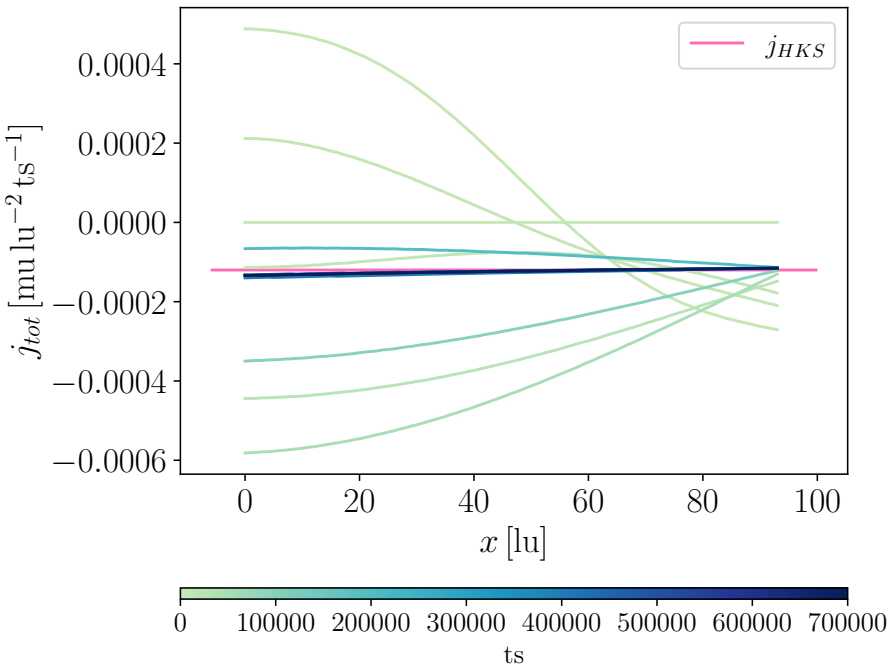

Figure 7.8: Time evolution of the total mass flux in the domain.

With $X_2^{inter} = X_2(x = 93)$, the mole fraction directly above the evaporation interface, one can use equation 7.1 to calculate j_{HKS}. After 700000 time steps we found $j_{HKS} = -0.00012$, which is also shown in figure 7.8. For the mean total flux we obtained $\bar{j}_{tot} = -0.00012$. Additionally one can use Fick's law to estimate the mass flux in the domain based on the gradient of ρ_2 and D_{12}:

$$\bar{j}_{2D,x} = -D_{12}\, mean\left(\frac{\rho_{2,x+1} - \rho_{2,x}}{1\,\mathrm{lu}}\right) \tag{7.3}$$

We found $\bar{j}_{1D,x} = -0.000099$, which has the same order of magnitude as j_{HKS} and $\bar{j}_{tot}$. Fick's law is only an approximation and the LB multi component code solves the more accurate Maxwell–Stephan equations including diffusion and convection. Therefore it is expected that $\bar{j}_{1D,x}$ is smaller than $\bar{j}_{tot}$ which also includes a convective term which is introduced by the evapoartion BC.

Since the correct σ_e values are unknown, we tested its influence on the total flux j_{tot} and on the diffusive flux $j_{D2,x}$.

Table 7.3: The influence of σ_e on the total flux j_{tot} and on the diffusive flux $j_{D2,x}$.

σ_e	0.05	0.2	0.8
j_{tot}	-0.73×10^{-4}	-1.2×10^{-4}	-1.7×10^{-4}
$j_{D2,x}$	-0.61×10^{-4}	-0.99×10^{-4}	-1.2×10^{-4}
$100\% \times j_{D2,x}/j_{tot}$	84%	82.5%	71%

7.3.2 *Evaporation and Vapor Transport in Realistic Membrane Geometries*

To determine the water distribution for a liquid film in contact with the three different geometries, we used the LB multiphase model introduced in chapter 3.

To realize zoning patterns with alternating stripes of hydrophobic and hydrophilic regions, we reduced the value of G_{ads} to $G_{ads} = -400$ for certain regions of the solid membrane geometry, the rest of the conditions are identical to those described in chapter 3. This results in regions with hydrophilic surface properties and equilibrium contact angles of about 65°. To ensure that the water does not penetrate the entire membrane, the hydrophilic zones are limited to a depth of 100 voxels (3.9 μm), the width of a stripe was set to 137 voxels (5.34 μm). Figure 7.9 shows a sketch of the zones, the resulting water distribution of the liquid film is shown in red in figure 7.10 (b).

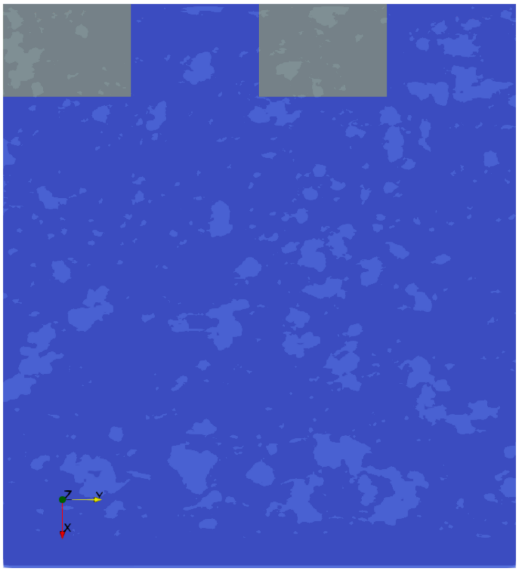

Figure 7.9: Slice at $z = 275\,\text{lu}$ through the 3D FHLP membrane geometry ($600 \times 550 \times 550\,\text{lu}^3$). Areas in gray represent the hydrophilic zones. Gas voxels are shown in dark blue and solid voxels are shown in light blue.

The pillars have a radius of $r_p = 20\,\text{lu}$, a heights $h_p = 100\,\text{lu}$ and a pillar distance $P = 110\,\text{lu}$. The pillars on top of the membrane geometry are shown in figure 7.10 (a). This pillar geometry was chosen in a way that the liquid does not move down the pillar walls for a pressure difference typically expected between liquid and gas for an AGMD module ($\Delta p = 0.182\,\text{bar}$).

To find the appropriate pillar geometry where the liquid remains at the elevated state, the formula in equation 7.4 developed by Zheng, Yu, and Zhao [52] can be used, which allows to calculate the critical pressure (liquid entry pressure) based on the pillar geometry and the

equilibrium contact angle; a detailed discussion of the formula can be found in chapters 4 and 5.

$$\Delta p_{crit}^{Zheng} = -\frac{\gamma 2\pi r_p \cos(\theta)}{P^2 - \pi r_p^2} \tag{7.4}$$

For a surface interaction strength of $G_{ads} = -80$ (parameter from the LB multiphase model which was discussed in chapter 3), which was chosen for the pillar geometry studied here, follows for the equilibrium contact angle $\alpha_0 = 156.61°$ and therefore with equation 7.4 $\Delta p < \Delta p_{crit}^{Zheng} = 0.201\,\text{bar}$. This ensured that the liquid did not slide down the pillars.

In addition, the pillar geometry presented here reduces the contact area between liquid and solid when the liquid remains in the elevated state. The liquid–solid contact area for the pillars ($A_{lp} = 100\% \times \pi r_p^2 / P^2 \approx 10\%$) is about half that of an untreated membrane, which is determined by the membrane porosity. The membrane studied here has a porosity of about 80% [10]. Therefore, the water–solid contact area for an untreated membrane can be estimated by $A_{lm} \approx 100\% - 80\% = 20\%$. A smaller liquid–solid contact area reduces the target surface for scaling and membrane fouling and is therefore beneficial.

After a static density distribution was reached for the LB multiphase simulations, we used the final state to create the new geometries for the multicomponent evaporation LB simulations. If the density was above ρ_c the voxel was set to an evaporation voxel of type 2 and if the density was below ρ_c the voxel remained a fluid voxel of type 0. For the untreated membrane and the membrane pillars $\rho_c = 150\,\text{mu}\,\text{lu}^{-3}$ and for the membarne with zoning $\rho_c = 540\,\text{mu}\,\text{lu}^{-3}$. This increase was necessary to properly recover the liquid–gas interface for the hydrophilic parts of the membrane and to be able to calculate the interface area.

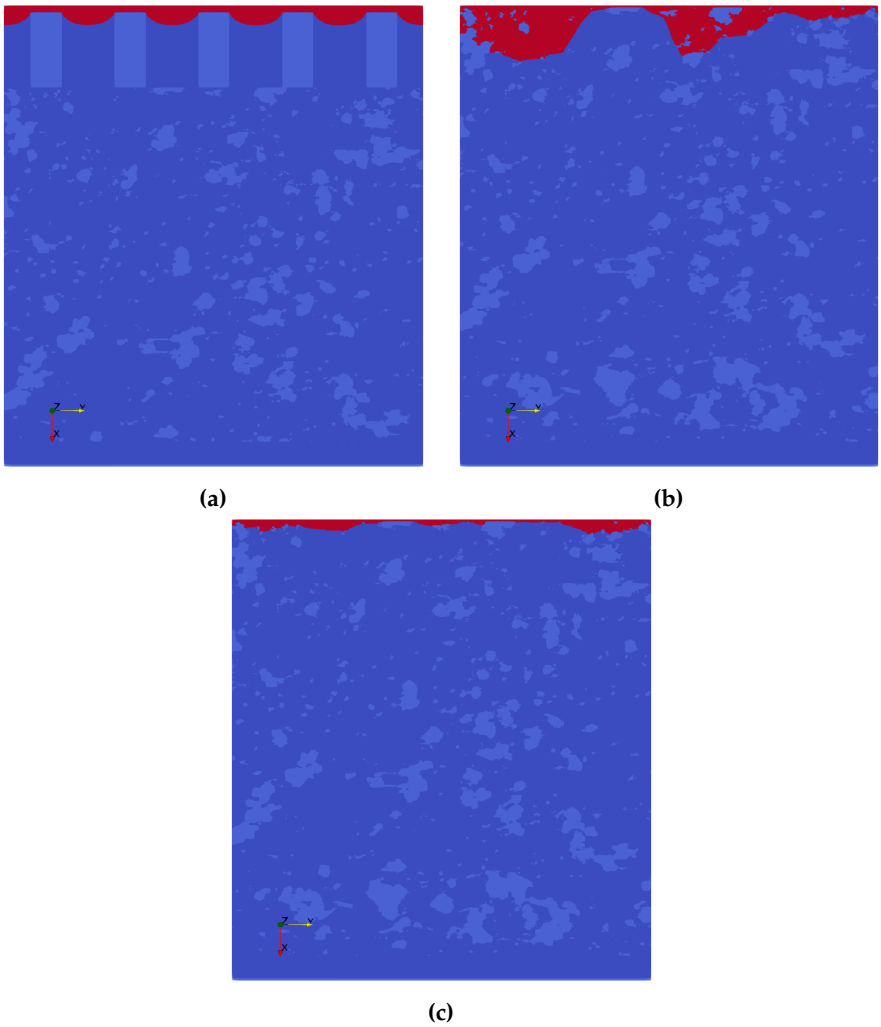

Figure 7.10: Slice at $z = 275\,\mathrm{lu}$ through the 3D FHLP membrane geometry ($600 \times 550 \times 550\,\mathrm{lu}^3$) with liquid distribution for pillars (a), zoning (b) and no treatment (c). Liquid boundary voxels in red, gas voxels in dark blue, solid boundary voxels in light blue.

Similar to the work in chapter 3, we used the marching cube algorithm to determine and calculate the liquid–gas interface surface area (see figure 7.11 and table 7.4). Hydrophilic/hydrophobic zoning and pillars both increased the liquid–gas surface area.

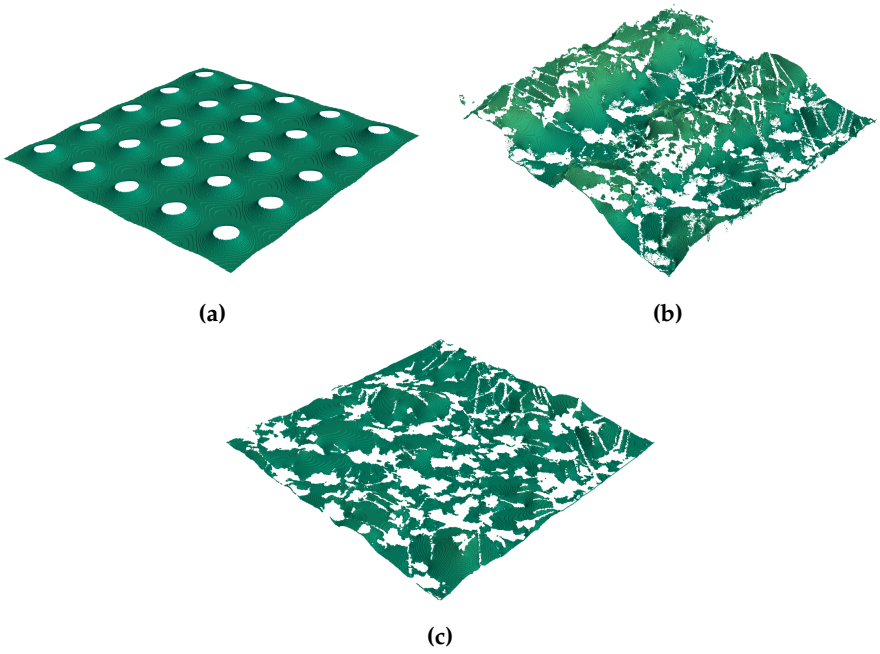

Figure 7.11: Liquid–gas interface for pillars (a), wave like interface due to the zoning (b) and interface for no treatment (c), obtained with the marching cube algorithm. White spots indicate the contact area of liquid and membrane material.

Table 7.4: Liquid–gas interface surface area, calculated with the marching cube algorithm.

	No treatment	**Zoning**	**Pillars**
liquid–gas surface area [lu^2]	264422.94	354830.78	319135.0

With the large geometries prepared and consideration given to the different water distributions due to the surface treatment (see figure 7.10), the multicomponent code presented in chapter 2 can now be utilized to calculate the evaporation flux for all three water distributions. Similar to the setup in the benchmark where we tested the outflow BC, a multicomponent outflow condition with fixed species densities ($\rho_{1,out} = 0.987\,\mathrm{mu\,lu^{-3}}$ and $\rho_{2,out} = 0.013\,\mathrm{mu\,lu^{-3}}$) was established at the bottom of each domain. This setup will converge towards a steady state solution and allows to evaluate for which geometry the biggest distilled water flux can be reached. In addition to the outflow BC, a layers consisting of 30 fluid voxels has been added below the membrane geometry (see figure 7.12).

The vapour flux in the x–direction $j_{2,x}$ represents the distilled water flux and is the one that should be maximized in order to gain the most fresh water.

The distilled water flux leaving the membrane at the bottom side, can be calculated by averaging $j_{2,x}$ over the layer of fluid voxels be-

tween the outflow and the membrane geometry (see figure 7.13 and 7.12). It holds: $\bar{j}_{2,x} = mean(\rho_2 \times v_{2,x})$.

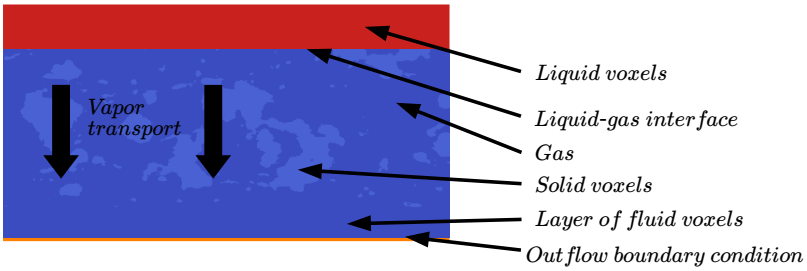

Figure 7.12: Sketch of the simulation setup. Liquid boundary voxels in red, gas voxels in dark blue, solid boundary voxels (membrane material) in light blue and an outflow BC with fixed densities for both species at the bottom side of the domains.

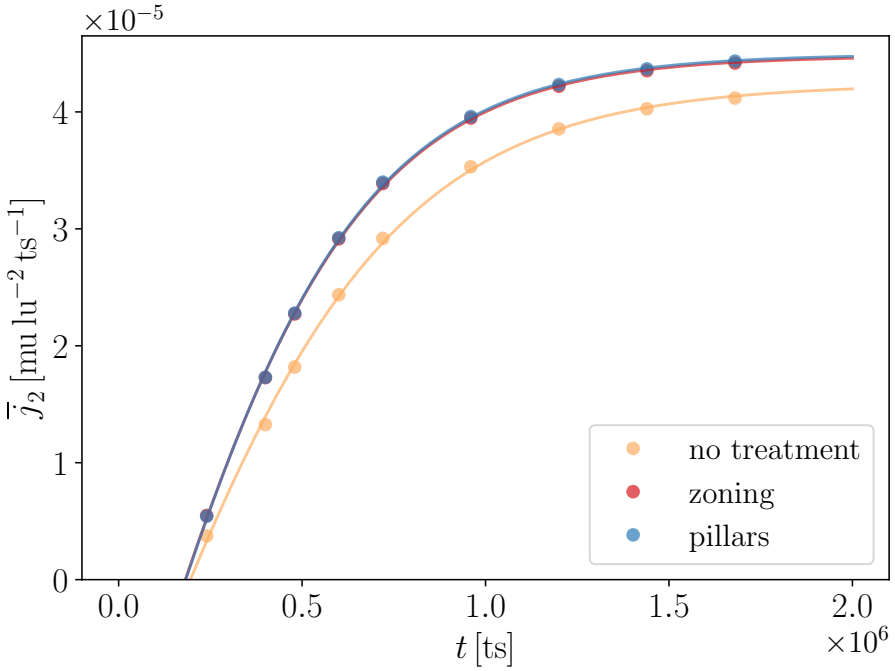

Figure 7.13: The observed vapor flux leaving the membrane at the bottom side. And the fits of equation 7.5.

To quantify the vapor flux $\bar{j}_{2,x}$ at steady state $\bar{j}_{2,x,\infty}$ $(t \to \infty)$ we plotted the observed $\bar{j}_{2,x}$ from the simulations against the time t and fitted the function given in equation 7.5. The tanh models an asymptotic behavior. For $t \to \infty$ follows $\bar{j}_{2,x} \to p_0 + p_2$. The resulting steady–state vapor fluxes are listed in table 7.5.

$$\bar{j}_{2,x}(t) = p_0 \times \tanh(p_1 \times t) + p_2 \tag{7.5}$$

Table 7.5: Steady state vapor fluxes between membrane and outflow.

	No treatment	**Zoning**	**Pillars**
p_0	5.783×10^{-5}	6.265×10^{-5}	6.306×10^{-5}
p_1	0.140×10^{-5}	0.161×10^{-5}	0.162×10^{-5}
p_2	-1.544×10^{-5}	-1.786×10^{-5}	-1.811×10^{-5}
$\bar{j}_{2,x,\infty} = p_0 + p_2$	4.239×10^{-5}	4.479×10^{-5}	4.494×10^{-5}
	-	(+5.7%)	(+6.0%)

$j_{2,x}$ is the mass flux of the vapor, including a convective and a diffusive part. The magnitude of the diffusive part $j_{D2,x}$ can be estimated by using equation 7.3. Similarly, $\bar{j}_{1,x}$ and $\bar{j}_{D1,x}$ can be calculated. Figure 7.14 shows the fluxes resulting from the different water distributions as a function of t.

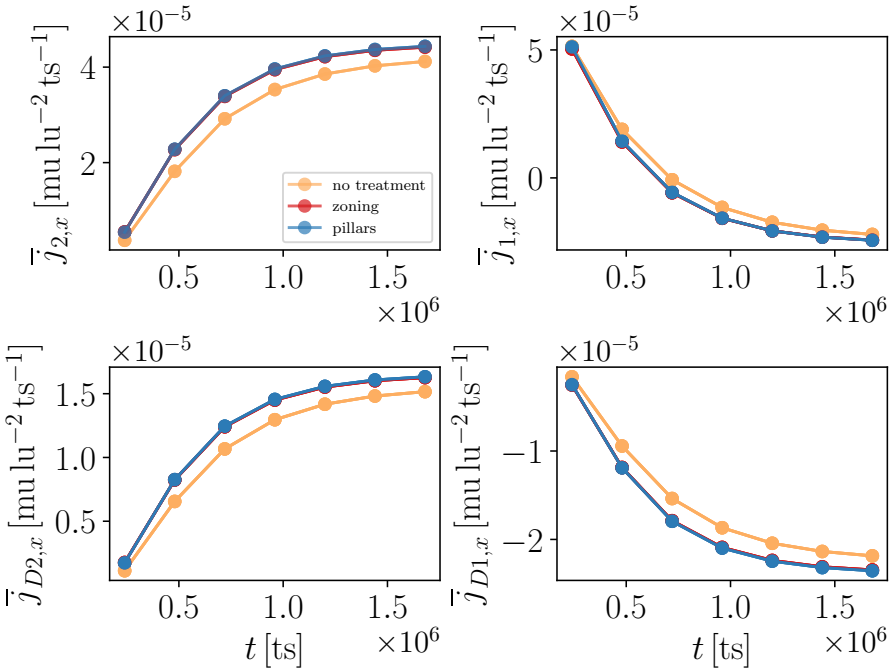

Figure 7.14: The observed evaporation fluxes in the fluid layer at the bottom of the domain between the membrane structure and the outflow BC for the different water distributions.

For the condition and setup investigated in this work we can infer that zoning and pillars can increase the vapour flux and therefore improve the performance of the MD module (see table 7.5 and figure 7.13 and 7.14). Furthermore the convective part of the vapor flux has an important contribution to vapour flux $j_{2,x}$, since $j_{2,x}$ is more than double of $j_{D2,x}$.

7.4 DISCUSSION

Based on the findings presented in figure 7.13 and 7.14, it can be inferred that the different water distributions due to surface treatment (zoning or pillars) have a significant effect on the magnitude of the evaporation flux. Over the course of the simulation, the integration of a hydrophilic/hydrophobic zoning pattern and the implementation of pillars led both to a similar rise in the magnitude of the evaporation flux as compared to an untreated membrane. At steady state we found an increase of 5.7% for the zoning and 6.0% for the pillars. These results show that a positive correlation between the available liquid–gas surface area and the magnitude of the evaporation flux exists even for intricate porous membrane structures (see table 7.4). It is surprising to find a similar flux for the hydrophilic/hydrophobic zoning and the pillar structure since the interface area is different (see table 7.4). A possible explanation could be that the orientation of the interface, which is different for the pillars and the zoning (compare 7.11 (a) and (b)), also influences the magnitude of the evaporation flux. Another explanation could be that the interface area for the zoning was overestimated. Due to the hydrophilic zoning the interface was not anymore a nice continuous interface as for the pillars or the untreated liquid interface, but also consisted of very small isolated droplets. Such isolated droplets often consist of only a few voxels and complicate an accurate interface area calculation with the marching cube algorithm and could have led to an overestimation of the liquid–gas interface, i.e. the actual interface might be smaller for the zoning case.

8

CONCLUSION

The separation mechanism for pure water from saline or brackish water in the context of AGMD is based on evaporation and diffusive transport. During this process, the saline or brackish water is in contact with a hydrophobic membrane. When optimizing the design of AGMD modules, the focus is typically on the overall structure and arrangement of the membrane and the air gap. Since little is known about the underlying mechanisms at the pore scale and experiments at the pore level are complicated, in–depth modeling of the separation process is desirable.

To address this research question, the work was divided into two parts, which are both crucial for a deeper understanding of the separation process. The first part investigated the interaction between the hydrophobic membrane material and the liquid phase (water) at pore level, using a LB multiphase model. The second part of this study investigated the effects of varying water distribution on the magnitude of the evaporation flux passing through the membrane. Maximizing the evaporation flux is important because it will increase the efficiency of the MD module.

The interface shape of a pressurized liquid in contact with a hydrophobic material is described by the Young–Laplace equation and a surface of constant mean curvature. An analytical solution to this problem exists for only a few basic geometries. For a complex geometry such as the porous structure of the membrane, numerical modeling is required. Based on various tests and benchmarks, we can conclude that the multiphase pseudo potential LB model is a suitable model to investigate the shape of the liquid–gas interface, as it natively supports the inclusion of complex rough BC and an interaction between fluid and solid. For example, in chapter 3 we found good agreement with the liquid entry pressure (LEP) observed in experiments compared to our multiphase simulations. Among other things, the LEP is an important membrane characteristic, but also plays an important role in microfluidics and biochemical analysis. For many applications in this context it is relevant to retain liquids behind or within rough structures, such as for example a pillar–pore structure.

There is an exact formula available for determining the LEP of basic structures including cylindrical and toroidal pores. In chapter 4, we conducted a theoretical analysis of the constant mean curvature problem in cases of rotational symmetry. This analysis allowed us to determine an analytical expression for the liquid entry pressure of a hydrophobic pillar–pore structure, as well as the shape of the liquid–

gas interface and the location of its minimum. The presented pillar–pore structure can also serve as a benchmark for the development and validation of numerical multiphase models. We found good agreement between the analytical solution and multiphase LB simulations for the interface shape.

In another study in chapter 3, we observed an agglomeration of water droplets in membrane regions of high porosity when water vapor condenses inside the membrane structure. This can be beneficial for the design of future membranes, as a gradient in porosity could facilitate the transport of water through the membrane and prevents a pore blockage in the center of the membrane. We also investigated the liquid gas interface of a liquid film in contact with the hydrophobic membrane material and found in chapter 3 and 7 that for an untreated membrane the liquid–gas interface area is prescribed by the porosity.

In our work in chapter 5, we analyzed the stability and energy barrier of droplets in the Cassie–Baxter state on such periodic patterns. In addition, we further developed the transition criterion from Patankar [30] and derived an improved version which allows predicting for which pillar geometries, equilibrium contact angles and droplet volumes the Cassie–Baxter state switches from a meta stable to an unstable state. This enables a comparison with existing experiments and 3D multiphase Lattice Boltzmann simulations for different pillar geometries and equilibrium contact angles, where a good agreement has been found.

Another research question we addressed was the question of what partial vapor pressure (level of saturation) can be expected in the membrane and air gap. In chapter 6 we tried to answer this question using a simple evaporation model based on the Hertz–Knudsen equation and a diffusive transport in the air gap. It turned out that this model is insufficient to answer this question, since the solution depends strongly on the evaporation and condensation coefficients, which differ by up to three orders of magnitude from setup to setup, making a general answer difficult. If these coefficients are known from previous experiments and diffusive transport is the dominant transport phenomenon, this model can be used. To address this question, one needs to use a combined multiphase–multicomponent code which resolves the full air gap, the porous membrane structure and includes a condensation and evaporation model similar to the one presented by [36]. The benefit of this approach is that the evaporation interface is handled dynamically allowing non static liquid gas interfaces to be modeled. Such a model allows to answer in detail the question under which conditions full saturation in the air gap is a reasonable assumption. The challenge with this approach is that the standard LB implementation requires the air gap and the membrane to be resolved at the same resolution, which dramatically increases the total number of voxels. This is because the air gap is much larger than the diameter

of the membrane. Therefore, either much more computing power is needed or one would need to implement a LB method that can handle different grid resolutions within the domain.

In chapter 7 we investigated the influence of different water distributions on the evaporation flux using a multi component LB method with an evaporation BC based on the Hertz–Knudsen–Schrage equation. Three different water distributions resulting from an untreated membrane material, hydrophilic/hydrophobic zoning and a periodically repeated pillar structure were tested.

We found that surface functionalization, either through hydrophilic–hydrophobic zoning or a pillar structure, can increase the liquid–gas interface area. Based on our findings, it can be concluded that the distribution of water and the liquid–gas interface area have a significant effect on the magnitude of the evaporation flux. Over the course of the simulation, the integration of a hydrophilic/hydrophobic zoning pattern and the implementation of pillars led to a rise in the magnitude of the evaporation flux compared to an untreated membrane. These results suggest that there is a positive correlation between the available liquid–gas surface area, which was higher for the zoning and the pillars compared to the untreated membrane, and the magnitude of the evaporation flux. Both treatments resulted in a similar increase in the vapour flux. The pillar structure has the additional advantage to reduced scaling effects where as the hydrophilic/hydrophobic zoning pattern has the benefit of being easier to fabricate. Furthermore, the results indicate that the momentum injected into the domain due to the evaporation can have a significant impact on the total flux and should be considered when modelling AGMD process.

In summary, based on the results presented in this work, the LB method is a viable method to model MD processes at the pore scale. The models in our work were limited to an isothermal flow and a static liquid–gas interface for the evaporation and transport model. The multiphase model used in this work is limited to small density ratios between liquid phase and gas phases (of order 10 to 20), which becomes problematic when simulating non–stationary dynamic flow at high Reynolds numbers. Future work should therefore aim to apply more complex multi relaxation time non–isothermal lattice Boltzmann methods, which include heat transport, a non–static liquid–gas interface and allow to model flow at high density ratios. Such models do exist, but are more complicated to implement and parallelize in order to run efficiently on geometries of the size investigated within this work.

BIBLIOGRAPHY

[1] Damena D. Agonafer et al. "Porous micropillar structures for retaining low surface tension liquids." In: *Journal of Colloid and Interface Science* 514 (2018), pp. 316–327. ISSN: 0021-9797. DOI: 10.1016/j.jcis.2017.12.011. URL: https://www.sciencedirect.com/science/article/pii/S0021979717314017.

[2] Ali Al-Karaghouli and Lawrence L. Kazmerski. "Energy consumption and water production cost of conventional and renewable-energy-powered desalination processes." In: *Renewable and Sustainable Energy Reviews* 24 (2013), pp. 343 –356. ISSN: 1364-0321. DOI: 10.1016/j.rser.2012.12.064. URL: http://www.sciencedirect.com/science/article/pii/S1364032113000208.

[3] Abdullah Alkhudhiri, Naif Darwish, and Nidal Hilal. "Membrane distillation: A comprehensive review." In: *Desalination* 287 (2012), pp. 2 –18. ISSN: 0011-9164. DOI: 10.1016/j.desal.2011.08.027. URL: http://www.sciencedirect.com/science/article/pii/S0011916411007284.

[4] A.S. Alsaadi, N. Ghaffour, J.-D. Li, S. Gray, L. Francis, H. Maab, and G.L. Amy. "Modeling of air-gap membrane distillation process: A theoretical and experimental study." In: *Journal of Membrane Science* 445 (2013), pp. 53–65. ISSN: 0376-7388. DOI: https://doi.org/10.1016/j.memsci.2013.05.049. URL: https://www.sciencedirect.com/science/article/pii/S0376738813004705.

[5] S. Arcidiacono, I. V. Karlin, J. Mantzaras, and C. E. Frouzakis. "Lattice Boltzmann and model for the simulation of multicomponent mixtures." In: *PHYSICAL REVIEW E* (2007).

[6] R. Byron Bird, Warren E. Stewart, and Edwin N. Lightfoot. *Transport Phenomena*. Wiley, 2006, p. 920. ISBN: 9780470115398.

[7] Florian Carle and David Brutin. "Chapter 9 - Convection." In: *Droplet Wetting and Evaporation*. Ed. by David Brutin. Oxford: Academic Press, 2015, pp. 115–128. ISBN: 978-0-12-800722-8. DOI: https://doi.org/10.1016/B978-0-12-800722-8.00009-6. URL: https://www.sciencedirect.com/science/article/pii/B9780128007228000096.

[8] S. Chapman and T.G. Cowling. *The mathematical Theory of Non-Uniform Gases*. Cambridge University Press, 1952.

[9] Qian Chen, Muhammad Burhan, Faheem Hassan Akhtar, Doskhan Ybyraiymkul, Muhammad Wakil Shahzad, Yong Li, and Kim Choon Ng. "A decentralized water/electricity cogeneration system integrating concentrated photovoltaic/thermal collectors and vacuum multi-effect membrane distillation." In: *Energy* 230 (2021), p. 120852. ISSN: 0360-5442. DOI: 10.1016/j.energy.2021.120852. URL: https://www.sciencedirect.com/science/article/pii/S0360544221011002.

[10] Kerstin Cramer, Nikolaos I. Prasianakis, Bojan Niceno, Johannes Ihli, and Stephan Leyer. "Three-Dimensional Membrane Imaging with X-ray Ptychography: Determination of Membrane Transport Properties for Membrane Distillation." In: *Transport in Porous Media* (2021).

[11] Jhon Jairo Feria-Díaz, María Cristina López-Méndez, Juan Pablo Rodríguez-Miranda, Luis Carlos Sandoval-Herazo, and Felipe Correa-Mahecha. "Commercial Thermal Technologies for Desalination of Water from Renewable Energies: A State of the Art Review." In: *Processes* 9.2 (2021). ISSN: 2227-9717. DOI: 10.3390/pr9020262. URL: https://www.mdpi.com/2227-9717/9/2/262.

[12] Andrew K. Gunstensen, Daniel H. Rothman, Stéphane Zaleski, and Gianluigi Zanetti. "Lattice Boltzmann model of immiscible fluids." In: *Phys. Rev. A* 43 (8 1991), pp. 4320–4327. DOI: 10.1103/PhysRevA.43.4320. URL: https://link.aps.org/doi/10.1103/PhysRevA.43.4320.

[13] Baek-Gyu Im, Jung-Gil Lee, Young-Deuk Kim, and Woo-Seung Kim. "Theoretical modeling and simulation of AGMD and LGMD desalination processes using a composite membrane." In: *Journal of Membrane Science* 565 (2018), pp. 14–24. ISSN: 0376-7388. DOI: https://doi.org/10.1016/j.memsci.2018.08.006. URL: https://www.sciencedirect.com/science/article/pii/S0376738818311104.

[14] Abhijit S Joshi, Aldo A Peracchio, Kyle N Grew, and Wilson K S Chiu. "Lattice Boltzmann method for multi-component, non-continuum mass diffusion." In: *Journal of Physics D: Applied Physics* 40.23 (2007), pp. 7593–7600. DOI: 10.1088/0022-3727/40/23/053. URL: https://doi.org/10.1088%2F0022-3727%2F40%2F23%2F053.

[15] Y Jung and Bharat Bhushan. "Wetting behaviour during evaporation and condensation of water microdroplets on superhydrophobic patterned surfaces." In: *Journal of microscopy* 229 (Feb. 2008), pp. 127–40. DOI: 10.1111/j.1365-2818.2007.01875.x.

[16] Tobias Jäger, Athanasios Mokos, Nikolaos I. Prasianakis, and Stephan Leyer. "Pore-Level Multiphase Simulations of Realistic Distillation Membranes for Water Desalination." In: *Membranes*

12.11 (2022). ISSN: 2077-0375. DOI: 10.3390/membranes12111112. URL: https://www.mdpi.com/2077-0375/12/11/1112.

[17] Ehsan Karbasi, Javad Karimi-Sabet, Jamshid Mohammadi-Rovshandeh, Mohammad Ali Moosavian, Hossein Ahadi, and Younes Amini. "Experimental and numerical study of air-gap membrane distillation (AGMD): Novel AGMD module for Oxygen-18 stable isotope enrichment." In: *Chemical Engineering Journal* 322 (2017), pp. 667–678. ISSN: 1385-8947. DOI: https://doi.org/10.1016/j.cej.2017.03.031. URL: https://www.sciencedirect.com/science/article/pii/S1385894717303698.

[18] Horst-Michael Prasser Kerstin Cramer Bojan Niceno and Stephan Leyer. "A three-dimensional model for the heat and mass transfer in air-gap membrane distillation." In: *Desalination and Water Treatment* (2021). DOI: 10.5004/dwt.2021.27775.

[19] M. Khayet, Paz Godino, and J. Mengual. "Modelling Transport Mechanism Through A Porous Partition." In: *Journal of Non-equilibrium Thermodynamics - J NON-EQUIL THERMODYN* 26 (Jan. 2001), pp. 1–14. DOI: 10.1515/JNETDY.2001.001.

[20] Timm Krüger, Halim Kusumaatmaja, Alexandr Kuzmin, Orest Shardt, Goncalo Silva, and Erlend Magnus Viggen. *The Lattice Boltzmann Method*. 2017.

[21] Josef Kunes. *Dimensionless Physical Quantities in Science and Engineering*. Elsevier Scientific Pub. Co Amsterdam ; New York, 2012.

[22] Emad Pouryazdanpanah Leila Jahanshaloo and Nor Azwadi Che Sidik. "A Review on the Application of the Lattice Boltzmann Method for Turbulent Flow Simulation." In: *Numerical Heat Transfer, Part A: Applications* 64.11 (2013), pp. 938–953. DOI: 10.1080/10407782.2013.807690. eprint: https://doi.org/10.1080/10407782.2013.807690. URL: https://doi.org/10.1080/10407782.2013.807690.

[23] Q. Li, K.H. Luo, Q.J. Kang, Y.L. He, Q. Chen, and Q. Liu. "Lattice Boltzmann methods for multiphase flow and phase-change heat transfer." In: *Progress in Energy and Combustion Science* 52 (2016), pp. 62 –105. ISSN: 0360-1285. DOI: 10.1016/j.pecs.2015.10.001. URL: http://www.sciencedirect.com/science/article/pii/S0360128515300162.

[24] K.H. Luo, J. Xia, and E. Monaco. "Multiscale modelling of multiphase flow with complex interactions." In: *Journal of Multiscale Modelling* 1.1 (Jan. 2009), pp. 125–156. URL: https://eprints.soton.ac.uk/69189/.

[25] A. Mazloomi M, S. S. Chikatamarla, and I. V. Karlin. "Entropic Lattice Boltzmann Method for Multiphase Flows." In: *Phys. Rev. Lett.* 114 (17 2015), p. 174502. DOI: 10.1103/PhysRevLett.114.174502. URL: https://link.aps.org/doi/10.1103/PhysRevLett.114.174502.

[26] Mesfin M. Mekonnen and Arjen Y. Hoekstra. "Four billion people facing severe water scarcity." In: *Science Advances* 2.2 (2016). DOI: 10.1126/sciadv.1500323.

[27] United Nations. *Water scarcity*. Accessed: 2023-05-19. URL: https://www.unwater.org/water-facts/water-scarcity.

[28] United Nations. *UN-Water Annual Report 2007*. 2007. URL: https://www.unwater.org/publications/un-water-annual-report-2007.

[29] Kim Choon Ng, Muhammad Burhan, Qian Chen, Doskhan Ybyraiymkul, Faheem Hassan Akhtar, M. Kumja, Robert W. Field, and Muhammad Wakil Shahzad. "A thermodynamic platform for evaluating the energy efficiency of combined power generation and desalination plants." In: *npj Clean Water* 4.1 (2021), p. 25. ISSN: 2059-7037. DOI: 10.1038/s41545-021-00114-5. URL: https://doi.org/10.1038/s41545-021-00114-5.

[30] Neelesh A. Patankar. "Consolidation of Hydrophobic Transition Criteria by Using an Approximate Energy Minimization Approach." In: *Langmuir* 26.11 (2010). PMID: 20158175, pp. 8941–8945. DOI: 10.1021/la9047424. eprint: https://doi.org/10.1021/la9047424. URL: https://doi.org/10.1021/la9047424.

[31] Aaron H. Persad. "Statistical Rate Theory Expression for Energy Transported during Evaporation." PhD thesis. Toronto, Canada: Mechanical and Industrial Engineering University of Toronto, 2014.

[32] Aaron H. Persad and Charles A. Ward. "Expressions for the Evaporation and Condensation Coefficients in the Hertz-Knudsen Relation." In: *Chemical Reviews* 116.14 (2016). PMID: 27314250, pp. 7727–7767. DOI: 10.1021/acs.chemrev.5b00511. eprint: https://doi.org/10.1021/acs.chemrev.5b00511. URL: https://doi.org/10.1021/acs.chemrev.5b00511.

[33] Melissa Petruzzello. *Water scarcity*. Accessed: 2023-05-24. URL: https://www.britannica.com/topic/water-scarcity.

[34] Roger Peyret and Thomas D. Taylor. *Computational Methods for Fluid Flow*. Springer, 1983.

[35] N. I. Prasianakis, I. V. Karlin, J. Mantzaras, and K. B. Boulouchos. "Lattice Boltzmann method with restored Galilean invariance." In: *Computational methods in fluid dynamics, Kinetic theory* (2009). DOI: 10.1103/PhysRevE.79.066702.

[36] Feifei Qin, Luca Del Carro, Ali Mazloomi Moqaddam, Qinjun Kang, Thomas Brunschwiler, Dominique Derome, and Jan Carmeliet. "Study of non-isothermal liquid evaporation in synthetic micro-pore structures with hybrid lattice Boltzmann model." In: *Journal of Fluid Mechanics* 866 (2019), 33–60. DOI: 10.1017/jfm.2019.69.

[37] J. Straub R. Marek. "Analysis of the evaporation coefficient and the condensation coefficient of water." In: *International Journal of Heat and Mass Transfer* 44 (2001), pp. 39–53.

[38] Rasha B. Saffarini, Edward K. Summers, Hassan A. Arafat, and John H. Lienhard V. "Economic evaluation of stand-alone solar powered membrane distillation systems." In: *Desalination* 299 (2012), pp. 55–62. ISSN: 0011-9164. DOI: 10.1016/j.desal.2012.05.017. URL: https://www.sciencedirect.com/science/article/pii/S0011916412002779.

[39] Mohammad Amin Safi, John Mantzaras, Nikolaos I. Prasianakis, Adrien Lamibrac, and Felix N. Büchi. "A pore-level direct numerical investigation of water evaporation characteristics under air and hydrogen in the gas diffusion layers of polymer electrolyte fuel cells." In: *International Journal of Heat and Mass Transfer* 129 (2019), pp. 1250–1262. ISSN: 0017-9310. DOI: 10.1016/j.ijheatmasstransfer.2018.10.042. URL: https://www.sciencedirect.com/science/article/pii/S0017931018324979.

[40] Ulf D. Schiller, Timm Krüger, and Oliver Henrich. "Mesoscopic modelling and simulation of soft matter." In: *Soft Matter* 14.1 (2018), pp. 9–26. DOI: 10.1039/c7sm01711a.

[41] X Shan and H Chen. "Simulation of nonideal gases and liquid-gas phase transitions by the lattice Boltzmann equation." In: *Physical Review. E, Statistical Physics, Plasmas, Fluids, and Related Interdisciplinary Topics; (United States)* (Apr. 1994). ISSN: 1063-651X. DOI: 10.1103/PhysRevE.49.2941. URL: https://www.osti.gov/biblio/5020512.

[42] Xiaowen Shan and Hudong Chen. "Lattice Boltzmann model for simulating flows with multiple phases and components." In: *Phys. Rev. E* 47 (3 1993), pp. 1815–1819. DOI: 10.1103/PhysRevE.47.1815. URL: https://link.aps.org/doi/10.1103/PhysRevE.47.1815.

[43] Mohamed Khayet Souhaimi and T. Matsuura. *Membrane Distillation: Principles and Applications*. Elsevier Scientific Pub. Co Amsterdam ; New York, 2011.

[44] S. Succi. *The Lattice Boltzmann Equation for Fluid Dynamics and Beyond*. Oxford University Press, 2001.

[45] S. Succi, M. Sbragaglia, and S. Ubertini. *Overview Lattice Boltzmann Method*. http://www.scholarpedia.org/article/Lattice_Boltzmann_Method. Accessed: 2019-12-16. 2010.

[46] Michael R. Swift, E. Orlandini, W. R. Osborn, and J. M. Yeomans. "Lattice Boltzmann simulations of liquid-gas and binary fluid systems." In: *Phys. Rev. E* 54 (5 1996), pp. 5041–5052. DOI: 10.1103/PhysRevE.54.5041. URL: https://link.aps.org/doi/10.1103/PhysRevE.54.5041.

[47] Michael R. Swift, W. R. Osborn, and J. M. Yeomans. "Lattice Boltzmann Simulation of Nonideal Fluids." In: *Phys. Rev. Lett.* 75 (5 1995), pp. 830–833. DOI: 10.1103/PhysRevLett.75.830. URL: https://link.aps.org/doi/10.1103/PhysRevLett.75.830.

[48] Unicef. *Water scarcity*. Accessed: 2023-05-19. URL: https://www.unicef.org/wash/water-scarcity.

[49] Zechun Xiao et al. "Slippery for scaling resistance in membrane distillation: A novel porous micropillared superhydrophobic surface." In: *Water Research* 155 (2019), pp. 152–161. ISSN: 0043-1354. DOI: 10.1016/j.watres.2019.01.036. URL: https://www.sciencedirect.com/science/article/pii/S0043135419300909.

[50] Wei Xiong and Ping Cheng. "Mesoscale simulation of a molten droplet impacting and solidifying on a cold rough substrate." In: *International Communications in Heat and Mass Transfer* 98 (2018), pp. 248–257. ISSN: 0735-1933. DOI: 10.1016/j.icheatmasstransfer.2018.09.001. URL: https://www.sciencedirect.com/science/article/pii/S0735193318302203.

[51] Lenan Zhang, Lin Zhao, and Evelyn N. Wang. "Stefan flow induced natural convection suppression on high-flux evaporators." In: *International Communications in Heat and Mass Transfer* 110 (2020), p. 104255. ISSN: 0735-1933. DOI: https://doi.org/10.1016/j.icheatmasstransfer.2019.03.020. URL: https://www.sciencedirect.com/science/article/pii/S0735193319301071.

[52] Q-S Zheng, Y Yu, and Z-H Zhao. "Effects of hydraulic pressure on the stability and transition of wetting modes of superhydrophobic surfaces." en. In: *Langmuir* 21.26 (2005), pp. 12207–12212.

[53] Yi Zong, Min Li, and Kai Wang. "Outflow boundary condition of multiphase microfluidic flow based on phase ratio equation in lattice Boltzmann method." In: *Physics of Fluids* 33.7 (2021), p. 073304. DOI: 10.1063/5.0058045. eprint: https://doi.org/10.1063/5.0058045. URL: https://doi.org/10.1063/5.0058045.